การศึกษาเชิงเปรียบเทียบประสิทธิภาพของระเบียบวิธีการพาที่มีความละเอียดสูงและไม่สั่นในบริบท ของการเคลื่อนที่ซึ่งเกิดจากบริเวณแบบผสมในของไหลแบบแบ่งชั้น

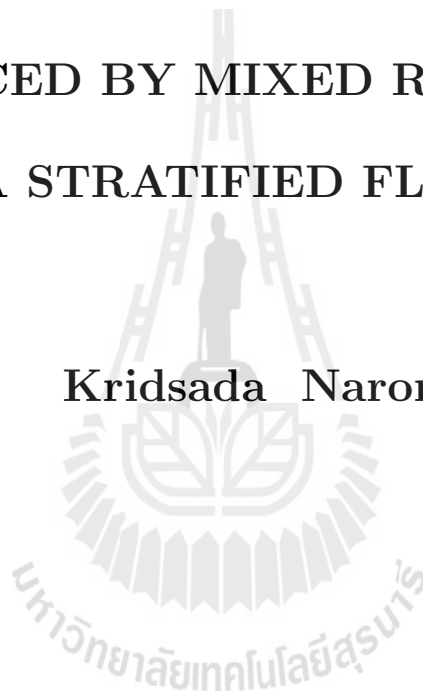นายกฤษดา นารอง

A COMPARATIVE STUDY OF THE

PERFORMANCE OF HIGH RESOLUTION

NON-OSCILLATING ADVECTION SCHEMES

IN THE CONTEXT OF THE MOTION

INDUCED BY MIXED REGION IN

A STRATIFIED FLUID

Kridsada Narong

A Thesis Submitted in Partial Fulfillment of the Requirements for the

Degree of Doctor of Philosophy in Applied Mathematics

Suranaree University of Technology

Academic Year 2010

A COMPARATIVE STUDY OF THE PERFORMANCE OF HIGH RESOLUTION NON-OSCILLATING ADVECTION SCHEMES IN THE CONTEXT OF THE MOTION INDUCED BY MIXED REGION IN A STRATIFIED FLUID

Suranaree University of Technology has approved this thesis submitted in partial fulfillment of the requirements for the Degree of Doctor of Philosophy.

Thesis Examining Committee

_____

(Assoc. Prof. Dr. Prapasri Asawakun)

Chairperson

_____

(Assoc. Prof. Dr. Nikolay Moshkin)

Member (Thesis Advisor)

_____

(Asst. Prof. Dr. Montri Maleewong)

Member

_____

(Prof. Dr. Sergey Meleshko)

Member

_____

(Assoc. Prof. Dr. Adrian Flood)

Member

_____   _____

(Dr. Wut Dankittikul)   (Assoc. Prof. Dr. Prapun Manyum)

Acting Vice Rector for Academic Affairs   Dean of Institute of Science

กฤษดา นารอง : การศึกษาเชิงเปรียบเทียบประสิทธิภาพของระเบียบวิธีการพาที่มี ความละเอียดสูงและไม่สั่นในบริบทของการเคลื่อนที่ ซึ่งเกิดจากบริเวณแบบผสมใน ของไหลแบบแบ่งชั้น (A COMPARATIVE STUDY OF THE PERFORMANCE OF HIGH RESOLUTION NON-OSCILLATING ADVECTION SCHEMES IN THE CONTEXT OF THE MOTION INDUCED BY MIXED REGION IN A STRATIFIED FLUID) อาจารย์ที่ปรึกษา : รองศาสตราจารย์ ดร.นิโคไลน์ มอสกิน, 91 หน้า.

วิทยานิพนธ์นี้ศึกษาปัญหาการยุบตัวของบริเวณผสมแบบสมบูรณ์ในตัวกลางที่มีความ หนาแน่นแบบแบ่งชั้นอย่างต่อเนื่องในสองมิติ และได้เปรียบเทียบประสิทธิภาพการประมาณ ค่าพจน์การพาที่ปรากฏในสมการนาเวียร์สโตก/โอเบอเบค-บูซซิเนสค์ โดยการเปรียบเทียบมี ขึ้นระหว่างระเบียบวิธีอัพวินด์ ระเบียบวิธีฟลักซ์-ลิมิเตอร์ (Minmod Superbee Van Leer และ Monotonized Centered (MC)) ระเบียบวิธีที่ปรับเปลี่ยนได้ (ENO3 และ SMIF) และระเบียบ วิธีแบบถ่วงน้ำหนัก (WENO5) และใช้ผลการทดลองทางห้องปฏิบัติการณ์ของวู (Wu, J. Fluid Mech., 1969, Vol. 35) เป็นบรรทัดฐานในการเปรียบเทียบประสิทธิภาพของระเบียบ วิธีการเชิงตัวเลขดังกล่าว ผลการคำนวณแสดงให้เห็นว่า วิธีฟลักซ์-ลิมิเตอร์ให้ค่าขนาดการ กระจายตัวของบริเวณผสมน้อยที่สุด ขณะที่ระเบียบวิธีแบบถ่วงน้ำหนัก WENO5 ให้ค่าขนาด การกระจายตัวของบริเวณผสมถูกต้องมากกว่าวิธีอื่น ระเบียบวิธีทุกวิธีให้รูปแบบของคลื่น ภายในที่เกิดจากการยุบตัวของบริเวณผสมมีความเสมือนจริง

สาขาวิชาคณิตศาสตร์   ลายมือชื่อนักศึกษา _____

ปีการศึกษา 2553   ลายมือชื่ออาจารย์ที่ปรึกษา _____

KRIDSADA NARONG : A COMPARATIVE STUDY OF THE
PERFORMANCE OF HIGH RESOLUTION NON-OSCILLATING
ADVECTION SCHEMES IN THE CONTEXT OF THE MOTION
INDUCED BY MIXED REGION IN A STRATIFIED FLUID. THESIS
ADVISOR : ASSOC. PROF. NIKOLAY MOSHKIN, Ph.D. 91 PP.

NAVIER-STOKES EQUATIONS/ INCOMPRESSIBLE VISCOUS FLOW/
STRATIFIED FLUIDS/ INTERNAL WAVES/ FINITE DIFFERENCES/
HIGH-ORDER UPWIND SCHEMES.

The problem of a two-dimensional fully mixed region collapsing in a
continuously density-stratified medium is considered. This research deals with
the numerical treatment of the advective terms in the Navier-Stokes equations
in the Oberbeck-Boussinesq approximation. Comparisons are made between the
upwind scheme, flux-limiter schemes, namely Minmod, Superbee, Van Leer and
Monotonized Centred (MC), monotone adaptive stencil schemes namely, ENO3
and SMIF and the weighted stencil scheme WENO5. We used the laboratory
experimental data of Wu (J. Fluid Mech., 1969, Vol. 35) as a benchmark test to
compare the performance of the different numerical approaches. We found that
flux-limiter schemes have the smallest numerical diffusion. The WENO5 scheme
describes more accurately the width of collapsed region variation with time. All
schemes considered give realistic patterns of internal gravity waves generated by
the collapse region.

School of Mathematics	Student's Signature _____
Academic Year 2010	Advisor's Signature _____

ACKNOWLEDGEMENTS

CONTENTS

CONTENTS (Continued)

LIST OF TABLES

LIST OF FIGURES

LIST OF FIGURES (Continued)

LIST OF FIGURES (Continued)

CHAPTER I

INTRODUCTION

The dynamics of a mixed region in density stratified fluids plays an important role in numerous geophysical and engineering applications, and is responsible for the transport of heat, nutrients and pollutants in the oceans and the atmosphere, as well as in various technical devices. In the ocean, for example, turbulent mixing can be caused by tidal flow over bottom topography, by breaking of internal waves or by a body traveling through the oceanic thermocline. Since the mixed fluid region has excess potential energy over its surroundings, the fluid must move towards a new stable equilibrium state; this results in the collapse of the mixed region. The character of this collapse is generally complicated and depends on various parameters including the shape and dimensions of the mixed region, the level of mixing and the background stratification profile. A correct representation of the mixing zone dynamics within a linearly and nonlinearly stratified fluid is a major problem in geophysical and oceanography research.

A number of geophysical phenomena and a number of technical problems related to a flow generated by a local density perturbation in a stratified fluid were studied by Turner (1973); Fedorov (1976); Monin and Ozmidov (1981); Maderich et al. (1988); Lighthill (2002) and Munroe et al. (2009). For example, because the turbulent wake behind a body traveling through a stratified fluid is very slender in the direction of body motion, the flow field induced by wake and the internal waves can be adequately described by studying the collapse of a non-turbulent mixed region in a stratified medium, as investigated by Gilreath and Brandt (1985),

Voropaeva and Chernykh (1998), Lighthill (2002), Voropaeva et al. (2003) and Moshkin et al. (2005).

There are numerous studies focusing on locally homogeneous perturbations of density fields (fully mixed regions). Experimental work on this problem has been done by Wu (1969). To the best of the author's knowledge, Wessel (1969) was the first person who solved the full nonlinear equations numerically for the case of a sharp discontinuity in the density field at the mixed region edge. He obtained gross corroboration with the experiment of Wu (1969) in terms of wave patterns and horizontal size of the mixed region for large time values. The properties of the internal wave patterns are well described in Lytkin and Chernykh (1975) for the case of laminar collapse of the mixed region having various initial density perturbations in a linearly stratified medium. This problem was used by several researchers as a benchmark test in order to assess the performance of numerical algorithms, i.e. Gushchin (1981) and Babakov (1983). In a paper of Nartov and Chernykh (1982), the idea of a nondiffusing passive scalar was used to study the shape of the mixed region over a time period. The methods for localization of singularities by Vorozhtsov and Yanenko (1989) was utilized to define the location of the mixed region edge.

Variable density incompressible viscous flow presents a difficulty for satisfying the property of mass conservation in two respects. On the one hand, the mass density of each fluid particle must remain unchanged during the fluid motion, whatever the level of unsteadiness and mixing. On the other hand, the velocity field must satisfy the incompressibility constraint which reflects the inability of pressure to do compression work. These two important physical characteristics are fully described by the set of the incompressible Navier-Stokes equations augmented by the advection equation for the density. The sharp front/discontinuities

are transported from one location to another, described very well by an advection model. The problem of accurately modeling advection is not limited to the area of geophysical models, and a number of review articles are available in the literature. In regions with large substance gradients and/or velocities, the advection schemes used in many models (upwind-first order, central differences-second order) lead to significant diffusion and/or under-and overshoot of substance values. To describe a sharp discontinuity in the density field at the mixed region edge accurately enough, schemes with high-order approximation of advection terms are required. Godunov's theorem states that any linear monotonic advection scheme can provide no more than first-order accuracy. Therefore, there is a need to apply higher order accuracy nonlinear numerical schemes devised for numerical solutions of conservation laws which support discontinuous solutions.

Computational experience demonstrates that numerical solutions reproduce the physical phenomenon better if they satisfy additional properties such as conservativeness, monotonicity, maximum principle, diminishing total variation and other properties. Many methods match additional requirements; examples are the Lax-Wendroff, Lax-Friedrichs, flux corrected transport (FCT) methods of Boris-Book and Zalesak, slope limiter methods of Van Leer, essentially non-oscillatory (ENO) schemes of Harten-Shu-Osher and total variation diminishing schemes (TVD). There are some books, for example Hirsch (1991); Chung (2002), that discuss many of the classical schemes as well as the flux corrected transport schemes following the work of Boris and Book (1976). Even though there are very few theoretical results about the properties of such schemes in multidimensional and nonlinear cases, in practice these schemes are very robust and stable, and are used in many practical applications. However, there is always the question of what scheme is the best choice, the answer to which is usually problem dependant.

Analysis of the known literature on numerical modeling of flow generated by collapse of a mixed region in a linearly stratified medium shows that there are no studies on the applicability of high-order resolution advection finite-difference schemes to this problem with discontinuity in the density field. A sufficiently complete list of references and a comprehensive overview of research related to numerical modeling of local density perturbed dynamics can be found in Voropaeva and Chernykh (1998).

This study has two objectives: the first is to highlight the high-order upwind schemes as an effective methodology for solving problems of mixed region collapse in stratified media, and the second is to improve the predictability of numerical modeling of problems with sharp discontinuities in the density field.

The organization of this thesis is as follows. In chapter II, the mathematical formulation for the problem of mixed region collapse in the density stratified fluid is described. The governing equations are the Navier-Stokes equations using the Oberbeck-Boussinesq approximation. The numerical algorithm is presented in Chapter III, which also describes details on high-order upwind approximations of convective terms in the governing equations. Some numerical test problems and their numerical solutions are presented in Chapter III. Chapter IV contains results of numerical computations. The problem of flow generated by the collapse of a mixed region is used to assess and compare the accuracy and performance of the various high-order upwind approximations of convective terms in the governing equations. Conclusions and future works of this research are given in the last chapter, Chapter V. The appendices contain a detailed description of the fractional step method which was used to solve the Poisson equation, and the method of calculating the location of Lagrangian particles.

CHAPTER II

MATHEMATICAL MODEL

The collapse of the mixed region and propagation of the gravity current was simulated numerically using a code that solved the full nonlinear Navier-Stokes and mass conservation equations in two dimensions. The equations were simplified by invoking the Oberbeck-Boussinesq approximation which assumes that the maximum change of stratified water density is negligibly small compared with the average density of water itself.

2.1   Governing equations and boundary conditions

The governing equations are the time-dependent incompressible Navier-Stokes equations in primitive variables (velocity and pressure) with the Oberbeck-Boussinesq approximation,

$$\frac{\partial u}{\partial t} + u\frac{\partial u}{\partial x} + v\frac{\partial u}{\partial z} + \frac{1}{\rho_0}\frac{\partial p_1}{\partial x} = \nu\left(\frac{\partial^2 u}{\partial x^2} + \frac{\partial^2 u}{\partial z^2}\right), \tag{2.1}$$

$$\frac{\partial v}{\partial t} + u\frac{\partial v}{\partial x} + v\frac{\partial v}{\partial z} + \frac{1}{\rho_0}\frac{\partial p_1}{\partial z} = \nu\left(\frac{\partial^2 v}{\partial x^2} + \frac{\partial^2 v}{\partial z^2}\right) - g\frac{\rho_1}{\rho_0}, \tag{2.2}$$

$$\frac{\partial \rho}{\partial t} + u\frac{\partial \rho}{\partial x} + v\frac{\partial \rho}{\partial z} = 0, \tag{2.3}$$

$$\frac{\partial u}{\partial x} + \frac{\partial v}{\partial z} = 0. \tag{2.4}$$

Here u and v are the components of fluid velocity in horizontal and vertical directions of the Cartesian coordinates as shown in Figure 2.1, ρ is the fluid density and ν is the kinematic viscosity of the fluid. We use a representation $\rho_1 = \rho - \rho_s$
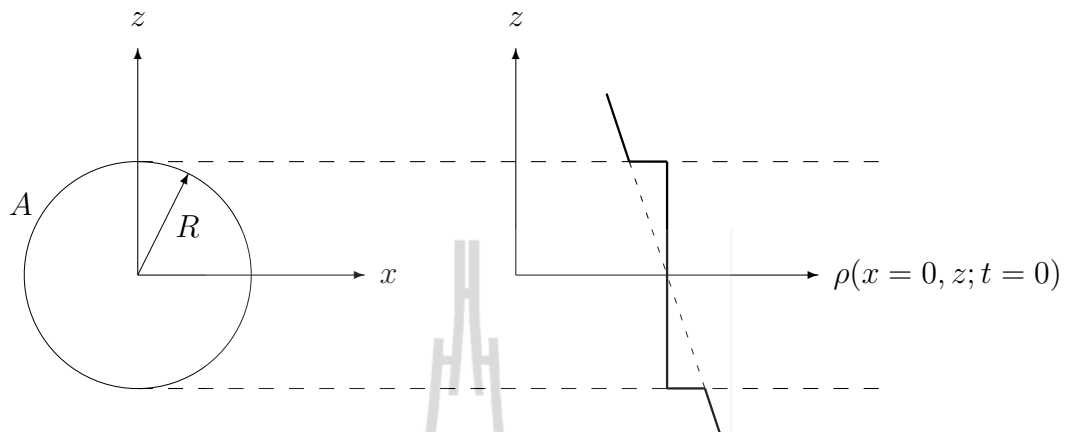
Figure 2.1 The initial mixed region and the initial density profile.

as a defect density, where $\rho_s = \rho_s(z)$ is the undisturbed media density. $\rho_0 = \rho_s(0)$ is an initial density and p_1 is the deviation of pressure from hydrostatic pressure. g is the gravitational acceleration. The stratification is assumed to be stable, i.e. $d\rho_s/dz = -a\rho_0$, where $a = const > 0$.

The boundary and initial conditions are

$$\rho_1 = u = v = 0, \quad x^2 + z^2 \to \infty, \quad t \geq 0, \tag{2.5}$$

$$u = v = 0, \quad -\infty < x, z < \infty, \quad t = 0, \tag{2.6}$$

$$\rho = \begin{cases} \rho_0, \ (x,z) \in A, t = 0, \\ \\ \rho_s, \ (x,z) \notin A, t = 0. \end{cases} \tag{2.7}$$

Here A is the region of totally mixed fluid (also called the mixed region), in particular case $A = \{(x, z) \mid x^2 + z^2 < \mathbb{R}^2\}$ is a circular mixed region with radius R.

2.2 Nondimensional form of governing equations

The system of equations (2.1)-(2.4) and boundary and initial conditions (2.5)-(2.7) are non-dimensionlized by using the radius R as the scale of length

and the Väisälä-Brunt period, $T = 1/\sqrt{ag}$, $(a = -\dfrac{1}{\rho_0}\dfrac{d\rho_s}{dz}|_{z=0})$, as the time scale. Besides, the representation $\rho_1 = \rho_0 a R \tilde{\rho}_1$ ($\tilde{\rho}_1$ denotes a non-dimensional defect of density) is used. As a result, the value $1/Re = \nu T/R^2$ appears in the dimensionless equation instead of kinematic viscosity ν, and instead g is normalized to 1. The Reynolds number (Re) is the only one dimensionless parameter appearing in the nondimensional system.

Equations (2.1) - (2.7) have been non-dimensionlized with the following scalings:

$$\tilde{x} = \frac{x}{R}, \ \tilde{z} = \frac{z}{R}, \ \tilde{u} = \frac{u}{U} = \frac{Tu}{R}, \ \tilde{v} = \frac{v}{U} = \frac{Tv}{R},$$

$$\tilde{p}_1 = \frac{T^2}{\rho_0 R^2}p_1, \ \tilde{\rho} = \frac{\rho}{\rho_0 a R}, \ \tilde{t} = \frac{t}{T}, \tag{2.8}$$

where variables with tilde (˜) refer to their corresponding dimensional variables. After applying all non-dimensional variables, the 2D plane flow becomes a non-dimensional system as follows:

$$\frac{\partial \tilde{u}}{\partial \tilde{t}} + \tilde{u}\frac{\partial \tilde{u}}{\partial \tilde{x}} + \tilde{v}\frac{\partial \tilde{u}}{\partial \tilde{z}} + \frac{\partial \tilde{p}_1}{\partial \tilde{x}} = \frac{1}{Re}\left(\frac{\partial^2 \tilde{u}}{\partial \tilde{x}^2} + \frac{\partial^2 \tilde{u}}{\partial \tilde{z}^2}\right), \tag{2.9}$$

$$\frac{\partial \tilde{v}}{\partial \tilde{t}} + \tilde{u}\frac{\partial \tilde{v}}{\partial \tilde{x}} + \tilde{v}\frac{\partial \tilde{v}}{\partial \tilde{z}} + \frac{\partial \tilde{p}_1}{\partial \tilde{z}} = \frac{1}{Re}\left(\frac{\partial^2 \tilde{v}}{\partial \tilde{x}^2} + \frac{\partial^2 \tilde{v}}{\partial \tilde{z}^2}\right) - \tilde{\rho}_1, \tag{2.10}$$

$$\frac{\partial \tilde{\rho}}{\partial \tilde{t}} + \tilde{u}\frac{\partial \tilde{\rho}}{\partial \tilde{x}} + \tilde{v}\frac{\partial \tilde{\rho}}{\partial \tilde{z}} = 0, \tag{2.11}$$

$$\frac{\partial \tilde{u}}{\partial \tilde{x}} + \frac{\partial \tilde{v}}{\partial \tilde{z}} = 0. \tag{2.12}$$

The boundary and initial conditions in the non-dimensional form are

$$\tilde{\rho}_1 = \tilde{u} = \tilde{v} = 0, \ \ \tilde{x}^2 + \tilde{z}^2 \to \infty, \ \ \tilde{t} \geq 0, \tag{2.13}$$

$$\tilde{u} = \tilde{v} = 0, \ \ -\infty < \tilde{x}, \tilde{z} < \infty, \ \ \tilde{t} = 0, \tag{2.14}$$

$$\tilde{\rho} = \begin{cases} \tilde{\rho}_0, \ (\tilde{x}, \tilde{z}) \in \tilde{A}, \tilde{t} = 0, \\ \\ \tilde{\rho}_s(\tilde{z}), \ (\tilde{x}, \tilde{z}) \notin \tilde{A}, \tilde{t} = 0. \end{cases} \tag{2.15}$$

Here the initial mixed region A becomes a circular region $\tilde{A}$ of radius 1. Henceforth we will omit the superscript ($\tilde{}$) for the non-dimensional quantities; unless it is needed for clarity.

2.3 Advection equation of passive scalar

In order to study the shape history of the mixed region, the idea of non-diffusive concentration of passive scalar C will be used. The transport equation of passive scalar:

$$\frac{\partial C}{\partial t} + u\frac{\partial C}{\partial x} + v\frac{\partial C}{\partial z} = 0, \tag{2.16}$$

is solved together with system (2.9)-(2.15). The initial and boundary conditions are

$$C(x, z) = \begin{cases} C_0 = const \neq 0, & \text{if } (x, z) \in A, \ t = 0, \\ 0, & \text{if } (x, z) \notin A, \ t = 0, \end{cases} \tag{2.17}$$

$$C(x, z) = 0, \quad x^2 + z^2 \to \infty, \quad t > 0. \tag{2.18}$$

Figure 2.2 (a) depicts discontinuity of the initial passive scalar locating at the edge of the circular mixed region A. Under the symmetric property, it allows us to consider a quarter of the whole domain. Figure 2.2 (b) images the half-size of the mixed region under the flow situation.
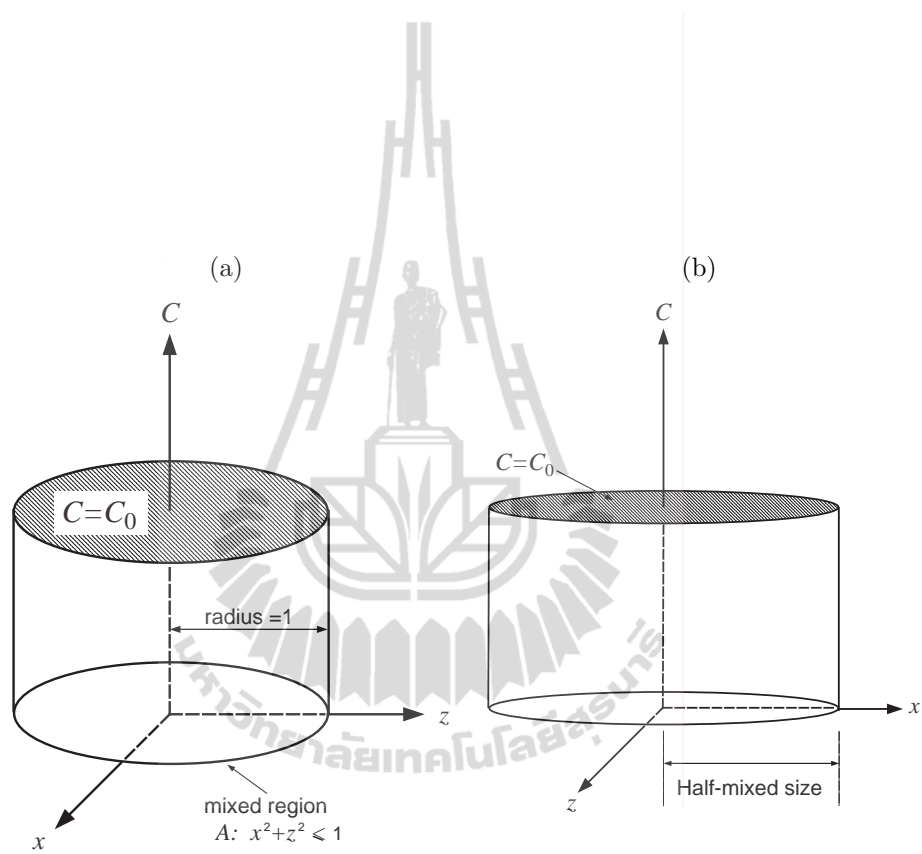
Figure 2.2 Schematic illustration of the passive scalar distribution (a) at initial time, (b) at larger instants of time.

CHAPTER III

NUMERICAL MODEL

A finite difference scheme is used to solve the governing equations. All variables are discretized on a uniform rectangular grid of mesh size Δx and Δz in the horizontal and vertical directions, respectively. The temporal scheme is based on the fractional-step method of Kim and Moin (1985), with slight modification. The Crank-Nicolson scheme is used to approximate the viscous terms. The second-order spatial derivatives are approximated by using second-order central differences. High-order upwind algorithms for advection terms are utilized. A variant of the staggered location of variables is used as depicted in Figure 3.1. The scalar variables are defined at the center of each cell, and the velocity variables on the faces which are perpendicular to their directions. Cell-centered values of velocity components are used as well.

3.1 A projection method

We begin this section with the description of the fractional step method, known as a projection method for solving the incompressible Navier-Stokes equations. Many different forms of projection methods were developed after this method was originally introduced by Chorin (1968) and Temam (1969). We use the form suggested by Kim and Moin (1985) through the finite difference method. The basic idea of the projection method is devising time marching procedures that uncouple the velocity field and the pressure field. It consists of two steps per time step, the first step computes an intermediate velocity without the gradient pres-

sure term. Then it imposes the incompressibility constraint in the second step by solving a Poisson equation.

For the sake of simplicity the system of nondimensional Navier-Stokes equations together with the density equation is recast in the following form:

$$
\begin{cases}
\boldsymbol{u}_t + (\boldsymbol{u} \cdot \nabla)\boldsymbol{u} = -\nabla p_1 + \dfrac{1}{Re}\nabla^2\boldsymbol{u} - \rho_1\mathbf{e}_z, \text{ in domain }, & (3.1) \\[2mm]
\rho_t + (\boldsymbol{u} \cdot \nabla)\rho = 0, \text{ in domain }, & (3.2) \\[2mm]
\nabla \cdot \boldsymbol{u} = 0, \text{ in domain}, & (3.3) \\[2mm]
\boldsymbol{u} = \boldsymbol{b}, \text{ on boundary }, & (3.4)
\end{cases}
$$

where $\boldsymbol{u} = (u, v)$ is velocity vector, $\boldsymbol{b}$ is a boundary condition, and $\mathbf{e}_z$ is a unit vector in the direction opposite to the gravitational force. The projection method can be written in a semi-discrete form as the following system:

1st−step:

$$
\begin{cases}
\dfrac{\boldsymbol{u}^* - \boldsymbol{u}^n}{\Delta t} + (\boldsymbol{u}^{n+1/2} \cdot \nabla)\boldsymbol{u}^{n+1/2} = \dfrac{1}{2Re}(\nabla^2\boldsymbol{u}^* + \nabla^2\boldsymbol{u}^n) - \rho_1\mathbf{e}_z, & (3.5) \\[2mm]
\boldsymbol{u}^* = \boldsymbol{b} + \Delta t\nabla\phi^n, \text{ on boundary}, & (3.6)
\end{cases}
$$

2nd−step:

$$
\begin{cases}
\dfrac{\boldsymbol{u}^{n+1} - \boldsymbol{u}^*}{\Delta t} = -\nabla\phi^{n+1}, & (3.7) \\[2mm]
\boldsymbol{n} \cdot \boldsymbol{u}^{n+1} = \boldsymbol{n} \cdot \boldsymbol{b}, \text{ on boundary}, & (3.8)
\end{cases}
$$

where $\boldsymbol{n}$ is the unit normal, and $\boldsymbol{u}^*$ represents the intermediate velocity. The nonlinear convection term $(\boldsymbol{u}^{n+1/2}.\nabla)\boldsymbol{u}^{n+1/2}$ can be expressed in many ways; for example in this thesis we use an explicit Adams-Bashforth formula:

$$
(\boldsymbol{u}^{n+1/2} \cdot \nabla)\boldsymbol{u}^{n+1/2} \approx \frac{3}{2}(\boldsymbol{u}^n \cdot \nabla)\boldsymbol{u}^n - \frac{1}{2}(\boldsymbol{u}^{n-1} \cdot \nabla)\boldsymbol{u}^{n-1}. \tag{3.9}
$$
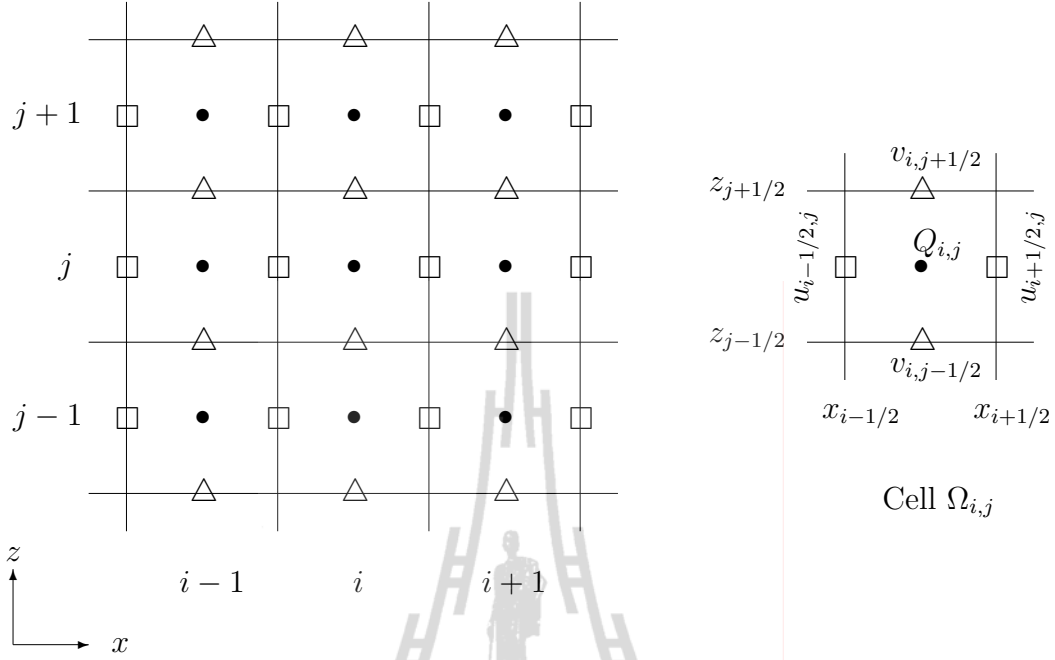
Figure 3.1   Staggered grid: $\square - u$, $\triangle - v$ and $\bullet - Q$

The pressure p_1^{n+1} can be obtained from ϕ^{n+1} through the relation below (see more details in Brown et al. (2001))

$$p_1^{n+1} = \phi^{n+1} - \frac{\Delta t}{2Re}\nabla^2\phi^{n+1}. \tag{3.10}$$

To compute ϕ^{n+1}, we apply the divergence operator $(\nabla\cdot)$ to (3.7) and use (3.3). We then have the Poisson equation for ϕ^{n+1}:

$$\nabla^2\phi^{n+1} = \frac{1}{\Delta t}\nabla \cdot \boldsymbol{u}^*. \tag{3.11}$$

To compute ρ^{n+1}, the following semi-discretization will be performed with high-resolution schemes for the density equation

$$\frac{\rho^{n+1} - \rho^n}{\Delta t} + (\boldsymbol{u}^n \cdot \nabla)\rho^n = 0. \tag{3.12}$$

The next algorithm shows the whole computation of the projection method for the governing equations. All steps were performed on a rectangular domain $[0, \mathrm{X}] \times [0, \mathrm{Z}] \subset \mathbb{R}^2$ with uniform meshes, $\Delta x = \Delta z$. Grid points x_i and z_j are

defined by $x_i = i\Delta x, i = 0, 1, ..., N_x$ and $z_j = j\Delta z, j = 0, 1, ..., N_z$. The staggered grid in Figure 3.1 is applied to discretize the governing equations. The horizontal velocity u is defined at the middle of the vertical wall, while the vertical velocity v at the middle of the horizontal wall of cell $\Omega_{i,j}$. Cell-centered velocity components are denoted by capital letters U and V, and they are the approximations of the cell average

$$U_{i,j} \approx \frac{1}{\Delta x \Delta z} \int_{\Omega_{i,j}} u(t, x, z) dx dz, \quad V_{i,j} \approx \frac{1}{\Delta x \Delta z} \int_{\Omega_{i,j}} v(t, x, z) dx dz. \qquad (3.13)$$

Other variables, p_1, ρ, C and ϕ, are defined at the cell center in the same way. The capital letter $Q_{i,j}$ represents the approximation to the cell average value of conservative quantity q defined by the following:

$$Q_{i,j} \equiv \int_{\Omega_{i,j}} q(t, x, z) dx dz, \qquad (3.14)$$

where $\Omega_{i,j} = [x_{i-1/2}, x_{i+1/2}] \times [z_{j-1/2}, z_{j+1/2}]$. We notice that $x_{i\pm 1/2}$ and $z_{j\pm 1/2}$ are vertices of cell $\Omega_{i,j}$ defined by $x_{i\pm 1/2} = x_i \pm \Delta x/2$ and $z_{j\pm 1/2} = z_j \pm \Delta z/2$, respectively.

Algorithm 1:

- Step1: Obtain intermediate cell-centered velocities $\boldsymbol{U}^*$.

    - Substep 1.1: Use the centered values $\boldsymbol{Q}^n = (U^n, V^n, \rho^n) = (\boldsymbol{U}^n, \rho^n)$ and edge values $\boldsymbol{u}^n = (u^n, v^n)$ to solve the advection equation

    $$\frac{\boldsymbol{Q}^\dagger - \boldsymbol{Q}^n}{\Delta t} + \boldsymbol{u}^n \cdot \nabla \boldsymbol{Q}^n = 0. \qquad (3.15)$$

    This is solved on a finite volume grid using the explicit high-resolution upwind algorithm. The resulting solution is $\boldsymbol{Q}^\dagger = (U^\dagger, V^\dagger, \rho^{n+1}) = (\boldsymbol{U}^\dagger, \rho^{n+1})$

– Substep 1.2: Use a Crank-Nicolson discretization for the diffusion term.

$$\frac{\boldsymbol{U}^* - \boldsymbol{U}^\dagger}{\Delta t} = \frac{1}{2Re}\left(\nabla^2 \boldsymbol{U}^* + \nabla^2 \boldsymbol{U}^\dagger\right) + \rho_1^{n+1}\mathbf{e}_z \qquad (3.16)$$

This gives the intermediate velocities $\boldsymbol{U}^* = (U^*, V^*)$ at cell center. The implicit equation (3.16) is inverted at every time step using a splitting scheme (see details in Appendix A). This decomposes the 2D system into a decoupled system of 1D equations which are efficiency inverted using the Thomas algorithm for a tridiagonal matrix.

• Step 2: Obtain the edge velocity by

$$\boldsymbol{u}^{n+1} = \boldsymbol{u}^* - \Delta t \nabla \phi^{n+1}, \qquad (3.17)$$

where $\boldsymbol{u}^* = (u^*, v^*)$ is the average of the adjacent $\boldsymbol{U}^*$:

$$u^*_{i-1/2,j} = \frac{1}{2}\left(U^*_{i-1,j} + U^*_{i,j}\right),$$
$$v^*_{i,j-1/2} = \frac{1}{2}\left(V^*_{i,j-1} + V^*_{i,j}\right).$$

The update (3.17) requires the values ϕ^{n+1}, which can be obtained by solving a discrete Poisson problem (3.11) with the Neumann boundary condition $\partial\phi/\partial\mathbf{n} = 0$, (see details in Appendix A).

• Step 3: In the final step, we update the cell-centered velocities $\boldsymbol{U}^{n+1}$ and pressure p_1^{n+1} by

$$U_{i,j}^{n+1} = U_{i,j}^* - \frac{\Delta t}{2\Delta x}\left(\phi_{i+1,j}^{n+1} - \phi_{i-1,j}^{n+1}\right), \qquad (3.18)$$
$$V_{i,j}^{n+1} = V_{i,j}^* - \frac{\Delta t}{2\Delta z}\left(\phi_{i,j+1}^{n+1} - \phi_{i,j-1}^{n+1}\right), \qquad (3.19)$$
$$p_{1_{i,j}}^{n+1} = \phi_{i,j}^{n+1} - \frac{\Delta t}{2Re}\nabla^2\phi_{i,j}^{n+1}. \qquad (3.20)$$

This completes one time step. Go to Step 1 for next time step.

3.2   High-resolution schemes for advection equations.

To describe the discontinuity in density at the mixed region edge with sufficient accuracy a monotone scheme of high order of approximation is required. For simplicity, we illustrate the methods under study by considering the one-dimensional scalar advection equation for a quantity Q which can be one of the following u, v, ρ, or passive scalar C,

$$\frac{\partial Q}{\partial t} + \frac{\partial (uQ)}{\partial x} = 0. \tag{3.21}$$

Let $f = f(Q(x,t)) = uQ$ denote a physical flux function with constant speed u. $\hat{Q}$ is the numerical solution of Q while x and t represent the space and time variables, respectively. We want to solve (3.21) on an interval $I = [a,b]$, with suitable boundary conditions. Let us consider, for simplicity, a uniform grid spacing Δx on I of points $\{x_i\}, i = 0, 1, ..., N$, where $x_i = x_0 + i\Delta x$ with $x_0 = a$ and $x_N = b$. Let Δt be the time stepping. Discretization of (3.21) using an explicit forward Euler method in time and central flux in space is given below

$$
\begin{aligned}
\hat{Q}_i^{n+1} &= \hat{Q}_i^n - \frac{\Delta t}{\Delta x}[(u\hat{Q})_{i+1/2}^n - (u\hat{Q})_{i-1/2}^n] \\
&= \hat{Q}_i^n - \frac{\Delta t}{\Delta x}[\hat{F}_{i+1/2}^n - \hat{F}_{i-1/2}^n],
\end{aligned}
\tag{3.22}
$$

where $\hat{F}_{i+1/2}^n \approx f(Q(x_{i+1/2}, t^n))$ is a numerical flux which approximates the average flux along the cell interface at $x_{i+1/2}$. Figure 3.2 illustrates the numerical fluxes $\hat{F}_{i\pm1/2}$ of cell i. In the next paragraph, we describe the different approximations of numerical flux $\hat{F}_{i+1/2}^n$ that are used in this thesis. These include four flux-limiter schemes, two adaptive stencil schemes, and one weighted stencil scheme.
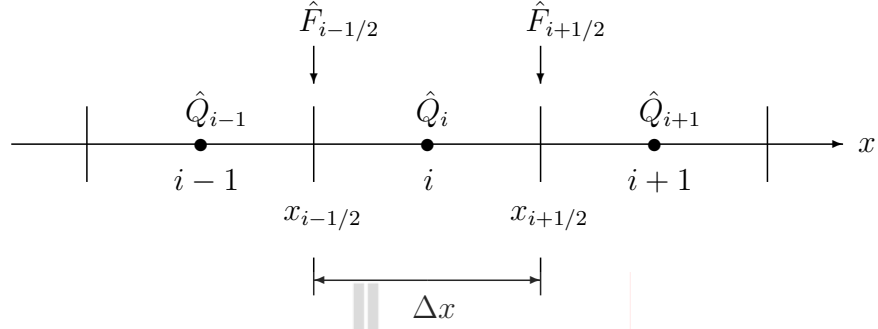
Figure 3.2 Finite difference discretization 1D-problem.

3.2.1 Flux-limiter schemes

One can approximate the numerical flux in (3.22) by the first-order upwind method

$$
\hat{F}_{i+1/2}^n =
\begin{cases}
u\hat{Q}_i^n, & \text{if } u > 0, \\
u\hat{Q}_{i+1}^n, & \text{if } u < 0.
\end{cases}
\tag{3.23}
$$

The numerical flux $\hat{F}_{i+1/2}^n$ resulting from an upwind method is called the "upwind flux". Using the upwind flux in the approximation of $\partial(uQ)/\partial x$ avoids non-physical oscillations, but is unfortunately affected by excessive numerical diffusion. One strategy to avoid nonphysical oscillations and excessive numerical diffusion is using a hybrid method which uses the second order numerical flux in smooth regions and limits the solution in the vicinity of discontinuities by using the monotonic upwind method in these regions. This procedure is carried out by introducing a flux-limiter based on the local gradient of the solution (3.21). We write the interface value $\hat{Q}_{i+1/2}$ as the sum of the diffusive first order upwind term and an "anti-diffusive" one. The higher order anti-diffusive part is multiplied by the flux limiter $\Psi(\theta)$, which depends locally on the nature to the solution. This function is expressed by a new parameter θ namely the "slopes ratio". It's the ratio of the slope at the neighboring interface in the upwind direction to the slope at the current interface.

$$\theta_{i+1/2} = \begin{cases} \dfrac{\hat{Q}_i^n - \hat{Q}_{i-1}^n}{\hat{Q}_{i+1}^n - \hat{Q}_i^n} & \equiv \theta_{i+1/2}^+ & \text{if } u_{i+1/2}^n > 0, \\[3mm] \dfrac{\hat{Q}_{i+2}^n - \hat{Q}_{i+1}^n}{\hat{Q}_{i+1}^n - \hat{Q}_i^n} & \equiv \theta_{i+1/2}^- & \text{if } u_{i+1/2}^n < 0. \end{cases} \tag{3.24}$$

Introduction of this parameter θ, and the limiter function $\Psi(\theta)$, lead to the flux limiter version of the hybrid schemes as

$$\hat{Q}_{i+1/2}^n = \begin{cases} \hat{Q}_i^n + \dfrac{1}{2}(\hat{Q}_{i+1}^n - \hat{Q}_i^n)\Psi(\theta_{i+1/2}^+) & \text{if } u_{i+1/2}^n > 0, \\[3mm] \hat{Q}_{i+1}^n - \dfrac{1}{2}(\hat{Q}_{i+1}^n - \hat{Q}_i^n)\Psi(\theta_{i+1/2}^-) & \text{if } u_{i+1/2}^n < 0. \end{cases} \tag{3.25}$$

The interface value $\hat{Q}_{i-1/2}^n$ is obtained from $\hat{Q}_{i+1/2}^n$ by substituting the index i by $i-1$. From equation (3.24), one can see that if $\Psi = 0$ once again we find the upwind scheme, and if $\Psi = 1$ the scheme is reduced to the centered one. The limiting procedure must be carried out under some constraints to ensure stability of the scheme. The following limiter functions used in this study satisfy these constraints (see more details in LeVeque (1996)) including the following:

$$\begin{aligned} \text{Minmod}: \Psi(\theta) &= max(0, min(1, \theta)), \\ \text{Superbee}: \Psi(\theta) &= max(0, min(1, 2\theta), min(2, \theta)), \\ \text{Van Leer}: \Psi(\theta) &= (\theta + |\theta|)/(1 + |\theta|), \\ \text{MC}: \Psi(\theta) &= max\left(0, min\left(\frac{1+\theta}{2}, 2, 2\theta\right)\right). \end{aligned} \tag{3.26}$$

The Minmod and Superbee limiters have been introduced by Roe (1983), and Roe and Sidilkover (1992). The Van Leer limiter was introduced in the paper by Van-Leer (1974), and the monotonized central (MC) limiter was also introduced by Van Leer in a later paper of Van-Leer (1977).

Extension to two-dimensional space

The generalization of the finite-difference scheme considered to two dimensions is easily performed for convective terms as splitting mode in each one-dimensional directions. This way of extending a finite difference scheme is very simple and efficient, and hence is widely used in applications. However, this scheme is only second order accurate for general nonlinear systems, regardless of the order of accuracy in the one-dimensional procedure Zhang et al. (2010).

Here we consider the two dimensional advection equation in conservation form:

$$\frac{\partial Q}{\partial t} + \frac{\partial f}{\partial x} + \frac{\partial g}{\partial z} = 0, \tag{3.27}$$

where $f = uQ$, $g = vQ$ and u, v are constants velocities in x and z directions, respectively. We approximate (3.27) by the following semidiscrete form

$$\frac{\partial Q}{\partial t} = -\frac{1}{\Delta x}\left(\hat{F}_{i+1/2,j} - \hat{F}_{i-1/2,j}\right) - \frac{1}{\Delta z}\left(\hat{G}_{i,j+1/2} - \hat{G}_{i,j-1/2}\right), \tag{3.28}$$

where $\hat{F}$ and $\hat{G}$ represent numerical fluxes at the cell walls for f and g respectively (see Figure 3.3). We assume that the values of the numerical solution are also available outside the computational domain whenever they are needed. The numerical flux $\hat{F}_{i+1/2,j}$ is obtained by the one dimensional upwind flux (with j fixed) applied to $f = uQ$. Likewise, the numerical flux $\hat{G}_{i,j+1/2}$ is obtained by the one dimensional upwind flux applied to $g = vQ$ with i fixed. Limiter versions can be applied to both directions.

3.2.2 Adaptive stencil schemes: SMIF

Here we consider a hybrid monotonic difference scheme based on a combination of a Modified Central Difference Scheme (MCDS) and Modified Upwind
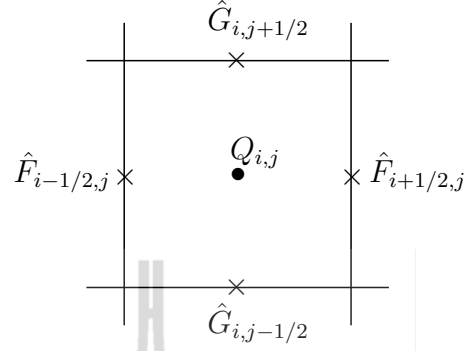
Figure 3.3 Four fluxes at cell walls in 2D advection conservation law.

Difference Scheme (MUDS) with a special switch condition. This scheme was developed in Gushchin and Konshin (1992), Gushchin and Matyushin (1997), and Belotserkovskii (1997) for the numerical simulation of fluid flows with large gradients of hydrodynamic parameters. It was named the Splitting on physical factors Method for Incompressible Fluid flows (SMIF). This splitting scheme is similar to the famous SMAC method (see Amsden and Harlow (1970)) and to one of the approaches suggested in Fortin et al. (1971). The hybrid finite-difference scheme is constructed for convective terms.

To describe the special switch condition of the SMIF scheme for the advection equation, it is easy to consider the 1D linear model equation (3.21) with $u = const$. The numerical flux $\hat{F}^n_{i+1/2}$ can be written in the following form:

$$\hat{F}^n_{i+1/2} = u\hat{Q}^n_{i+1/2},$$

where $\hat{Q}^n_{i+1/2}$ is approximated by

$$\hat{Q}^n_{i+1/2} = \begin{cases} \alpha\hat{Q}^n_{i-1} + (1 - \alpha - \beta)\hat{Q}^n_i + \beta\hat{Q}^n_{i+1}, & u \geq 0, \\ \alpha\hat{Q}^n_{i+2} + (1 - \alpha - \beta)\hat{Q}^n_{i+1} + \beta\hat{Q}^n_i, & u < 0. \end{cases} \tag{3.29}$$

In this case, the first differential approximation for equation (3.21) has the form

$$Q_t + uQ_x = \left[\frac{\Delta x}{2}|u|(1 + 2\alpha - 2\beta) - \frac{\Delta t u^2}{2}\right] Q_{xx}. \tag{3.30}$$

If $\alpha = \beta = 0$ in (3.29), one will obtain the usual first-order monotonic scheme which is stable when the *Courant number* (C_{cour}) satisfies the following condition:

$$0 < C_{cour} = \frac{\Delta t |u|}{\Delta x} \leq 1. \qquad (3.31)$$

If $\alpha = 0$, $\beta = 0.5$, one will obtain the usual central difference scheme, and for $\alpha = -0.5$, $\beta = 0$ the usual upwind scheme. The last two schemes are of second-order accuracy in the space variable and are non-monotonic. Schemes with upwind differences, i.e. $\beta = 0$, should have a minimum scheme viscosity, as can readily be seen from equation (3.30), provided the following condition on α holds,

$$\alpha = -0.5(1 - C_{cour}). \qquad (3.32)$$

For schemes with $\alpha = 0$, the analogous condition is

$$\beta = 0.5(1 - C_{cour}). \qquad (3.33)$$

Since an explicit finite difference scheme is considered, the subsequent analysis is reduced to the necessary condition (3.31) for stability in the case of the explicit schemes. Let us assume that there is a monotonic function Q_i^n, for example, $\triangle \hat{Q}_{i+1/2}^n \equiv \hat{Q}_{i+1}^n - \hat{Q}_i^n$ at any i.

The function $\hat{Q}_i^{n+1}$ will also be monotonic when the following conditions are satisfied:

(a) for a scheme with $\beta = 0$ and α from relationship (3.32), under the condition

$$\triangle \hat{Q}_{i+1/2}^n \leq \zeta(C_{cour}) \triangle \hat{Q}_{i-1/2}^n, \text{ where } \zeta(C_{cour}) = 0.5(1 - C_{cour})/(2 - C_{cour});$$

(b) for a scheme with $\alpha = 0$ and β from relationship (3.33), under the condition

$$\triangle \hat{Q}_{i+1/2}^n \leq \sigma(C_{cour}) \triangle \hat{Q}_{i-1/2}^n, \text{ where } \sigma(C_{cour}) = 2(1 + C_{cour})/C_{cour}.$$

It can be seen from this that the domains of monotonicity of the homogeneous scheme being considered have a non-empty intersection. Hence, a whole class

of hybrid schemes is distinguished by the condition of switching over from one homogeneous scheme to another. The general form of this condition is as follows:

$$\triangle \hat{Q}_{i+1/2}^n = \delta \triangle \hat{Q}_{i-1/2}^n \text{ where } \zeta(C_{cour}) \leq \delta \leq \sigma(C_{cour}).$$

The choice of $\delta = 1$ corresponds to the points of the interchange of the sign of the second difference Q_i^n and makes it possible to obtain the estimate $Q_{xx} = O(h)$ for the required function Q at the intersection points, by means of which a second-order approximation is retained with respect to the spatial variables of smooth solutions. The following switching criterion were developed:

$$\text{if}(u \cdot \triangle \hat{Q} \cdot \triangle^2 \hat{Q})_{i+1/2}^n \geq 0, \text{ then the scheme with } \beta = 0 \text{ (MUDS) is used,}$$

$$\text{if}(u \cdot \triangle \hat{Q} \cdot \triangle^2 \hat{Q})_{i+1/2}^n < 0, \text{ then the scheme with } \alpha = 0 \text{ (MCDS) is used,}$$

where $\triangle^2 \hat{Q}_{i+1/2}^n = \triangle \hat{Q}_{i+1}^n - \triangle \hat{Q}_i^n$. On smooth solutions this scheme has a second order of approximation with respect to the time and spatial variables. It is stable when the *Courant criterion* (3.31) is satisfied and monotonic. Moreover, it was shown by Gushchin and Konshin (1992) that this hybrid scheme comes nearest to the third order schemes.

Extension to two-dimensional space

We use the same idea as in the flux-limiter scheme for extension to the 2D case. To compute the numerical flux in (3.50) of the four cell faces, we use the one dimensional SMIF method in each direction. The flux $\hat{F}_{i+1/2,j}^n$ is defined by

$$\hat{F}_{i+1/2,j}^n = u\hat{Q}_{i+1/2,j}^n,$$

where $\hat{Q}_{i+1/2,j}^n$ is approximated by

$$\hat{Q}_{i+1/2,j}^n = \begin{cases} \alpha\hat{Q}_{i-1,j}^n + (1-\alpha-\beta)\hat{Q}_{i,j}^n + \beta\hat{Q}_{i+1,j}^n, & u \geq 0, \\ \\ \alpha\hat{Q}_{i+2,j}^n + (1-\alpha-\beta)\hat{Q}_{i+1,j}^n + \beta\hat{Q}_{i,j}^n, & u < 0. \end{cases} \quad (3.34)$$

Parameters α and β are computed from (3.32)-(3.33) with $C_{cour} = \dfrac{\Delta t|u|}{\Delta x}$. And, the flux $\hat{G}_{i,j+1/2}^n$ is defined by

$$\hat{G}_{i,j+1/2}^n = v\hat{Q}_{i,j+1/2}^n,$$

where $Q_{i,j+1/2}^n$ is approximated by adaptive stencil

$$\hat{Q}_{i,j+1/2}^n = \begin{cases} \alpha\hat{Q}_{i,j-1}^n + (1-\alpha-\beta)\hat{Q}_{i,j}^n + \beta\hat{Q}_{i,j+1}^n, & v \geq 0, \\ \\ \alpha\hat{Q}_{i,j+2}^n + (1-\alpha-\beta)\hat{Q}_{i,j+1}^n + \beta\hat{Q}_{i,j}^n, & v < 0. \end{cases} \quad (3.35)$$

Again, parameters α and β are computed from (3.32)-(3.33) with $C_{cour} = \dfrac{\Delta t|v|}{\Delta z}$.

3.2.3 Adaptive stencil schemes: ENO

Traditional finite difference methods for construction of the numerical fluxes are based on fixed stencil interpolations. For example, for the construction of flux $\hat{F}_{i+1/2}$ with the third order accuracy, the data points of the cell $i-1, i$ and $i+1$ can be used to build an interpolation polynomial of second degree. However, a fixed stencil of second or higher order accuracy gives oscillations near a discontinuity. These oscillations do not decrease when the mesh is refined and they can be a reason for numerical instabilities in nonlinear problems containing discontinuities. Using only data points from the smoothest parts around the discontinuity for the construction can help avoid such oscillations. In this section, the finite difference ENO will be described in order to obtain the numerical flux $\hat{F}_{i+1/2}$. To explain the ENO method, a piecewise polynomial interpolation of the
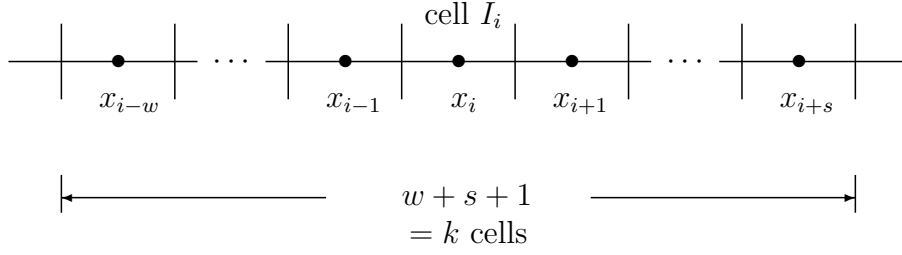
Figure 3.4   Stencil $S_i^{(w)} = \left\{ I_{i-w}, \cdots, I_{i-1}, I_i, I_{i+1}, \cdots, I_{i+s} \right\}$

given data points $\{f_0, f_1, ... f_{i-1}, f_i, f_{i+1}, ..., f_N\}$ will be considered for each interval $I_i = [x_{i-1/2}, x_{i+1/2}]$. We denote the stencil $S_i^{(w)}$ of size k cells around cell I_i as follow:

$$S_i^{(w)} = \{I_{i-w}, ..., I_i, I_{i+1}, ..., I_{i+s}\}, \tag{3.36}$$

where w and s are two integers with the properties $-1 \leq w \leq k-1$ and $w+s+1 = k$. Figure 3.4 illustrates the stencil $S_i^{(w)}$ with w cells to the left and s cells to the right. In this thesis, we only focus on the case $k = 3$ which corresponds to $3^{rd}-$ENO or simply ENO3. Therefore, we have four stencils,

$$
\begin{aligned}
S_i^{(-1)} &= \{I_{i+1}, I_{i+2}, I_{i+3}\}, \\
S_i^{(0)} &= \{I_i, I_{i+1}, I_{i+2}\}, \\
S_i^{(1)} &= \{I_{i-1}, I_i, I_{i+1}\}, \\
S_i^{(2)} &= \{I_{i-2}, I_{i-1}, I_i\}.
\end{aligned}
$$

The key idea of the ENO method is an "adaptive stencil" $S_i^{(w)}$ to building up an interpolation polynomial of degree k, representative for cell I_i. Among all of the candidate stencils, the "smoothest" stencil will be used. A larger magnitude of divided differences indicates less smoothness within the stencil. This process tries to not include the data points with high gradient and discontinuities in the desired stencil. The interpolation avoids the oscillation artifacts formed by interpolating over discontinuities, hence the name essentially non-oscillatory(ENO).

In order to get the ENO3 stencil, construction via primitive functions will be considered in this section. It is easy to obtain a convenient algorithm for computer programming to approximate the numerical flux $\hat{F}_{i+1/2}$. First of all, we define an auxiliary function $h(x)$ implicitly as follows,

$$f(Q(x)) = \frac{1}{\Delta x} \int_{x-\Delta x/2}^{x+\Delta x/2} h(\xi)d\xi. \tag{3.37}$$

Differentiate (3.37) on both sides

$$\frac{\partial f(Q(x))}{\partial x} = \frac{h(x + \Delta x/2) - h(x - \Delta x/2)}{\Delta x}. \tag{3.38}$$

Comparing (3.38) with the discritization (3.22) shows that $h(x)$ is identical to the numerical flux function at the cell walls. That is, $\hat{F}_{i\pm1/2} = h(x_{i\pm1/2})$ for all i. The function $h(x)$ can be found by finding its primitve

$$H(x) = \int_{x_{i-1/2}}^{x} h(\xi)d\xi. \tag{3.39}$$

We construct the primitive $H(x)$ of $h(x)$ by using polynomial interpolation, and then take a derivative to get $h(x)$. The coefficients of the polynomial are the entries in the divided difference table. We use the notation, $D_i^l H$ to represent the lth divided difference of the function H at grid point i. For $l = 0, .., 3$, the divided differences of H are defined by the following fomulas,

$$0^{th}: \quad D_{i+1/2}^0 H \quad = H(x_{i+1/2}) \tag{3.40}$$

$$
\begin{aligned}
1^{st}: \quad D_i^1 H \quad &= \frac{H(x_{i+1/2}) - H(x_{i-1/2})}{\Delta x} \\
&= f(Q_i) \\
&= f_i
\end{aligned}
\tag{3.41}
$$

$$2^{nd}: \quad D_{i+1/2}^2 H = \frac{D_{i+1}^1 H - D_i^1 H}{2\Delta x}$$

$$= \frac{1}{2\Delta x}(f(Q_{i+1}) - f(Q_i))$$

$$= \frac{1}{2\Delta x}(f_{i+1} - f_i) \tag{3.42}$$

$$3^{rd}: \quad D_i^3 H = \frac{D_{i+1/2}^2 H - D_{i-1/2}^2 H}{3\Delta x}$$

$$= \frac{1}{3\Delta x}\left(\frac{f(Q_{i+1}) - f(Q_i)}{2\Delta x} - \frac{f(Q_i) - f(Q_{i-1})}{2\Delta x}\right)$$

$$= \frac{1}{6(\Delta x)^2}\left(f(Q_{i+1}) - 2f(Q_i) + f(Q_{i-1})\right)$$

$$= \frac{1}{6(\Delta x)^2}\left(f_{i+1} - 2f_i + f_{i-1}\right) \tag{3.43}$$

The next algorithm is the ENO3 procedure. Step one to three produce three polynomials $P_i^{(1)}(x), P_i^{(2)}(x)$ and $P_i^{(3)}(x)$, where $x \in [x_{i-1/2}, x_{i+1/2}]$. The final step performs the approximation of numerical flux $\hat{F}_{i+1/2}$ by taking the derivative of $P_i^{(1)}(x) + P_i^{(2)}(x) + P_i^{(3)}(x)$ at $x = x_{i+1/2}$.

Algorithm 2:

At each interface $i+1/2$, set $\lambda_{i+1/2} = \frac{\partial f(Q)}{\partial Q}|_{i+1/2}$ which is used to identify the wind directions at cell interface $x_{i+1/2}$.

- Step ①: If $\lambda_{i+1/2} > 0$,

    set $\kappa = i$.

    Otherwise, set $\kappa = i + 1$.

    Define

    $$P_i^{(1)}(x) = (D_\kappa^1 H)(x - x_{i+1/2}). \tag{3.44}$$

- Step ②: If $|D_{\kappa-1/2}^2 H| \leq |D_{\kappa+1/2}^2 H|$,

    then $c = D_{\kappa-1/2}^2 H$ and $\kappa^* = \kappa - 1$.

Otherwise, $c = D^2_{\kappa+1/2}H$ and $\kappa^* = \kappa$.

Define

$$P_i^{(2)}(x) = c(x - x_{i-1/2})(x - x_{\kappa+1/2}). \tag{3.45}$$

- Step ③: If $|D^3_{\kappa^*}H| \le |D^3_{\kappa^*+1}H|$,

  then $c^* = D^3_{\kappa^*}H$.

  Otherwise, $c^* = D^3_{\kappa^*+1}H$.

  Define

$$P_i^{(3)}(x) = c^*(x - x_{\kappa^*-1/2})(x - x_{\kappa^*+1/2})(x - x_{\kappa^*-3/2}). \tag{3.46}$$

- Step ④: Finally,

$$\hat{F}_{i+1/2} = H'(x_{i+1/2}) = P_i'^{(1)}(x_{i+1/2}) + P_i'^{(2)}(x_{i+1/2}) + P_i'^{(3)}(x_{i+1/2}) \tag{3.47}$$

which simplifies to

$$\hat{F}_{i+1/2} = D^1_\kappa H + c\left(2(i-\kappa)+1\right)\Delta x + c^*\left(3(i-\kappa^*)^2 - 1\right)(\Delta x)^2 \tag{3.48}$$

The diagram in Figure 3.5 depicts the conditions in the steps ①, ② and ③ of the ENO algorithm. To construct the numerical flux $\hat{F}_{i+1/2}$, we begin with $\lambda_{i+1/2}$. The conditional of statement of step ① yields κ, follow by the conditional statement in ② which yields κ^*. After that, the condition of step ③ is performed in order to have c^*. The algorithm gives us a sequence of $\{\kappa, \kappa^*, c^*\}$ and a set of polynomials $P_i^{(1)}$, $P_i^{(2)}$, $P_i^{(3)}$. The numerical flux resulting from this sequence is equivalent to one of stencils $S_i^{(-1)}$, $S_i^{(0)}$, $S_i^{(1)}$,or $S_i^{(2)}$. In the diagram, a top-down tracking of bold lines leads us to one of the these four stencils. There is only one possible choice to obtain stencil $S_i^{(-1)}$ or $S_i^{(2)}$. While, stencil $S_i^{(0)}$ and $S_i^{(1)}$ have three possible choices. For example, after performing the conditions

①, ② and ③, we obtain $\kappa = i$, $\kappa^* = i - 1$ and $c^* = D^3_{i-1}$. The polynomials $P_i^{(1)}(x_{i+1/2})$, $P_i^{(2)}(x_{i+1/2})$, $P_i^{(3)}(x_{i+1/2})$ can be obtained by using (3.44), (3.45) and (3.46), respectively. We compute the numerical flux $\hat{F}_{i+1/2}$ via the equation (3.47) as follows,

$$
\begin{aligned}
\hat{F}_{i+1/2} &= H'(x_{i+1/2}), \quad \text{where } H = P^{(1)} + P^{(2)} + P^{(3)} \\
&= P_1'(x_{i+1/2}) + P_2'(x_{i+1/2}) + P_3'(x_{i+1/2}) \\
&= D^1_\kappa H + c\left(2(i - \kappa) + 1\right)\Delta x + c^*\left(3(i - \kappa^*)^2 - 1\right)(\Delta x)^2, \quad c = D^2_{\kappa-1/2}H \\
&= D^1_i H + \left(D^2_{i-1/2}H\right)\Delta x + \left(D^3_{i-1}H\right)(2)(\Delta x)^2 \\
&= f_i + \frac{1}{2\Delta x}(f_i - f_{i-1})\Delta x + \frac{1}{6(\Delta x)^2}(f_i - 2f_{i-1} + f_{i-2})(2)(\Delta x)^2 \\
&= f_i + \frac{1}{2}(f_i - f_{i-1}) + \frac{1}{3}(f_i - 2f_{i-1} + f_{i-2}) \\
&= \frac{1}{3}f_{i-2} - \frac{7}{6}f_{i-1} + \frac{11}{6}f_i \\
&= \sum_{j=0}^{2} c_{w,j}f_{i-w+j}, \quad \text{with } w = 2,
\end{aligned}
\tag{3.49}
$$

where $w = 2$ in this example refers to the fact that the data points from stencil $S_i^{(2)} = \{I_{i-2}, I_{i-1}, I_i\}$ have been used. The coefficients c_{wj} in (3.49) corresponding to the four candidate stencils $S_i^{(w)}, w = -1, 0, 1, 2$ which are listed in a Table 3.1. The information in Table 3.1 can be seen in many papers of Chi Wang Shu, for example "*Essentially non-oscillatory and weighted essentially non-oscillatory schemes for hyperbolic conservation laws*", see Shu (1997).

Extension to two-dimensional space

We recall the semidiscrete form of the two-dimensional advection problem (3.27) with constant velocity field

$$
\frac{\partial Q}{\partial t} = -\frac{1}{\Delta x}\left(\hat{F}_{i+1/2,j} - \hat{F}_{i-1/2,j}\right) - \frac{1}{\Delta z}\left(\hat{G}_{i,j+1/2} - \hat{G}_{i,j-1/2}\right),
$$

Table 3.1 The ENO coefficients c_{wj} in (3.49).

k	w	$j = 0$	$j = 1$	$j = 2$
1	-1	1		
	0	1		
2	-1	3/2	-1/2	
	0	1/2	1/2	
	1	-1/2	3/2	
3	-1	11/6	-7/6	1/3
	0	1/3	5/6	-1/6
	1	-1/6	5/6	1/3
	2	1/3	-7/6	11/6

where $\hat{F}_{i\pm1/2,j} \approx f_{i\pm1/2,j}$ and $\hat{G}_{i,j\pm1/2} \approx g_{i,j\pm1/2}$. The numerical fluxes $\hat{F}_{i\pm1/2,j}$ and $\hat{G}_{i,j\pm1/2}$ can be constructed from the one-dimensional ENO algorithm dimension by dimension. This means that we could simply take the data points of physical flux $f_{i,j}$ for fixed j, and the one dimensional ENO reconstruction algorithm described above, to obtain an approximation of $\partial f/\partial x$ at the point (x_i, z_j). Similarly, the approximation to $\partial g/\partial z$ can be obtained by taking the data points of physical flux $g_{i,j}$ for fixed i, and use the same one-dimensional ENO reconstruction. The time required to compute the approximation $\partial f/\partial x + \partial g/\partial z$ is thus just twice that of the one-dimensional evaluation of $\partial f/\partial x$ for each grid point.

3.2.4 Weighted stencil schemes: WENO

Finite difference weighted essentially non-oscillatory schemes (WENO) have proven to be effective in capturing structures of problems involving steep gradi-
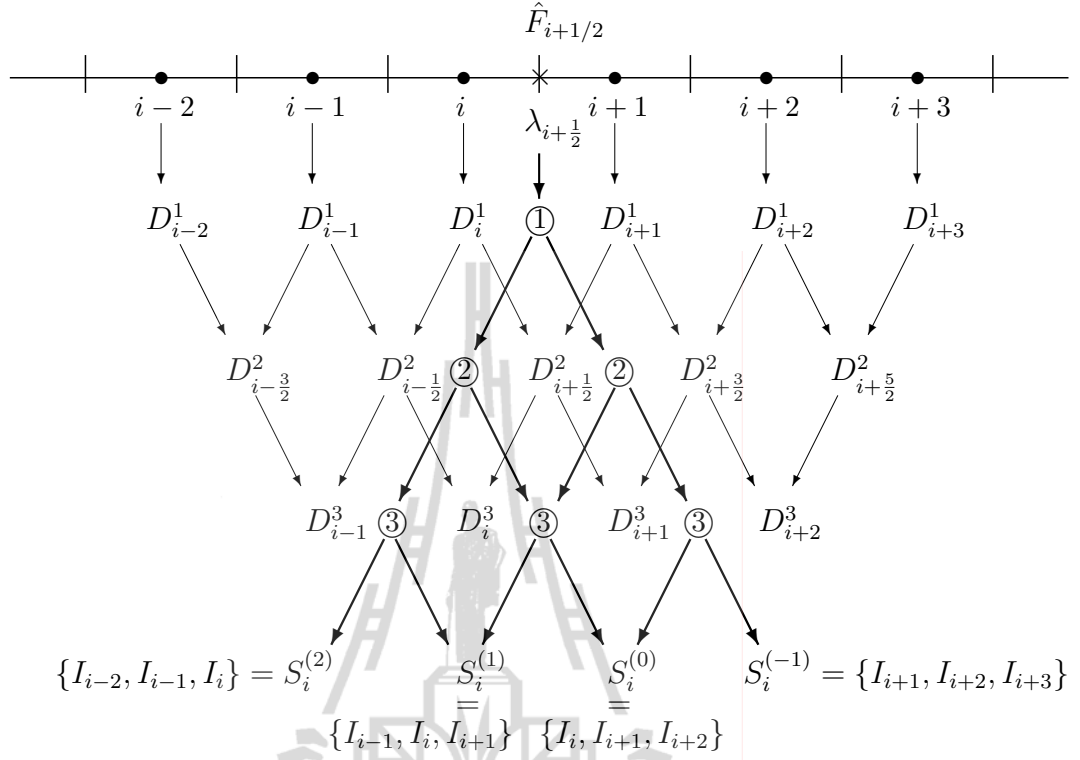
Figure 3.5 Flowchart of ENO algorithm. Note that D_i^l denotes $D_i^l H$.

ents and discontinuities, see Jiang and Shu (1996), Shu (1997), Balsara and Shu (2000). The classical WENO schemes were designed to use a dynamic set of stencils, where a nonlinear convex combination of lower-order polynomials adapts either to a higher-order approximation at smooth parts of the solution, or to an upwind spatial discretization that avoids interpolation across discontinuities. The nonlinear coefficients of convex combination, hereafter referred to as nonlinear weights ω, are based on the local smoothness indicators (β). An essentially zero weight is assigned to those lower-order polynomials whose underlining stencils contain high gradients and/or discontinuities, yielding an essentially non-oscillatory solution at and near discontinuities. At smooth parts of the solution, higher-order is achieved through the mimicking of the central upwinding scheme of maximum order, when all smoothness indicators are about the same size. The classical WENO scheme designs are based on the ENO schemes of Harten et al. (1987).

In this thesis, fifth order WENO (or WENO5) schemes are applied to approximate convective terms. The WENO5 scheme uses the nonlinear convex combination based on ENO3 stencils depending on upwinding. If the wind blows from left to right, $\{S_i^{(0)}, S_i^{(1)}, S_i^{(2)}\}$ will be used. Otherwise, $\{S_i^{(-1)}, S_i^{(0)}, S_i^{(1)}\}$ will be used. Here we use $\lambda_{i+1/2} = f'(Q)$ to distinguish the direction of wind. If $\lambda_{i+1/2} > 0$ (positive direction or wind blows to the right), WENO5 for $\hat{F}_{i+1/2}$ based on the ENO3 stencils can be expressed as

$$\hat{F}_{i+1/2} = \sum_{w=0}^{2} \omega_w f_{i+1/2}^{(w)}, \tag{3.50}$$

$$\omega_w = \frac{\alpha_w}{\sum_{l=0}^{2} \alpha_l}, \tag{3.51}$$

$$\alpha_w = \frac{d_w}{(\varepsilon + \beta^{(w)})^2}, \tag{3.52}$$

$$(d_0, d_1, d_2) = \left(\frac{3}{10}, \frac{3}{5}, \frac{1}{10}\right), \tag{3.53}$$

where $f_{i+1/2}^{(w)}$ approximates $\hat{F}_{i+1/2}$ using cell stencil $S_i^{(w)}, w = 0, 1, 2$. The parameter $\varepsilon = 10^{-6}$ is used to avoid zero denominator and $\beta^{(w)}$ is a smoothness indicator of the stencil $S^{(w)}$ for positive direction. The third order numerical fluxes are given below:

$$\begin{aligned}
f_{i+1/2}^{(0)} &= \frac{1}{3}f_i + \frac{5}{6}f_{i+1} - \frac{1}{6}f_{i+2}, \\
f_{i+1/2}^{(1)} &= -\frac{1}{6}f_{i-1} + \frac{5}{6}f_i + \frac{1}{3}f_{i+1}, \\
f_{i+1/2}^{(2)} &= \frac{1}{3}f_{i-2} - \frac{7}{6}f_{i-1} + \frac{11}{6}f_i.
\end{aligned} \tag{3.54}$$

They are the results from ENO3 schemes coresponding to stencils $S_i^{(0)}, S_i^{(1)}$ and $S_i^{(2)}$, respectively. In addition, the smoothness indicators $\beta^{(w)}$ in terms of point values of f are given by

$$\begin{aligned}
\beta^{(0)} &= \frac{13}{12}(f_i - 2f_{i+1} + f_{i+2})^2 + \frac{1}{4}(3f_i - 4f_{i+1} + f_{i+2})^2, \\
\beta^{(1)} &= \frac{13}{12}(f_{i-1} - 2f_i + f_{i+1})^2 + \frac{1}{4}(f_{i-1} - f_{i+1})^2, \\
\beta^{(2)} &= \frac{13}{12}(f_{i-2} - 2f_{i-1} + f_i)^2 + \frac{1}{4}(f_{i-2} - 4f_{i-1} + 3f_i)^2.
\end{aligned} \tag{3.55}$$

If $\lambda_{i+1/2} < 0$ (negative direction), the construction of WENO5 for $\hat{F}_{i+1/2}$ plays the same role as positive direction, but the three stencils of ENO3 have changed to $\{S_i^{(-1)}, S_i^{(0)}, S_i^{(1)}\}$. Therefore, the WENO5 scheme for negative direction can be expressed as follows,

$$\hat{F}_{i+1/2} = \sum_{w=-1}^{1} \tilde{\omega}_w f_{i+1/2}^{(w)} \tag{3.56}$$

$$\tilde{\omega}_w = \frac{\tilde{\alpha}_w}{\sum_{l=-1}^{1} \tilde{\alpha}_l} \tag{3.57}$$

$$\tilde{\alpha}_w = \frac{\tilde{d}_w}{(\varepsilon + \tilde{\beta}^{(w)})^2} \tag{3.58}$$

$$(\tilde{d}_{-1}, \tilde{d}_0, \tilde{d}_1) = \left(\frac{1}{10}, \frac{3}{5}, \frac{3}{10}\right), \tag{3.59}$$

where $f_{i+1/2}^{(w)}$ approximates $\hat{F}_{i+1/2}$ using cell stencil $S_i^{(w)}, w = -1, 0, 1$. The $\tilde{\beta}_w$ is a smoothness indicator of the stencil $S^{(w)}$ for negative direction. The third order numerical fluxes for negative direction are given as follows,

$$
\begin{aligned}
f_{i+1/2}^{(-1)} &= \frac{11}{6} f_{i+1} - \frac{7}{6} f_{i+2} + \frac{1}{3} f_{i+3}, \\
f_{i+1/2}^{(0)} &= \frac{1}{3} f_i + \frac{5}{6} f_{i+1} - \frac{1}{6} f_{i+2}, \\
f_{i+1/2}^{(1)} &= -\frac{1}{6} f_{i-1} + \frac{5}{6} f_i + \frac{1}{3} f_{i+1},
\end{aligned} \tag{3.60}
$$

with the smoothness indicators $\tilde{\beta}^{(w)}$ express in terms of f are given below

$$
\begin{aligned}
\tilde{\beta}^{(-1)} &= \frac{13}{12}(f_{i+1} - 2f_{i+2} + f_{i+3})^2 + \frac{1}{4}(3f_{i+1} - 4f_{i+2} + f_{i+3})^2, \\
\tilde{\beta}^{(0)} &= \frac{13}{12}(f_i - 2f_{i+1} + f_{i+2})^2 + \frac{1}{4}(f_i - f_{i+2})^2, \\
\tilde{\beta}^{(1)} &= \frac{13}{12}(f_{i-1} - 2f_i + f_{i+1})^2 + \frac{1}{4}(f_{i-1} - 4f_i + 3f_{i+1})^2.
\end{aligned} \tag{3.61}
$$

The general idea of the weights definition in (3.51) and (3.57) is that on smooth parts of the solution the smoothness indicators β are all small and

about the same size, generating weights ω that are good approximations to the ideal weights d. On the other hand, if the stencil contains a discontinuity, β is $O(1)$ and the corresponding weight ω is small relative to the other weights.

Extension to two-dimensional space

We consider the two-dimensional advection equation (3.27) again. The numerical fluxes $\hat{F}_{i\pm1/2,j}$ and $\hat{G}_{i,j\pm1/2}$ in semidiscrete form (3.50) can be obtained by using the one-dimensional WENO algorithm dimension by dimension. As in the one-dimensional WENO described above, we can construct numerical flux $\hat{G}_{i,j+1/2}$ by using $\lambda_{i,j+1/2} = g'(Q)_{i,j+1/2}$ to distinguish the wind direction and using physical flux $g_{i,j}$ with i fixed instead of using f. For example, if $\lambda_{i,j+1/2} = g'(Q)_{i,j+1/2} > 0$, the numerical flux $\hat{G}_{i,j+1/2}$ will be computed

$$\hat{G}_{i,j+1/2} = \sum_{w=0}^{2} \omega_w g_{i,j+1/2}^{(w)}, \qquad (3.62)$$

$$\omega_w = \frac{\alpha_w}{\sum_{l=0}^{2} \alpha_l}, \alpha_w = \frac{d_w}{(\varepsilon + \beta^{(w)})^2}, (d_0, d_1, d_2) = (\frac{3}{10}, \frac{3}{5}, \frac{1}{10})$$

where $g_{i,j+1/2}^{(w)}$ approximates $\hat{G}_{i,j+1/2}$ using cell stencil $S_j^{(w)}, w = 0, 1, 2$.

$$\begin{aligned}
g_{i,j+1/2}^{(0)} &= \frac{1}{3}g_{i,j} + \frac{5}{6}g_{i,j+1} - \frac{1}{6}g_{i,j+2}, \\
g_{i,j+1/2}^{(1)} &= -\frac{1}{6}g_{i,j-1} + \frac{5}{6}g_{i,j} + \frac{1}{3}g_{i,j+1}, \\
g_{i,j+1/2}^{(2)} &= \frac{1}{3}g_{i,j-2} - \frac{7}{6}g_{i,j-1} + \frac{11}{6}g_{i,j}.
\end{aligned} \qquad (3.63)$$

The smoothness indicators are given below

$$\begin{aligned}
\beta^{(0)} &= \frac{13}{12}(g_{i,j} - 2g_{i,j+1} + g_{i,j+2})^2 + \frac{1}{4}(3g_{i,j} - 4g_{i,j+1} + g_{i,j+2})^2, \\
\beta^{(1)} &= \frac{13}{12}(g_{i,j-1} - 2g_{i,j} + g_{i,j+1})^2 + \frac{1}{4}(g_{i,j-1} - g_{i,j+1})^2, \\
\beta^{(2)} &= \frac{13}{12}(g_{i,j-2} - 2g_{i,j-1} + g_{i,j})^2 + \frac{1}{4}(g_{i,j-2} - 4g_{i,j-1} + 3g_{i,j})^2.
\end{aligned} \qquad (3.64)$$

3.3   Numerical examples

In this section, we demonstrate several examples of 1D and 2D linear problems that validate the rate of convergence of the advection schemes presented in the previous section. All of the velocity fields used in these computations have the property that simply evaluating the velocity at the cell interfaces gives discrete values satisfying the discrete divergence-free condition. A uniform grid is used for all computations.

Example 1. The first test is the one-dimensional advection equation with constant velocity of an initial data containing discontinuity. We observe behaviors of the advection schemes,

$$q_t + aq_x = 0. \tag{3.65}$$

The analytical solution of the above equation is $q = f(x - at)$, where $f(x)$ is the initial distribution of q given by

$$f(x) = \begin{cases} 1, & x \leq 0, \tag{3.66} \\ 0, & x > 0. \tag{3.67} \end{cases}$$

The solution describes a wave propagating in the positive x-direction (if $a > 0$) with velocity a. Numerical results from advection schemes are shown in Figure 3.6 for a fixed velocity $a = 1.0$, uniform grid spacing $\Delta x = 0.2$ for the domain $x \in [-1, 20]$. We compute the solutions up to time $t = 10.0$; at this time the front is moving through $x = 10.0$ from its initial position at $x = 0$. For all the computation, a boundary condition is the Dirichlet boundary conditions, $q(-1) = 1$ and $q(20) = 0$.

We are using the Courant number $C_{cour} = 0.1$ for numerical comparison because our main interest is in various spatial difference schemes for convection. Since all the compared schemes are not second order accurate in time, in order

to avoid numerical errors due to discretization in time as far as possible, we have chosen such a small Courant number.

We can see that the classical first order upwind (UPW) scheme is more diffusive than others schemes and the solution smeared out because of the inherent numerical diffusion of this scheme. The schemes with limiters - minmod, superbee, Van Leer and MC limiters, improve the UPW scheme. The superbee limiter has been shown to be better than other limiters. As expected, the results from the 2nd-order SMIF, the 3rd-order ENO3 and the 5th-order WENO5 schemes are better than the UPW scheme. The best among those advection schemes are the WENO5 scheme and the superbee limiter.

Example 2. Next example was used as a test problem in a paper by LeVeque (1996). It is a two-dimensional advection equation on a unit rectangular domain $[0, 1] \times [0, 1]$ with smooth initial data (see Figure 3.7) and steady velocity field given below

$$q(x, y, 0) = \sin(2\pi x)\sin(2\pi y), \tag{3.68}$$

with constant velocities

$$u(x, y, t) = 1, \ v(x, y, t) = 2. \tag{3.69}$$

The periodic boundary conditions are used in this case and we compute up to time $t = 1.0$ at which the solution coincides with the initial data. The time step $\Delta t = 0.4\Delta x$, ($C_{cour} = 0.8$), is used for all runs. Figure 3.8 shows a plot of 1-norm error vs. grid spacing Δx in a log-log scale for a sequence of grids with $\Delta x = 0.05, \ 0.025, \ 0.0125$.
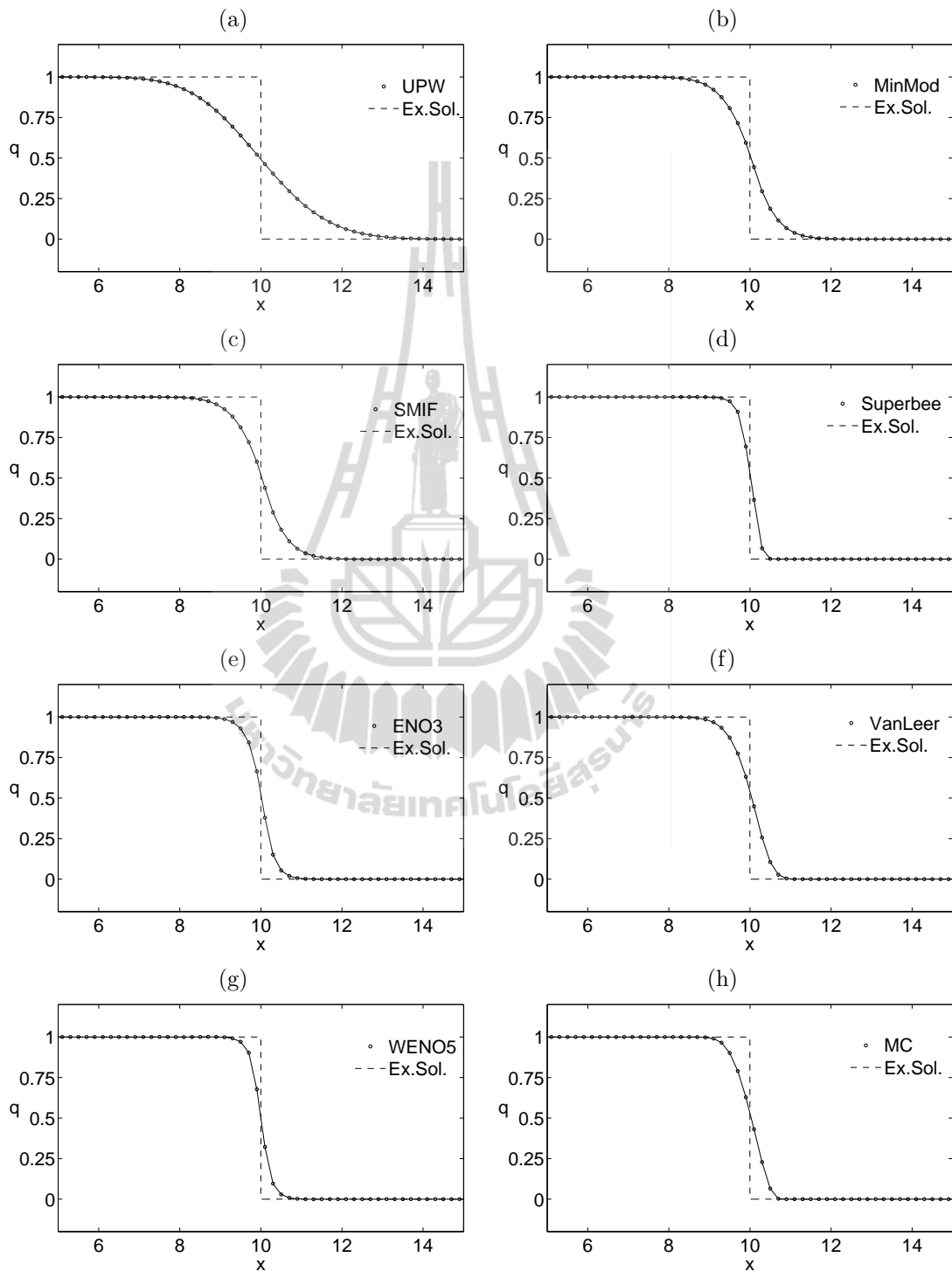
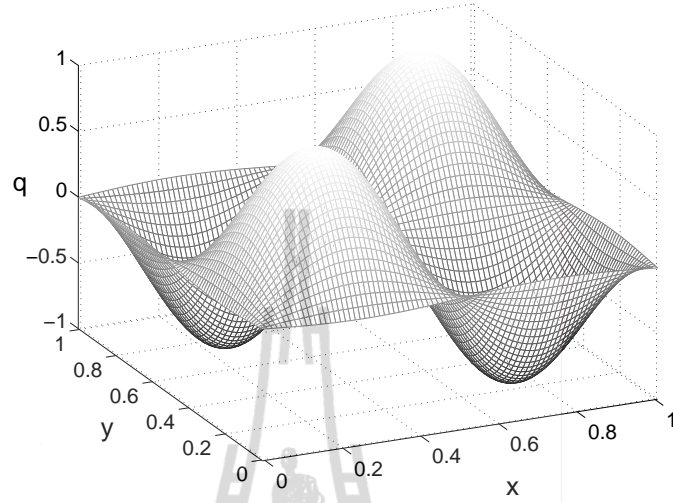**Figure 3.6** Results of numerical computations for *Example 1.*, $C_{cour} = 0.1$, resulting at $t = 10$.

Figure 3.7 Graphics of initial data for *Example 2.*

Table 3.2 shows the order of accuracy observed from each advection scheme in both the 1-norm[1] and the max-norm[2]. We note that, the first order UPW scheme is unstable with this time step. The order of each scheme is computed from finer and finest grids by the following formula

$$order = \log_2(E(\Delta x)/E(\Delta x/2)), \tag{3.70}$$

where $E(\Delta x)$ is the norm of the error with grid spacing Δx, relative to the true solution.

Data in Table 3.2 demonstrate the expected rate of convergence for all schemes. The WENO5 scheme is better than the other advection schemes as can be seen by the results in Figure 3.8 and Table 3.2. We note that the Minmod, Superbee and Van Leer limiters have rates of convergence a little bit more than one.

---

[1]1-norm: $\| \cdot \|_1 = \dfrac{\sum_{i=1}^{N_x} \sum_{j=1}^{N_y} | q_{ij}^{approx} - q_{ij}^{exact} |}{N_x N_y}$, N_x, N_y – total grid points in both directions.

[2]max-norm $:= \| \cdot \|_\infty = \max_{ij} | q_{ij}^{approx} - q_{ij}^{exact} |$
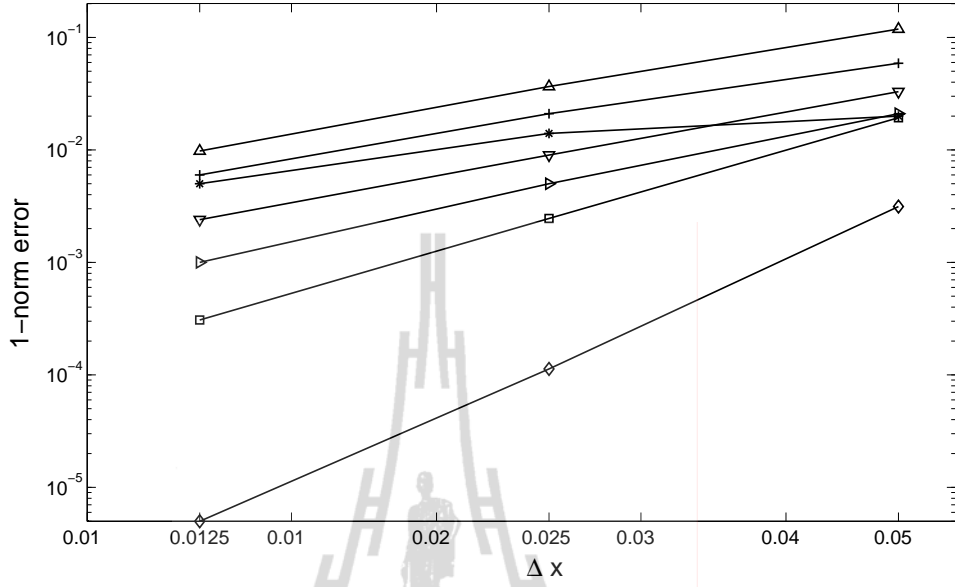
Figure 3.8 Log-log plot of the 1-norm error versus grid spacing ($\Delta x = 0.0125, 0.025, 0.05$) with $C_{cour} = 0.8$ and computed results at time $t = 1.0$; $+$ – Minmod, $*$ – Superbee, $\triangledown$ – Van Leer, $\triangleright$ – MC, $\triangle$ – SMIF, $\square$ – ENO3, $\diamond$ – WENO5.

Table 3.2 Order of accuracy for *Example 2.*, $C_{cour} = 0.8$, orders are computed from the errors of finer ($\Delta x = 0.025$) and finest ($\Delta x = 0.0125$) grids.

Methods	max-norm	1-norm
UPW-1st order	–	–
UPW-Minmod	1.23	1.81
UPW-Superbee	1.01	1.49
UPW-VanLeer	1.39	1.91
UPW-MC	0.68	0.69
SMIF	1.84	1.90
ENO3	2.99	3.00
WENO5	4.64	4.50

CHAPTER IV

NUMERICAL RESULTS

The collapse of a plane mixed region in a stratified medium of continuous density is analyzed here using direct simulation of the Navier-Stokes equations in the Oberbeck-Boussinesq approximation. In the fully mixed case the discontinuity in the density at the edge of the mixed region is helpful in distinguishing the fluid interior to the mixed region from that exterior to the region. In other words, it allows to study the dynamics of the mixed region spot. The numerical approximation of the advective process in presence of sharp gradients (or discontinuities) is very important in these cases.

The experiment of Wu (1969), Figure 4.1, presents the most complete data concerning the collapse of a mixed region in the two-dimensional case. The data of Wu's laboratory experiment (Wu (1969)) are used for assessment of a high-order finite difference upwind scheme for the simulation of convective terms in the Navier-Stokes equations. He assumed that there are three stages of collapse, "initial", "principal" and "final" collapse stages, respectively. He pointed that the collapse during the initial and principal stages is primarily a gravitational flow phenomenon, and that the collapse process during these stages is identical for all tests with different density stratifications. The Figure 4.2 depicts the profiles of collapse at several time. And, the Figure 4.3 are camera snapshots of Wu's experimental data. In these pictures present the internal waves of density induced by mixed region collapse in the stratified fluid.
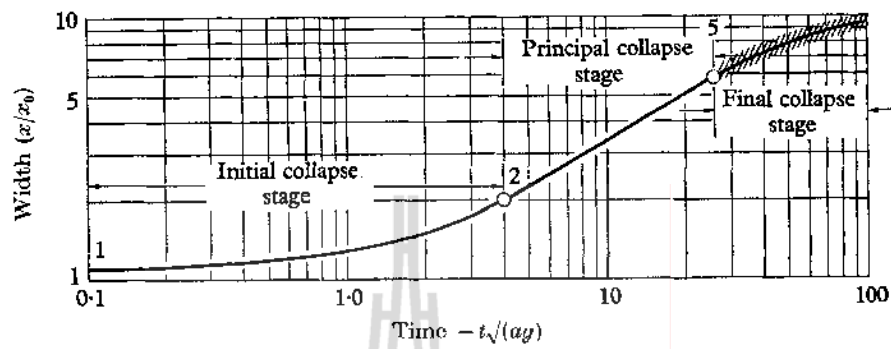
Figure 4.1 The experimental data of Wu (1969): stages of collapse.
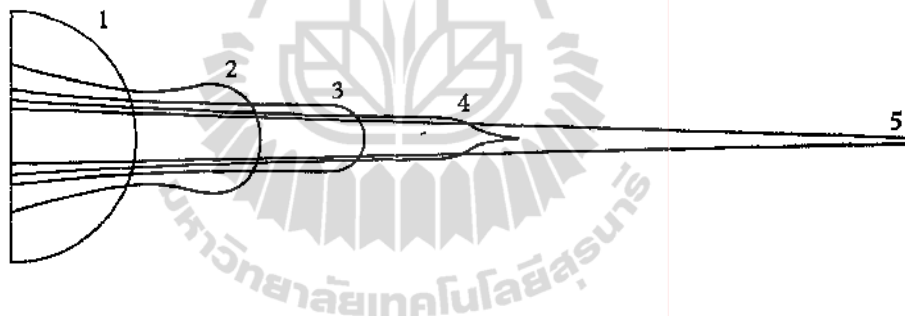

Figure 4.2 The profiles of collapse from Wu (1969).

$t\sqrt{(ag)} = 4$ $t\sqrt{(ag)} = 8$ $t\sqrt{(ag)} = 29$
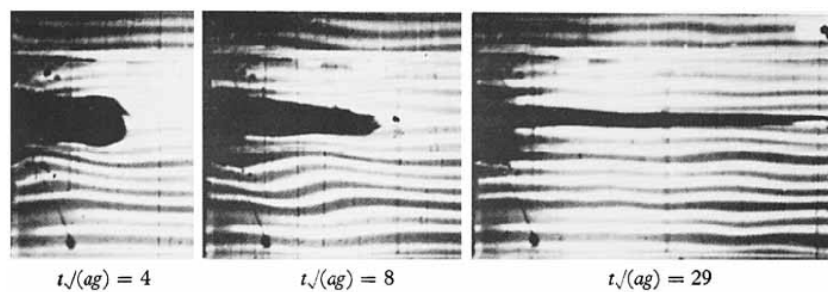
Figure 4.3 Collapse of the mixed region and subsequent generation of the internal waves.

4.1 Width, profiles and areas of collapsing region.

In the experiments of Wu (1969), profiles of the collapsing region are traced by tagging the mixed region fluid with dye. In our numerical computations profiles of collapsing region was traced from evolution of a passive scalar and from the evolution of Lagrangian particles positions. Finite difference schemes have a different smearing of density and passive scalar discontinuities.

To define the evolution of the mixing region we analyzed the profiles of a passive scalar at different transects. Figure 4.4 shows the graphs of the passive scalar at transect $z = 0.5\Delta z$ ($C(t, x, 0.5\Delta z)$) for different moments of time. Here we compare flux-limiter schemes with four limiters given by equations (3.26) and the first order upwind scheme (no limiter). The first order upwind scheme smears the solution too much (see lines marked by ○). The limiter schemes reduce the numerical diffusion comparing to the upwind scheme. Comparing the performance of the Van Leer and MC limiters (lines marked by ∇ and $\triangleright$, respectively) nearly identical results are seen and a negligible numerical diffusion is introduced compared to the one introduced by Minmod limiter (lines marked by $+$). The Superbee limiter (lines marked by $*$) gives better results concerning limitation of the numerical diffusion.

Figures 4.5 shows the graphs of $C(t, x, 0.5\Delta z)$ for different moments of time. Here we compare four schemes - Superbee flux-limiter, SMIF, ENO3 and WENO5. For the time interval up to $t \simeq 4$ there are almost no differences in performance. For larger time, $t \geq 6$ the Superbee limiter gives the smallest numerical diffusion compared with SMIF, ENO3 and WENO5. Performance of ENO3 and SMIF are nearly identical as seen from data on Figure 4.5. The WENO5 scheme produces smaller numerical diffusion compared with ENO3 and SMIF.
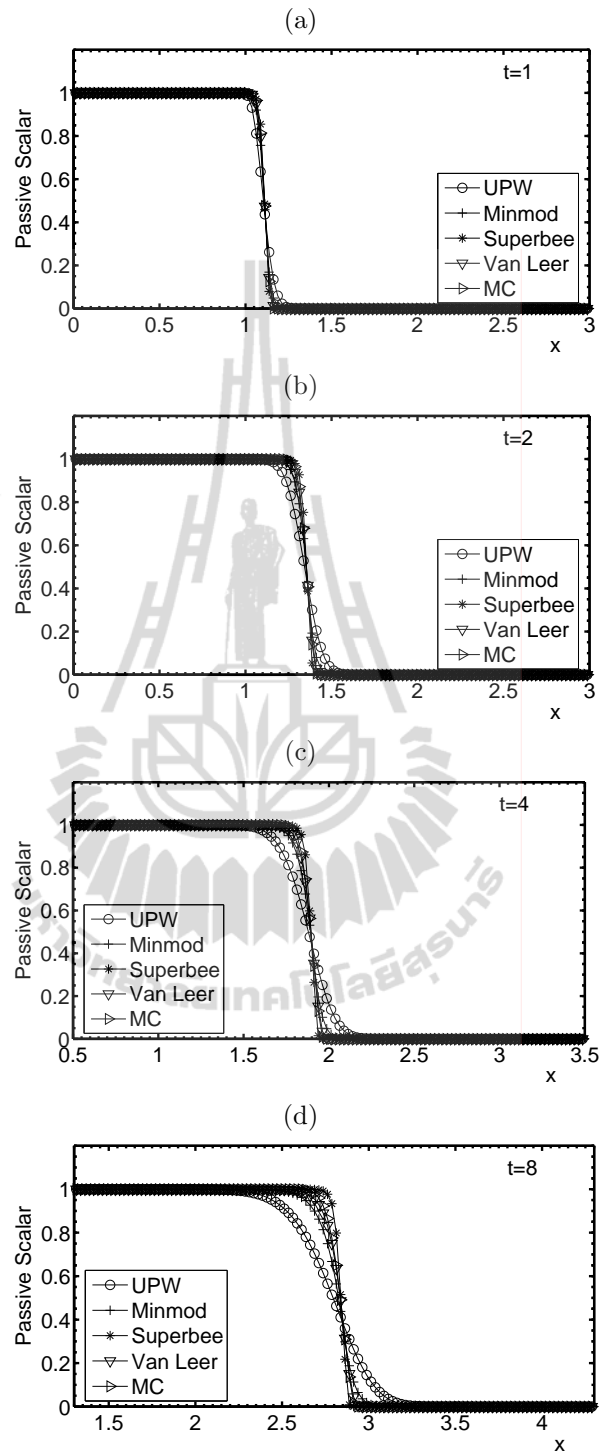
Figure 4.4 Comparison of first-order upwind and flux-limiter scheme with four limiters in the case of $Re = 10^3$, $\Delta x = \Delta z = 0.025$, $\Delta t = 0.0005$, computational domain is $[0, 10] \times [0, 4]$. Marks: $\circ$ –first-order monotone scheme (UPW), $+$ – Minmod, $*$ – Superbee, ∇ – Van Leer, $\triangleright$ – MC.

(e)

(f)

(g)

(h)

Figure 4.4   Continued.

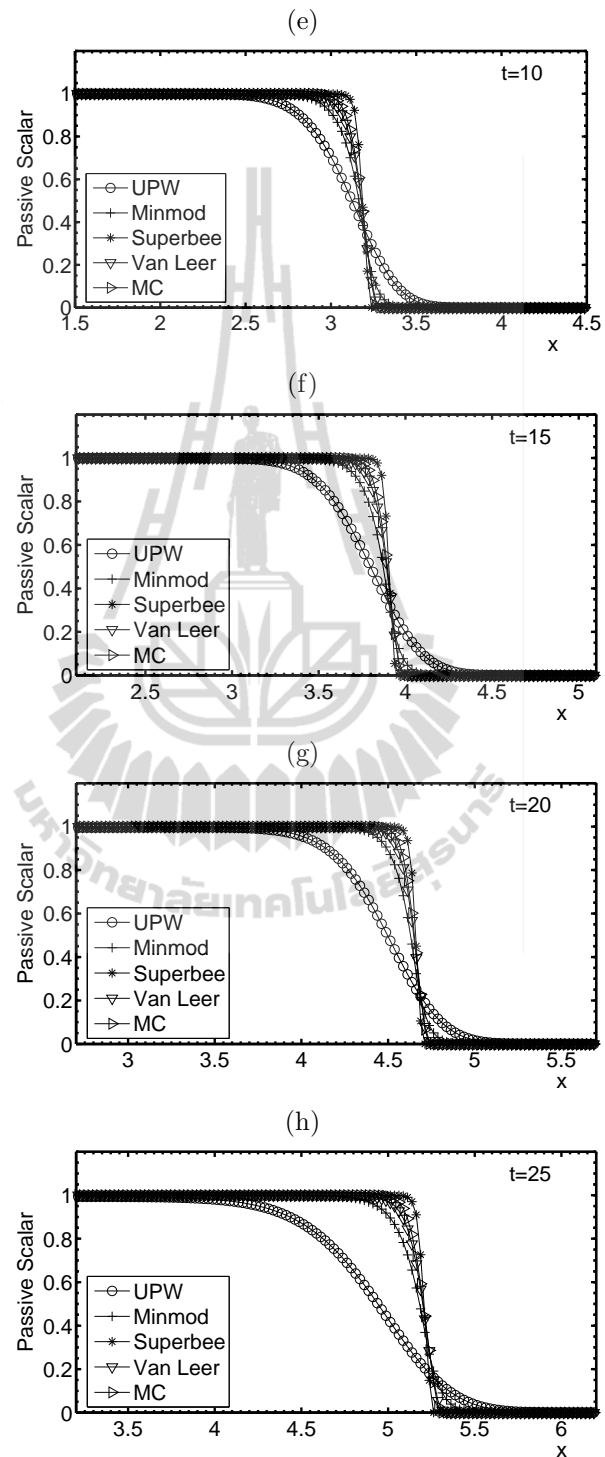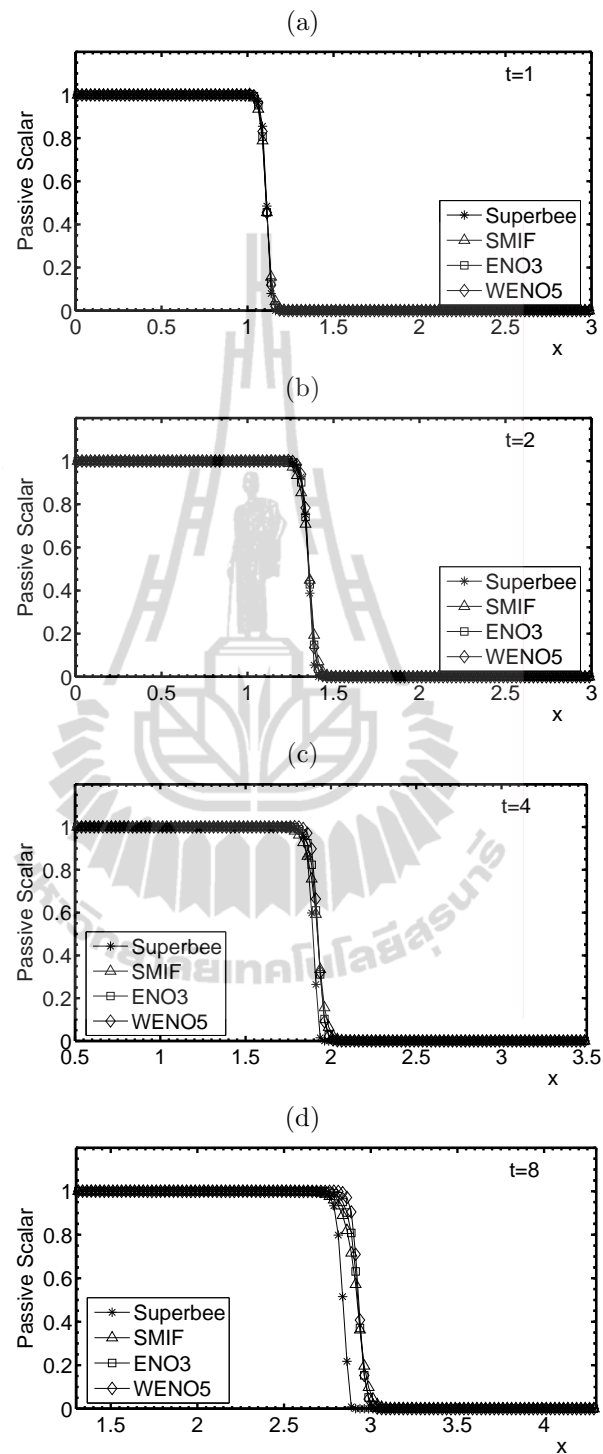**Figure 4.5** Comparison of four approximations of convective term in the case of $Re = 10^3$, $\Delta x = \Delta z = 0.025$, $\Delta t = 0.0005$, computational domain is $[0, 10] \times [0, 4]$. Marks: $*$ – flux-limiter/Superbee, $\triangle$ – SMIF, $\square$ – ENO3, $\diamond$ – WENO5.
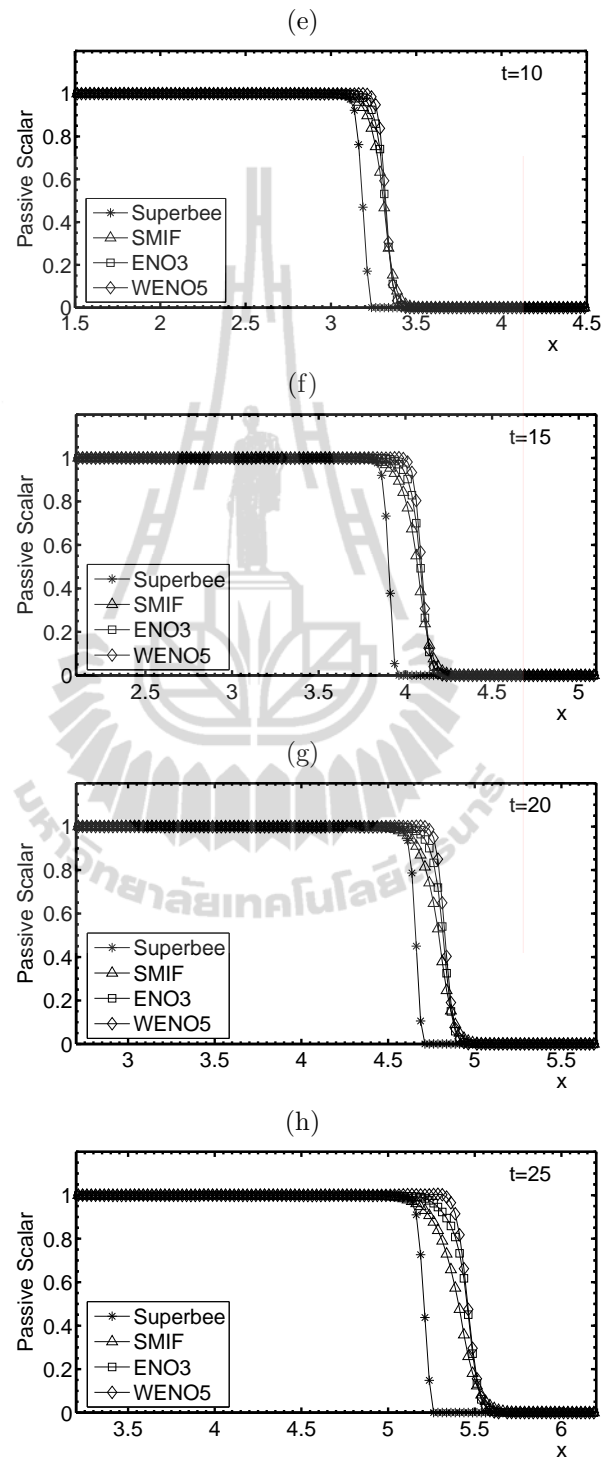
(e)

(f)

(g)

(h)

Figure 4.5   Continued.
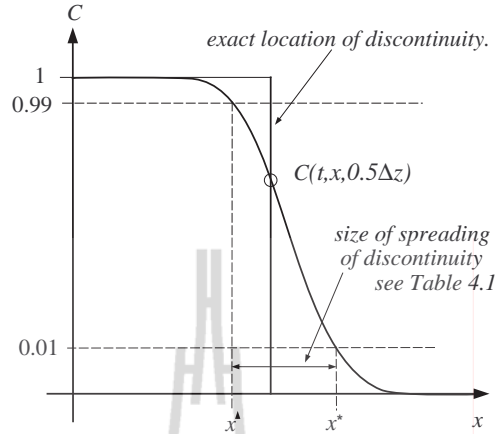
Figure 4.6 A diagram of approach to track location of discontinuity in passive scalar.

Figures 4.7 and 4.8 illustrate the temporal history of the mixed region width. The stars and triangles are the results of numerical simulations computed herein. The dashed line is drawn according to Wu's original experimental data in the log-log scales (see Figure 4.1 and see more details in Wu (1969)). The solid curve is made up of two functions:

$$
x = \begin{cases} 1 + 0.29t^{1.08} & \text{for } 0 \leq t < 2.75, \\[2mm] 1.03t^{0.55} & \text{for } 2.75 \leq t \leq 25, \end{cases} \tag{4.1}
$$

which were found by Wu to fit his experimental data. Our numerical data are presented by two signs: stars (*) and filled triangles ($^\blacktriangle$). The star signs represent the points x^*, which are the intersection of curve $C(t, x, 0.5\Delta z)$ and line $C = 0.01$. The filled triangle signs represent the points $x^\blacktriangle$, which are the intersection of curve $C(t, x, 0.5\Delta z)$ and line $C = 0.99$. Because all schemes smear the discontinuity across several cells, we assume that the actual location of the discontinuity (edge of mixing zone) is located between this two points x^* and $x^\blacktriangle$. The readers are referred to Figure 4.6 for an illustration.

Results of our numerical experiments in Figures 4.7 and 4.8 correspond to the following values of parameters $Re = 10^3, \Delta x = \Delta z = 0.025, \Delta t = 0.0005$, and the computational domain include 400×160 cells. Figure 4.7 demonstrates a comparison of $1^{st}-$order and four flux-limiter schemes. One can see that the first-order upwind scheme and the flux-limiter scheme with Minmod limiter have largest numerical diffusion. Points x^* are located closer to Wu's experimental data. For all schemes, the points $x^{\blacktriangle}$ located below Wu's experimental data.

Figure 4.8 shows a comparison of four schemes. One of them is the flux-limiter scheme with Superbee limiter and the others are the two adaptive stencil schemes (SMIF and ENO3) and weight stencil scheme (WENO5). Our numerical results agree quite well with Wu's experimental data (dashed curves in Figures 4.7 and 4.8). To more clear, zoomed pictures of selected timed greater than 10 of Figures 4.7 and 4.8 are presented in Figures 4.9 and 4.10, respectively.

Table 4.1 shows the size of spread of discontinuity $(x^* - x^{\blacktriangle})$ for three different grids with $\Delta x = \Delta z = 0.1, 0.05$ and 0.025. The grid with $\Delta x = \Delta z = 0.1$ is too coarse as can be seen from the third column of Table 4.1. For large instants of time $t = 20$ the distance between x^* and $x^{\blacktriangle}$ become large. In the case of the WENO5 scheme, this problem is related with monotonicity. For the finest grid with $\Delta x = \Delta z = 0.025$ numerical viscosity spreads the discontinuity over approximately ten computation cells for the schemes with a flux-limiter, SMIF, ENO3 and WENO5. The flux-limiter with Superbee limiter scheme has the smallest numerical diffusion and correspondingly demonstrates the smallest spread of the discontinuity which increases with increasing time by only a few percent. The size of the spread of discontinuity by first order upwind scheme increases with increasing times is up to 80%. In this case, it is difficult to predict the actual location of the discontinuity. Data in Table 4.1, and Figures 4.7 and 4.8 show that

the flux-limiter scheme with Superbee limiter gives a width of the mixed region a little bit smaller than Wu's experimental data, but at the same time, this scheme has the smallest numerical diffusion and the smallest size of spread of discontinuity $(x^* - x^{\blacktriangle})$. The ENO3 and SMIF schemes gave nearly identical widths of the mixed region. The WENO5 scheme gives results closer to Wu's experimental data.

Table 4.1 Size of spreading of discontinuity for three meshes, $x^* - x^{\blacktriangle}$.

Times (t)	Methods	$x^* - x^{\blacktriangle}$		
		$\Delta x = \Delta z = 0.1$ $\Delta t = 0.01$	$\Delta x = \Delta z = 0.05$ $\Delta t = 0.001$	$\Delta x = \Delta z = 0.025$ $\Delta t = 0.0005$
2	UPW-1st order	0.737	0.528	0.383
	Flux-Limiter/Minmod	0.563	0.373	0.244
	Flux-Limiter/Superbee	0.441	0.236	0.138
	Flux-Limiter/Van Leer	0.472	0.290	0.186
	Flux-Limiter/MC	0.453	0.270	0.148
	SMIF	0.540	0.344	0.219
	ENO3	0.440	0.278	0.170
	WENO5	0.427	0.257	0.156
10	UPW-1st order	2.902	1.846	1.051
	Flux-Limiter/Minmod	2.192	0.850	0.551
	Flux-Limiter/Superbee	0.669	0.309	0.148
	Flux-Limiter/Van Leer	1.130	0.598	0.361
	Flux-Limiter/MC	0.782	0.452	0.274
	SMIF	2.281	0.612	0.362
	ENO3	3.288	0.437	0.249
	WENO5	0.537	0.336	0.184
20	UPW-1st order	4.298	5.014	1.294
	Flux-Limiter/Minmod	4.000	0.881	0.523
	Flux-Limiter/Superbee	4.113	0.246	0.139
	Flux-Limiter/Van Leer	4.506	0.544	0.318
	Flux-Limiter/MC	4.298	0.388	0.237
	SMIF	4.085	0.785	0.452
	ENO3	3.924	0.855	0.295
	WENO5	3.905	0.360	0.202

Figure 4.7 Comparison with Wu's data, $Re = 10^3$, $\Delta x = \Delta z = 0.025$, $\Delta t = 0.0005$, domain is $[0, 10] \times [0, 4]$. $*$, $\blacktriangle$ correspond to $C(t, x^*, 0.5\Delta z) = 0.01$, $C(t, x^{\blacktriangle}, 0.5\Delta z) = 0.99$, respectively; solid lines represent formulae (4.1), dashed lines correspond to Wu's experimental data, Wu (1969).
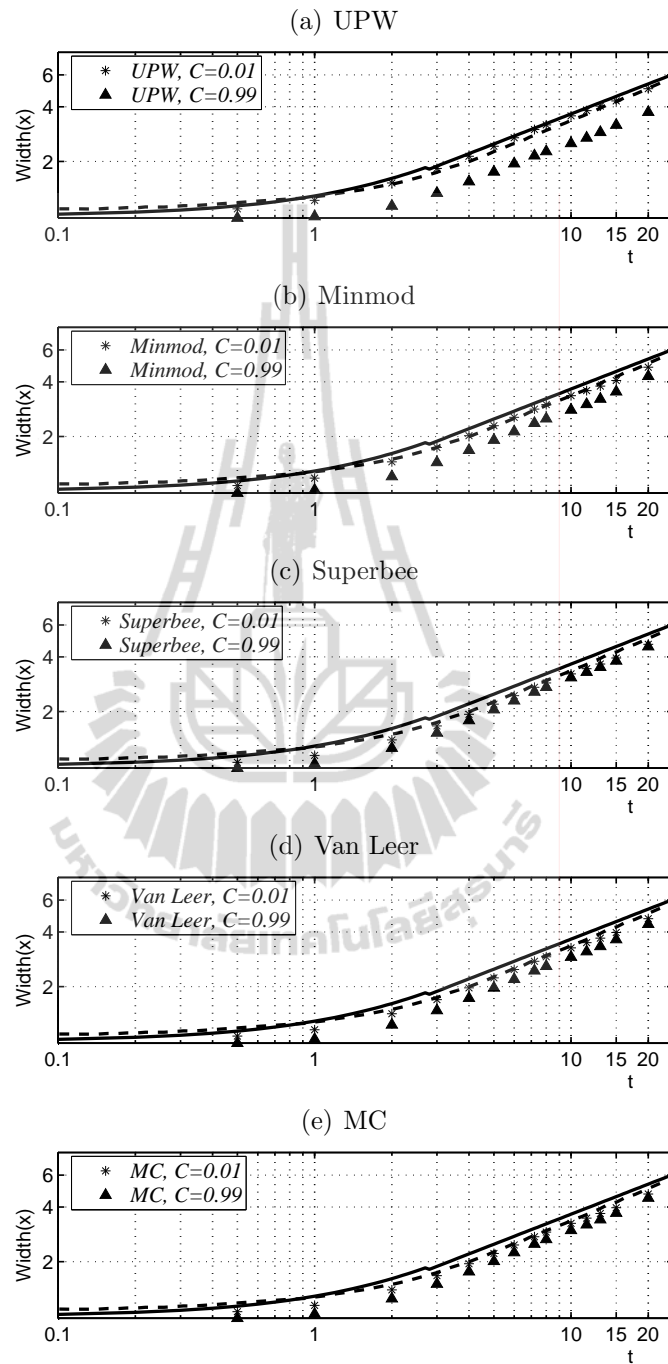
Figure 4.8 Comparison with Wu's data, $Re = 10^3$, $\Delta x = \Delta z = 0.025$, $\Delta t = 0.0005$, domain is $[0, 10] \times [0, 4]$. $*$, $\blacktriangle$ correspond to $C(t, x^*, 0.5\Delta z) = 0.01$, $C(t, x^{\blacktriangle}, 0.5\Delta z) = 0.99$, respectively; solid lines represent formulae (4.1), dashed lines correspond to Wu's experimental data, Wu (1969).
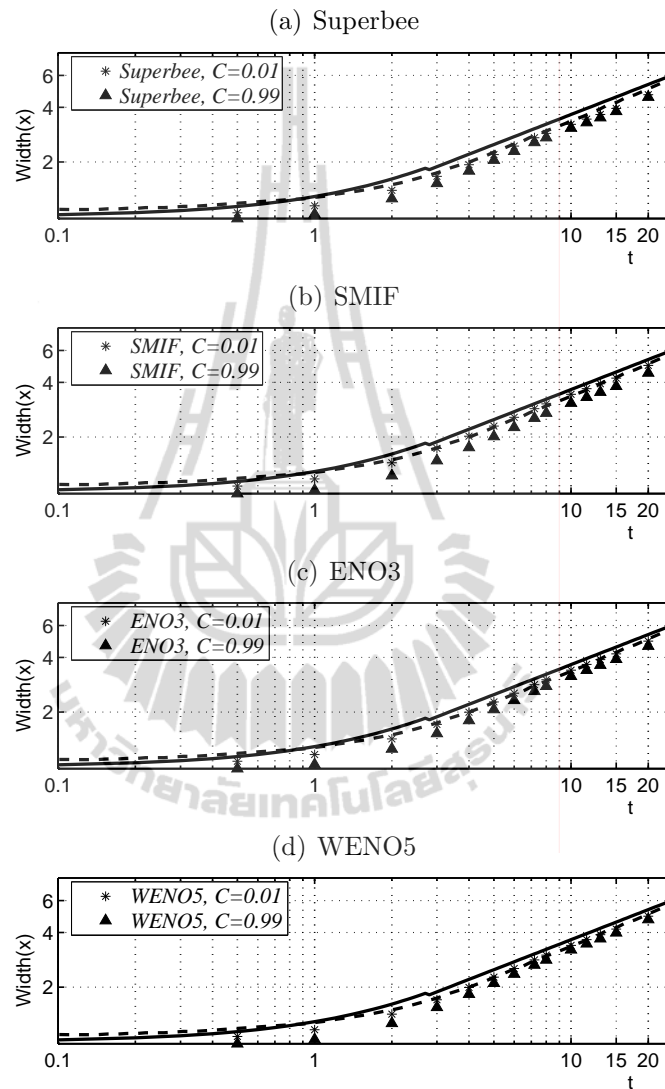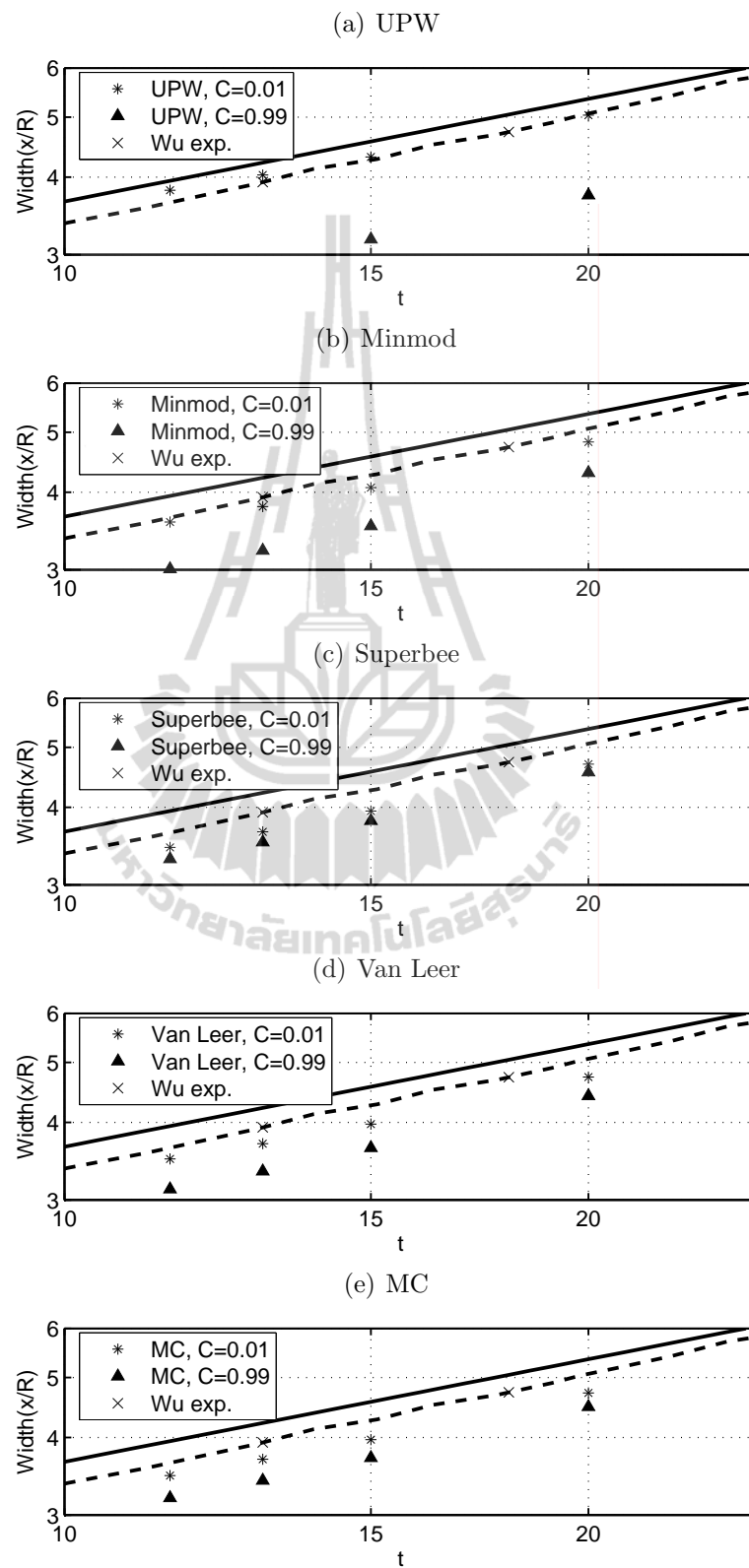
(a) UPW

(b) Minmod

(c) Superbee

(d) Van Leer

(e) MC

Figure 4.9 The same as Figure 4.7, zoomed pictures.

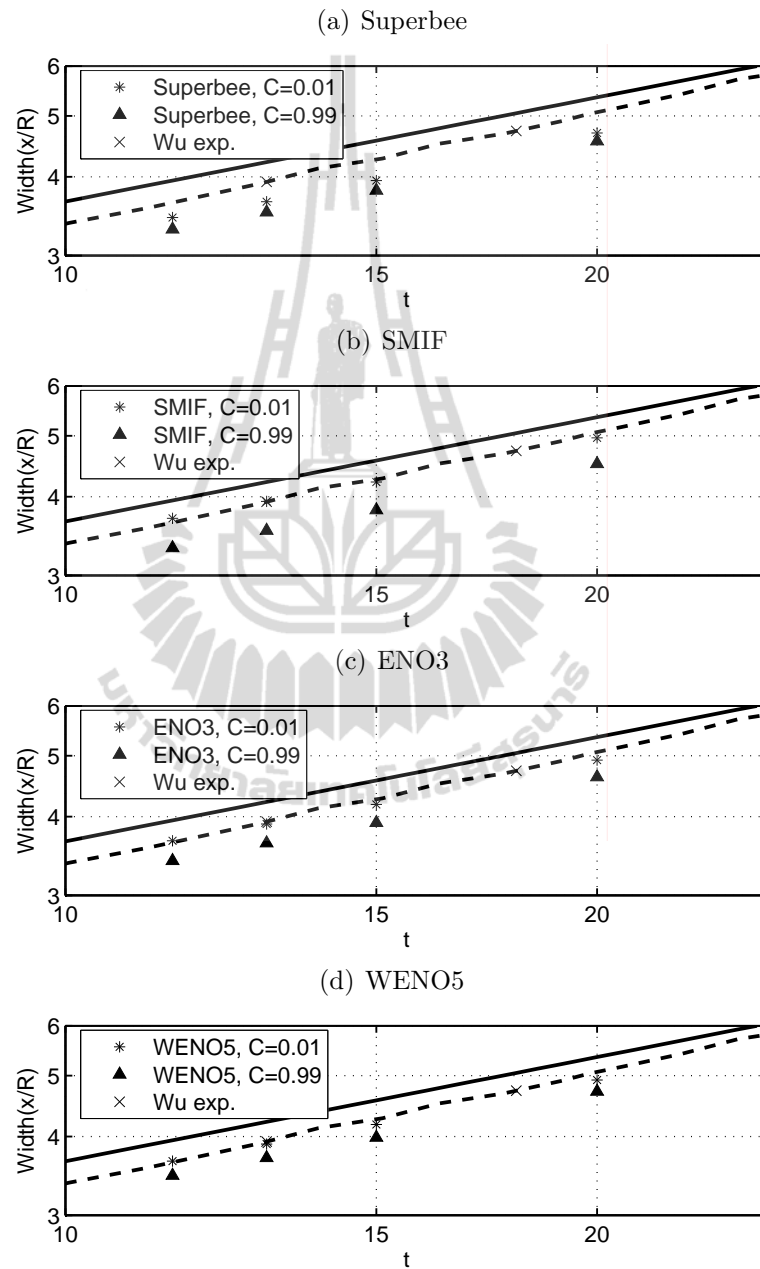(a) Superbee

(b) SMIF

(c) ENO3

(d) WENO5

Figure 4.10   The same as Figure 4.8, zoomed pictures.

Table 4.2 Locations of $x^{\blacktriangle}$ and x^{*} of all schemes.

Times: t	Grids spacings	UPW		F-L/Mindmod		F-L/Superbee		F-L/Van Lee		F-L/MC		SMIF		ENO3		WENO5	
		$x^{\blacktriangle}$	x^{*}	$x^{\blacktriangle}$	x^{*}	$x^{\blacktriangle}$	x^{*}	$x^{\blacktriangle}$	x^{*}	$x^{\blacktriangle}$	x^{*}	$x^{\blacktriangle}$	x^{*}	$x^{\blacktriangle}$	x^{*}	$x^{\blacktriangle}$	x^{*}
1	0.1	0.903	1.321	0.904	1.277	0.906	1.196	0.905	1.235	0.905	1.198	0.905	1.272	0.904	1.255	0.904	1.253
	0.05	0.955	1.264	0.901	1.216	0.975	1.150	0.976	1.191	0.972	1.185	0.964	1.209	0.973	1.196	0.975	1.195
	0.025	0.994	1.220	1.013	1.179	1.031	1.147	1.027	1.157	1.030	1.481	1.018	1.175	1.028	1.168	1.030	1.165
2	0.1	0.932	1.670	1.006	1.570	1.046	1.486	1.024	1.496	1.037	1.490	1.016	1.555	1.058	1.498	1.071	1.498
	0.05	1.056	1.584	1.122	1.495	1.180	1.417	1.157	1.447	1.171	1.441	1.144	1.489	1.181	1.486	1.193	1.450
	0.025	1.137	1.520	1.205	1.449	1.257	1.395	1.231	1.417	1.251	1.400	1.224	1.444	1.253	1.423	1.265	1.421
4	0.1	1.208	2.334	1.400	2.171	1.516	1.996	1.458	2.085	1.508	2.066	1.445	2.149	1.510	2.073	1.574	2.075
	0.05	1.415	2.222	1.568	2.084	1.698	1.957	1.628	2.013	1.672	1.994	1.637	2.073	1.705	2.034	1.742	2.032
	0.025	1.548	2.135	1.680	2.021	1.788	1.933	1.728	1.970	1.762	1.950	1.752	2.021	1.799	1.996	1.829	1.993
8	0.1	0.990	3.470	1.144	3.185	2.326	2.944	2.218	3.050	2.313	2.990	1.115	3.182	1.773	3.063	2.526	3.060
	0.05	1.883	3.310	2.330	3.080	2.603	2.900	2.440	2.978	2.532	2.946	2.547	3.098	2.638	3.043	2.717	3.043
	0.025	2.271	3.182	2.505	2.998	2.728	2.875	2.593	2.922	2.653	2.911	2.710	3.044	2.777	3.012	2.829	3.006
10	0.1	0.990	3.892	1.374	3.566	2.616	3.285	2.257	3.387	2.555	3.337	1.305	3.586	0.155	3.443	2.906	3.442
	0.05	1.871	3.718	2.592	3.442	2.938	3.247	2.727	3.325	2.842	3.294	2.885	3.498	3.001	3.439	3.103	3.439
	0.025	2.517	3.568	2.804	3.355	3.076	3.224	2.910	3.270	2.980	3.254	3.080	3.441	3.156	3.405	3.215	3.400
15	0.1	0.990	4.686	0.990	4.292	3.344	3.967	0.489	4.080	3.242	3.998	0.990	4.386	0.990	4.198	2.362	4.212
	0.05	0.613	4.487	3.308	4.158	3.688	3.948	3.455	4.023	3.568	3.994	3.564	4.287	3.674	4.213	3.869	4.222
	0.025	3.176	4.312	3.529	4.071	3.805	3.995	3.640	3.975	3.710	3.969	3.810	4.223	3.912	4.184	3.987	4.180
20	0.1	0.990	5.288	0.990	4.990	0.575	4.688	0.281	4.787	0.446	4.744	0.990	5.075	0.990	4.914	0.990	4.895
	0.05	0.159	5.173	4.022	4.903	4.453	4.699	4.230	4.773	4.357	4.475	4.229	5.015	4.087	4.942	4.589	4.950
	0.025	3.742	5.036	4.300	4.823	4.558	4.698	4.415	4.734	4.485	4.721	4.511	4.963	4.625	4.920	4.718	4.920
25	0.1	0.990	5.739	0.990	5.543	0.632	5.197	0.990	5.312	0.396	5.276	0.990	5.662	0.990	5.489	0.990	5.454
	0.05	0.990	5.731	0.522	5.520	4.953	5.278	4.501	5.347	4.732	5.328	2.312	5.671	1.209	5.593	5.108	5.598
	0.025	3.724	5.644	4.756	5.424	5.101	5.248	4.920	5.302	5.007	5.291	5.039	5.631	5.179	5.579	5.326	5.579

Table 4.2 shows the values at x^* and $x^{\blacktriangle}$ for grid refinement study at different instants of time. The convergence rate of the flux-limiter scheme is a little less than 2nd-order. The convergence rate of SMIF, ENO3 and WENO5 is a little better than 2nd-order. This result is in agreement with comments by Zhang et al. (2010) that the ENO and WENO schemes are only 2nd-order accurate for general nonlinear systems, regardless of the order of accuracy in the one-dimensional reconstruction procedure. It is clear from Table 4.2 that a grid spacing $\Delta x = \Delta z = 0.1$ is too coarse to be used to estimate the width of the mixed region. Numerical diffusion spreads the discontinuity by too large an amount.

The motion of the passive Lagrangian particle is also computed during the simulation. The typical goal of Lagrangian particle tracking is to gain information on the motion of the fluid. The tracer particles behave like true fluid elements. The tracking algorithm is described in Appendix B. Initially, particles are distributed uniformly within the mixed region. The initial location of each particle is given as follows,

$$x_i^{(0)^2} + z_j^{(0)^2} \le 1,$$

$$x_i^{(0)} = (i-1)\delta x, \ i = 1, 2, ..., N_x,$$

$$z_j^{(0)} = (j-1)\delta z, \ j = 1, 2, ..., N_z,$$

where $x_i^{(0)}, z_j^{(0)}$ are the x and z coordinates of the particle at the initial time. Typically, about 10,000 particles are used in the computation.

Figures 4.11-4.13 show distribution of passive Lagrangian particles at times $t = 4$, 15 and 20 for the case of $Re = 10^3$. Computations were performed on a grid 400×160 with grid spacings $\Delta x = \Delta z = 0.025$ and $\Delta t = 0.0005$. The number of total particles is 8,050 particles in the mixed region at the initial instant, i.e. $\delta x = \delta z = 0.01$. Subfigures (a)-(h) correspond to computations with different

approximation of convective terms in the equations. As can seen from Figure 4.11, at time $t = 4$ there is no significant difference in the distribution of the Lagrangian particles. The flux-limiter schemes demonstrate a higher proportion of particles near axis $x = 0$. This effect probably related to realization condition of symmetry on this axis. All schemes considered indicate an appearance of an elevated head of the spreading front.

Figure 4.11 shows the position of Lagrangian particles at $t = 4$ by all schemes. There was 8,050 Lagrangian particles initially located in the mixed region. The Reynolds number was 10^3, and the spatial grid was 400×160 nodes with $\Delta x = \Delta z = 0.025$ were used in computation with time increment $\Delta t = 0.0005$. Comparing the performance of SMIF, ENO3 and WENO5 (Figures 4.11 (f),(g),(h), respectively) almost identical results are seen. The flux-limiter with Superbee limiter gives a little bit smaller width of the mixed region and different locations of the Lagrangian particles near $x = 0$ axis.

Figure 4.12 shows Lagrangian particle distributions corresponding to time $t = 15$. All schemes demonstrate a wave shape of the edge of the mixed region. The first-order upwind scheme (Figure 4.12 (a)) demonstrates a smoother shape of the mixed region. The width of the mixed region corresponds to the largest horizontal coordinate of a Lagrangian particle. The first-order upwind scheme and upwind scheme with the flux-limiter indicate smaller widths compared with the width defined for cases with SMIF, ENO3 and WENO5 approximations of convective terms.

Figure 4.13 shows Lagrangian particle distributions at time $t = 20$. The width of mixed region in the case of first-order upwind scheme has the smallest value compared with the other schemes. SMIF, ENO3 and WENO5 schemes reproduce an identical shape of the mixed region.
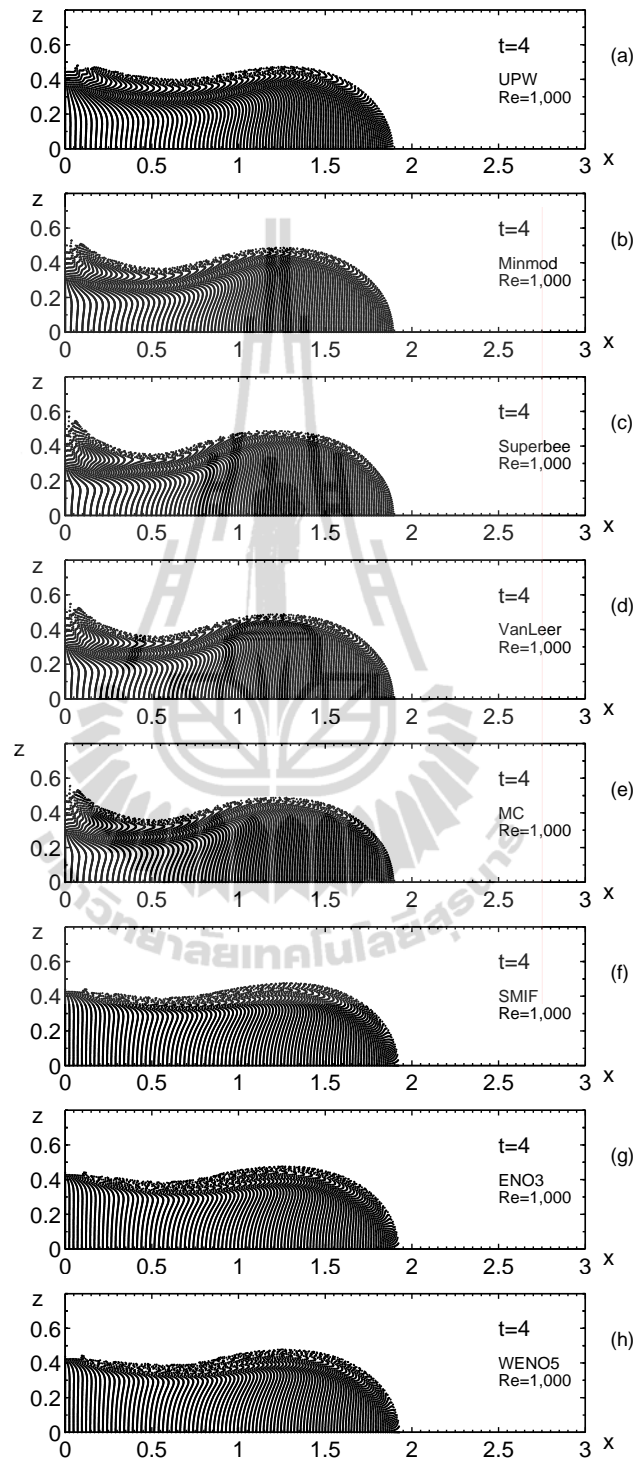
Figure 4.11 Shapes of the collapsed mixed region at $t = 4$. Comparison of 1st−order UPW, four flux-limiter, SMIF, ENO3 and WENO5 schemes with $Re = 10^3$, $\Delta x = \Delta z = 0.025$ and $\Delta t = 0.0005$.
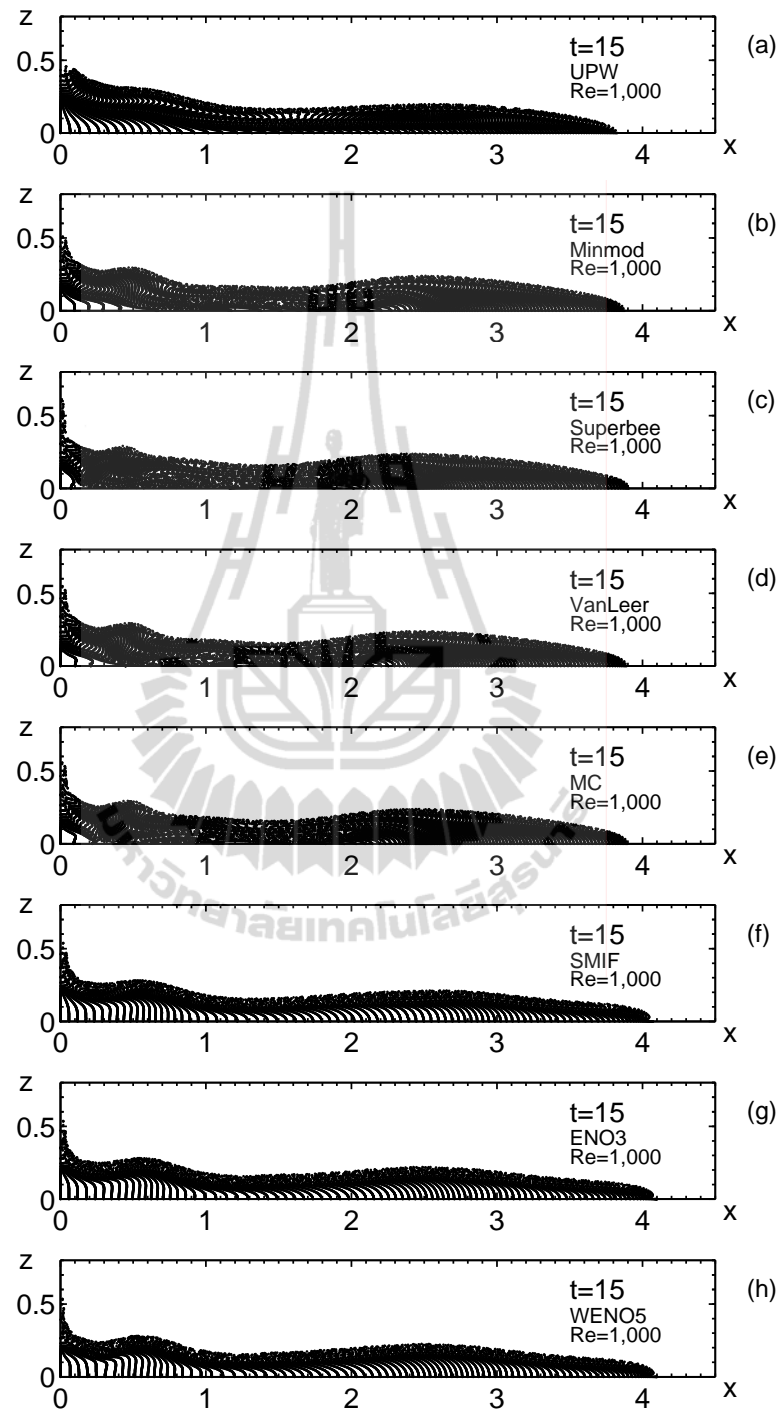
Figure 4.12 Shapes of the collapsed mixed region at $t = 15$. Comparison of $1^{st}-$order UPW, four flux-limiter, SMIF, ENO3 and WENO5 schemes with $Re= 10^3$, $\Delta x = \Delta z = 0.025$ and $\Delta t = 0.0005$.
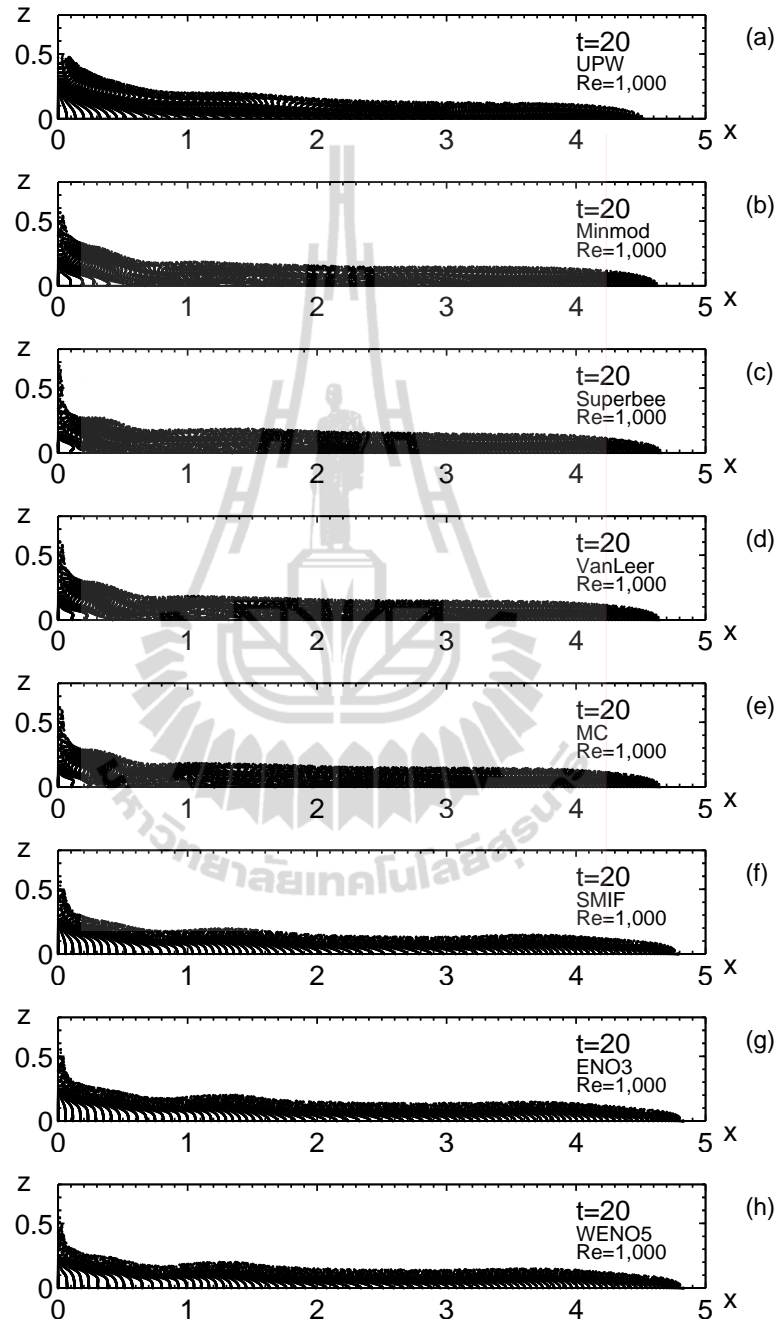
Figure 4.13 Shapes of the collapsed mixed region at $t = 20$. Comparison of 1st−order UPW, four flux-limiter, SMIF, ENO3 and WENO5 schemes with $Re=10^3$, $\Delta x = \Delta z = 0.025$ and $\Delta t = 0.0005$.

The "typical" sequential shape of the mixed region is illustrated in Figure 4.14 in terms of distribution of Lagrangian particles at selected time instants. The region collapses rather suddenly in the initial stage ($t \leq 2$). Gradually, an elevated head starts to form at the spreading front (see Figure 4.14 (c)). The elevated head then causes a subsequent collapse: flattening first the elevated part, and then developing a small wedge in front of the region proper ($t \geq 10$) (see Figures 4.14 (e) - (h)). The scenario described above qualitatively corresponds to one represented by Wu (1969). The observation of a sharp boundary of the mixed region in all numerical simulations on a fine grid demonstrates that no appreciable additional mixing takes place.

Figures 4.15 - 4.18 show Lagrangian particle distributions and contours of the passive scalar at different time instants for the case of $Re = 5 \times 10^4$. Computations were performed on the grid 360×160 with $\Delta x = \Delta z = 0.05$. The time step was $\Delta t = 0.001$. There were 8,050 particles in the mixed region at the initial instant. The shaded domain represents the shape of the mixed region defined by the Lagrangian particles. To make this region transparent we have not drawn all the particles. Solid lines in Figures 4.15 - 4.18 show the evolution of the curve $C(t, x, z) = const$. Lines with letter "a" represent level $C(t, x, z) = 0.01$, lines with letter "b" represent level $C(t, x, z) = 0.5$ and lines with letter "c" represent $C(t, x, z) = 0.99$. In Figure 4.15, we compare the results of five schemes; first order upwind and four schemes with flux limiters given by equation (3.26) at time $t = 4$.

It can be seen that the Superbee limiter scheme has the smallest dispersion of the passive scalar. If the shape of the mixed region is defined by the contour line $C(t, x, z) = const.$ then the contour level $C(t, x, z) = 0.5$ coincides with the shape of a mixed region defined by Lagrangian particles. Contour lines $C(t, x, z) = 0.01$ define a large domain of the mixed region compared with the shape by Lagrangian
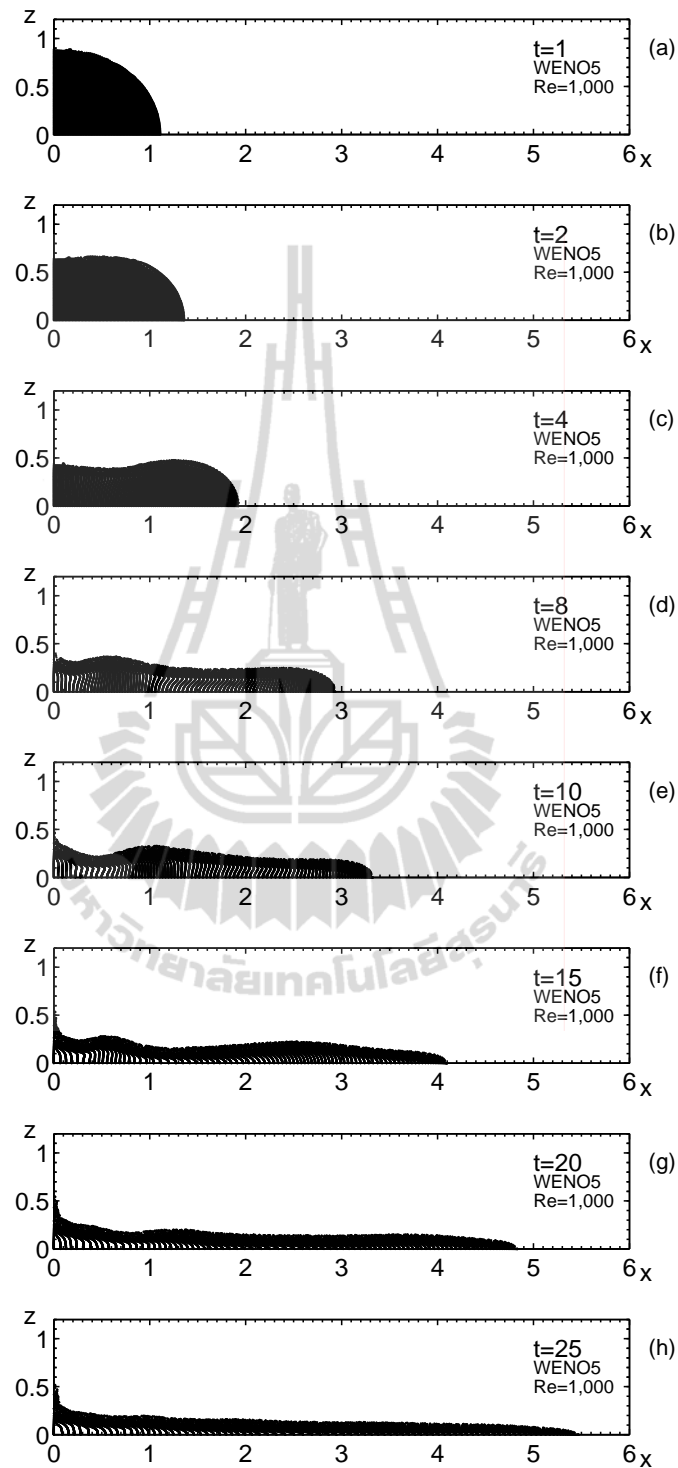
Figure 4.14 Shapes of the collapsed mixed region results of WENO5 scheme. The horizontal coordinate corresponds to the distance from the center. The pictures show Lagrangian particles located in the mixed region (8,050 particles), $Re = 10^3$, $\Delta x = \Delta z = 0.025$, $\Delta t = 0.0005$ and computational domain:$[0, 10] \times [0, 4]$.

particle. Contour lines, $C(t, x, z) = 0.99$, are located inside the shadow region for every time instant presented in Figures 4.15 - 4.18. Cross signs ($\times$) on the $x-$axis correspond to Wu's experiments. It can be seen that contour lines $C(t, x, z) = 0.01$ define the width of the mixed region corresponding to the experimental data. The width of the mixed region defined by a tracer particle for all schemes are smaller than the experimental results of Wu.

In Figure 4.16, we compare the results of four schemes, namely the scheme with Superbee flux-limiter, two adaptive stencil schemes (SMIF and ENO3), and a weighted stencil scheme (WENO5) at time $t = 4$. Performance of the adaptive stencil schemes and weighted stencil scheme are almost identical. We can see that the curve $C(t, x, z) = 0.5$ coincides with the edge of the shadowed region. The scheme with Superbee limiter demonstrates a smaller value of the mixed region width compared with SMIF, ENO3 and WENO5.

Figure 4.17 shows results of comparison of four schemes (Superbee, SMIF, ENO3 and WENO5) at the time instant $t = 10$. The qualitative behavior is similar to previous case corresponding to $t = 4$. Curve $C(t, x, z) = 0.5$ corresponds to the edge of the shadowed domain. The width of the mixed region defined by Lagrangian particles is smaller than Wu's experimental results.

Figure 4.18 shows results of computation corresponding to time instant $t = 20$. The four approximations of convective terms are compared, namely, flux-limiter Superbee, SMIF, ENO3 and WENO5. Again, the contour curve $C(t, x, z) = 0.5$ coincides with the boundary of the shadowed domain. The width of the mixed region defined by Lagrangian particles is smaller compared to Wu's experiments.

The ENO3 and WENO5 schemes define a width of the mixed region closer to Wu's experimental results. Comparison of results for $Re = 10^3$ and $Re = 5 \times 10^4$ demonstrate a weak dependence on the Reynolds number. It was pointed out

by Wu (1969) that the collapse during the initial ($t \approx 3$) and principal stage ($3 < t < 25$) is primarily a gravitational flow phenomenon, and that the collapse process during these stage is identical for different Reynolds numbers. Note that in case of $Re = 10^3$ the computational domain was $10R \times 4R$ in x and z directions, respectively. In case of $Re = 5 \times 10^4$ the computation domain was approximately twice larger, $18R \times 8R$, in the x and z direction, respectively. This note demonstrates that the size of computational domain $10R \times 4R$ is sufficient to shift boundary conditions from infinitely on to the boundary of the computation domain.
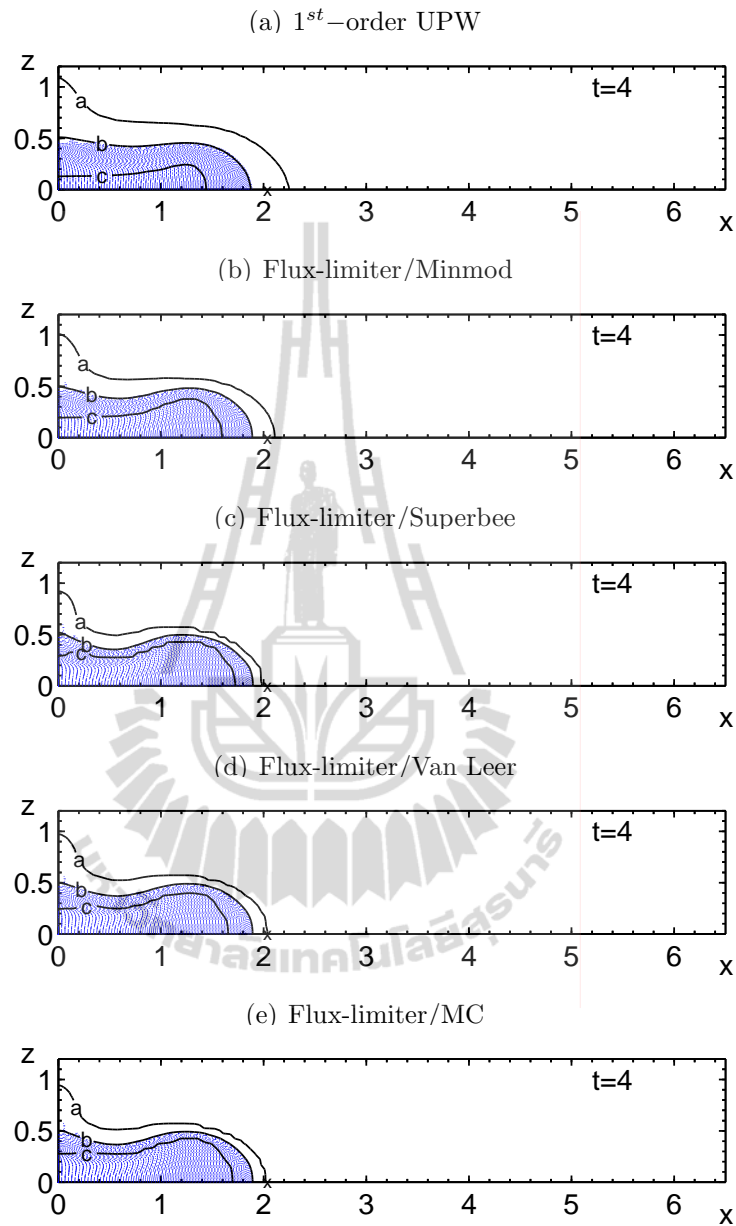
(a) $1^{st}-$order UPW

(b) Flux-limiter/Minmod

(c) Flux-limiter/Superbee

(d) Flux-limiter/Van Leer
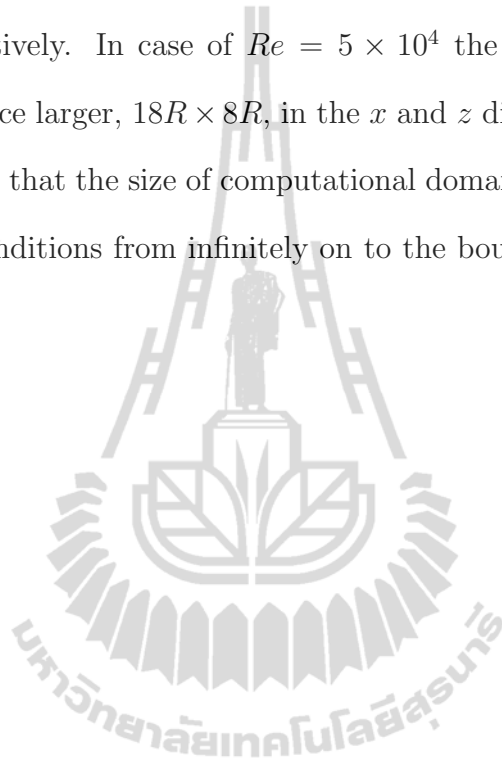
(e) Flux-limiter/MC

Figure 4.15 Shapes of the collapsed mixed region at time $t = 4$ of $1^{st}-$order UPW and four flux-limiter comparing to Wu's formula($\times$-mark on x axis), solid lines represent contour lines from numerical results of passive scalar, shaded areas represent mixed region taken from Lagrangian particles. $Re = 5 \times 10^4, \Delta x = \Delta z = 0.05$ and $\Delta t = 0.001$. The letters a, b and c represent passive scalar contour lines: $C(t, x, z) = 0.01, 0.5$ and 0.99, respectively.
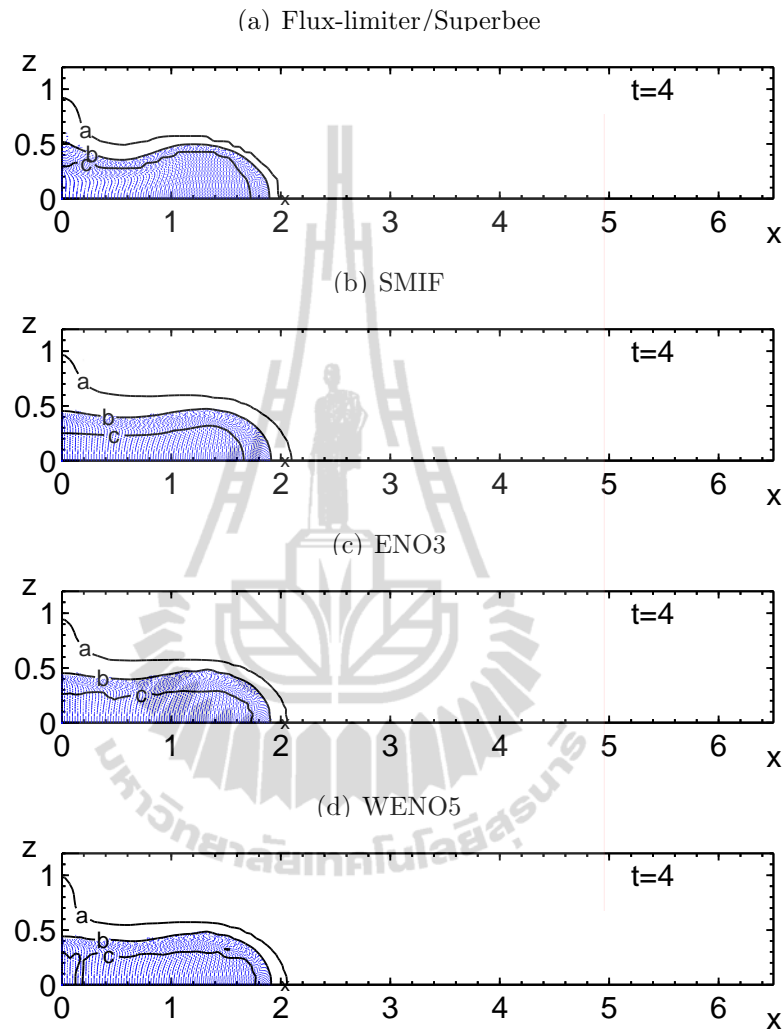
Figure 4.16 Shapes of the collapsed mixed region at time $t = 4$ of Superbee, SMIF, ENO3 and WENO5 comparing to Wu's formula($\times$-mark on x axis), solid lines represent contours line from numerical results of passive scalar, shaded areas represent mixed region taken from Lagrangian particles. $Re = 5 \times 10^4, \Delta x = \Delta z = 0.05$ and $\Delta t = 0.001$. The letters a, b and c represent passive scalar contour lines: $C(t, x, z) = 0.01, 0.5$ and 0.99, respectively.
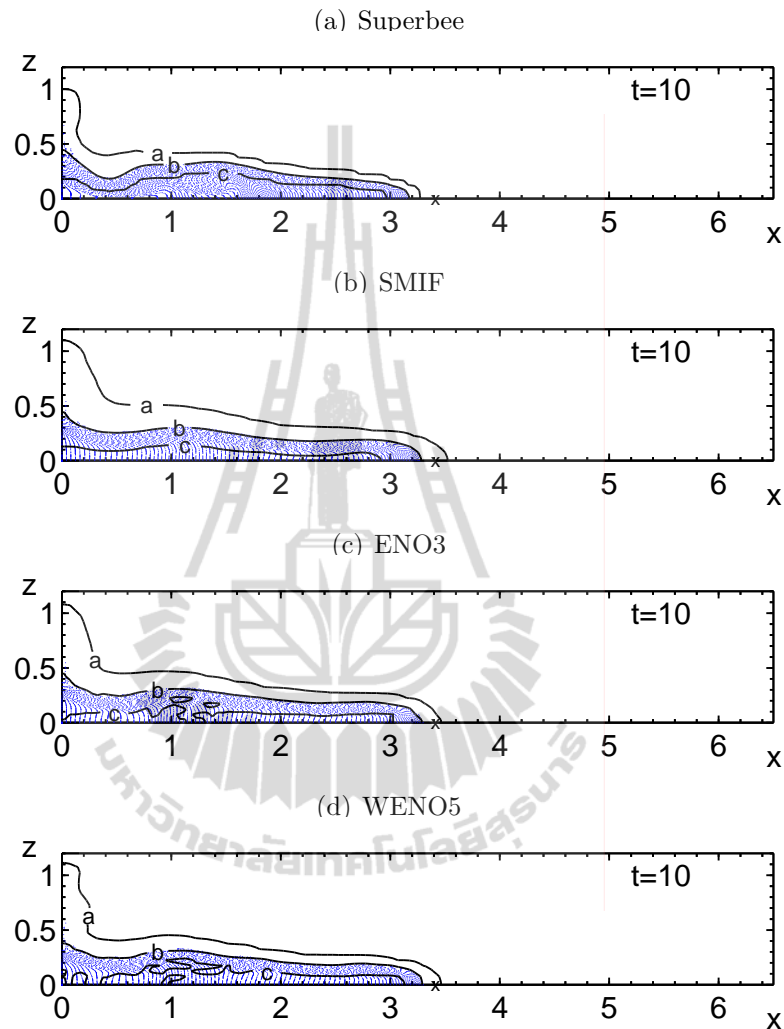
Figure 4.17 Shapes of the collapsed mixed region at time $t = 10$ of Flux-limiter/Superbee, SMIF, ENO3 and WENO5 comparing to Wu's formula($\times$-mark on x axis), solid lines represent contour lines from numerical results of passive scalar, shaded areas represent mixed region taken from Lagrangian particles. $Re = 5 \times 10^4$, $\Delta x = \Delta z = 0.05$ and $\Delta t = 0.001$. The letters a, b and c represent passive scalar contour lines: $C(t, x, z) = 0.01, 0.5$ and 0.99, respectively.
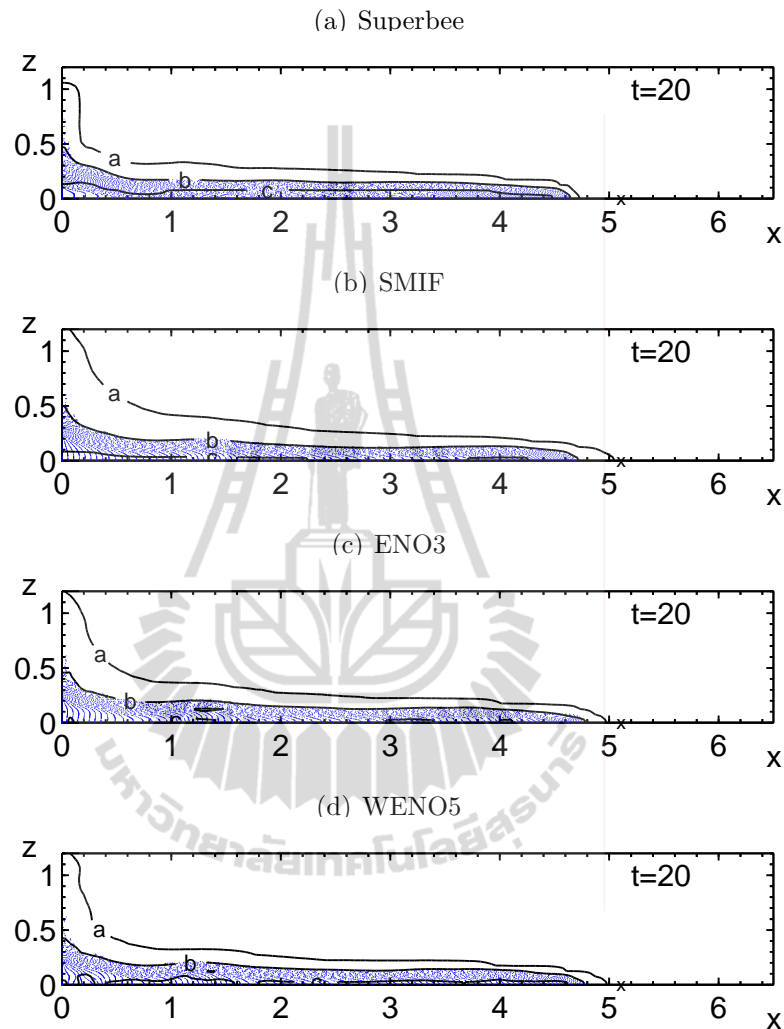
(a) Superbee

(b) SMIF

(c) ENO3

(d) WENO5

Figure 4.18 Shapes of the collapsed mixed region at time $t = 20$ of Flux-limiter/Superbee, SMIF, ENO3 and WENO5 comparing to Wu's formula($\times$-mark on x axis), solid lines represent contour lines from numerical results of passive scalar, shaded areas represent mixed region taken from Lagrangian particles. $Re = 5 \times 10^4$, $\Delta x = \Delta z = 0.05$, and $\Delta t = 0.001$. The letters a, b and c represent passive scalar contour lines: $C(t, x, z) = 0.01, 0.5$ and 0.99, respectively.

4.2 Internal wave generated by collapsing region

Everyone has experienced surface waves; when the surface of the water is displaced upward, gravity pulls it back downward, the fluid develops a vertical velocity (potential energy turns into kinetic energy) and because of inertia, the surface penetrates below its level of equilibrium. An oscillation results. The same mechanism is at work whenever two fluid densities differ. But the existence of such interfacial waves is not restricted to fluids with two distinct densities and a single interface. At the limit of a continuously stratified fluid the mechanism remains the same. There is a continuous interplay between gravity and inertia and a continuous exchange between potential and kinetic energy.

The phenomenon of internal wave generated by the turbulent wake of a self-propelled body moving through a density-stratified fluid was first demonstrated by Schooley and Stewart (1963). The later experiments of Wu (1969) represent the generation of an internal wave generated by the collapse of mixed region in the stratified fluid.

The results presented in this section correspond to $Re = 5 \times 10^4$, which is the same as in Wu's experiment. The total computational domain size, compared to the radius of the initial mixed region, is 18 radii wide and 8 radii high. We used a uniform mesh with grid spacings $\Delta x = \Delta z = 0.05$. Figure 4.19 shows constant density lines at successive time instants. Figure 4.19 shows in detail the collapse of the original mixed region and the growth and propagation of internal waves. During the initial collapse of the mixed region, $t \leq 4$, the fluid layers near the axis $x = 0$ displace towards the center and reach their maximum deflection at the end of the initial collapse stage. As the deflected layers oscillate back toward their equilibrium positions, undulations of the isopycnic lines are observed.
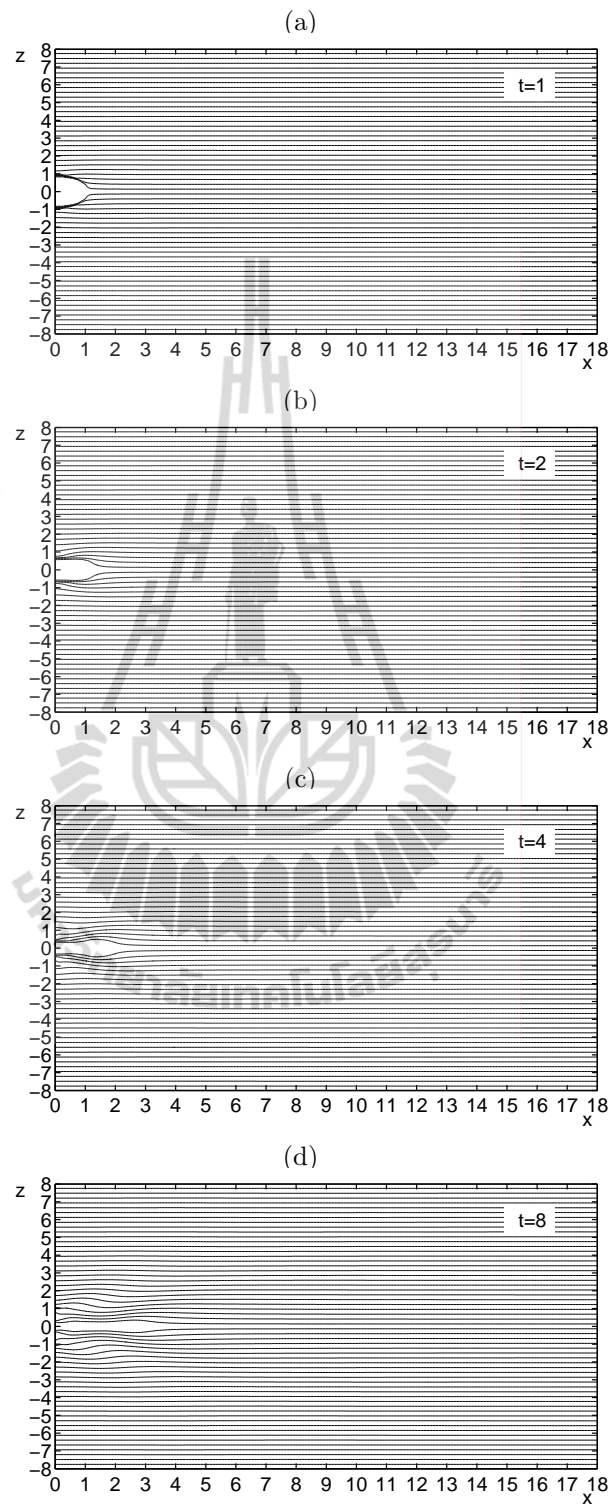
Figure 4.19 The constant density lines, $\rho(t, x, z) = const$, at successive time intervals. Results from SMIF approximation of convective terms are presented for $Re = 5 \times 10^4$, $\Delta x = \Delta z = 0.05$, $\Delta t = 0.001$ and computational domain=18×8.
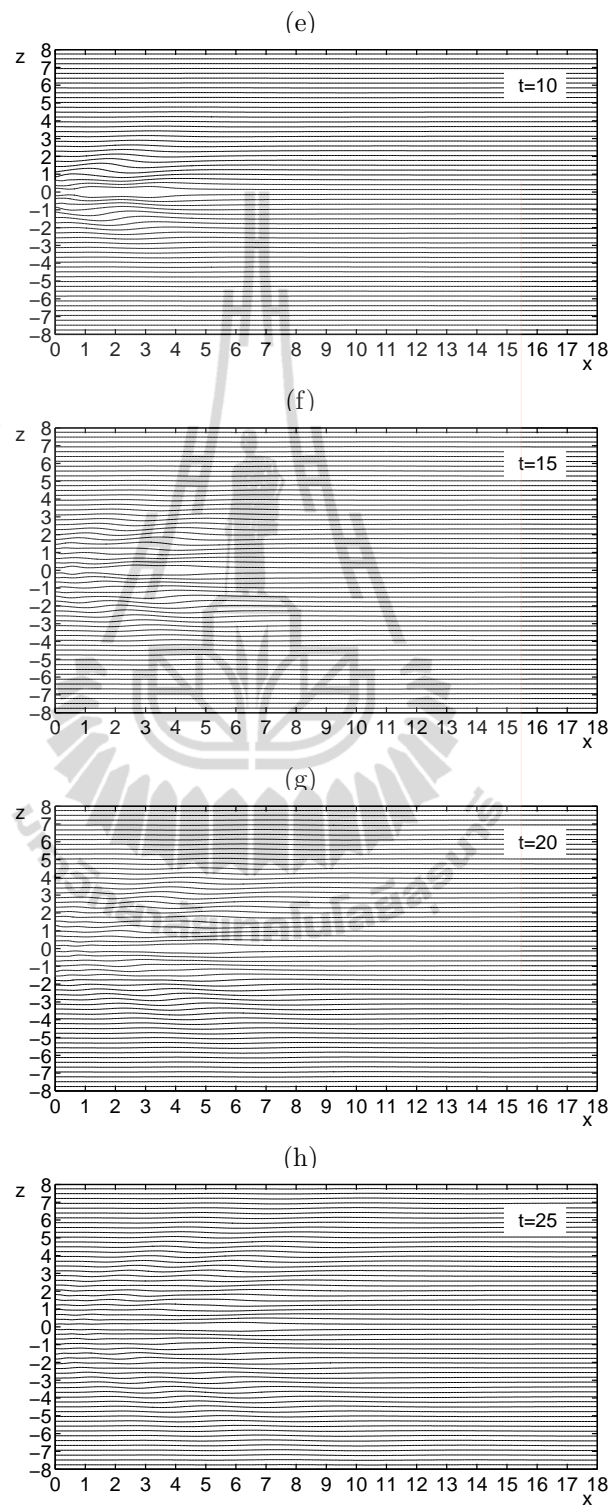
(e)

(f)

(g)

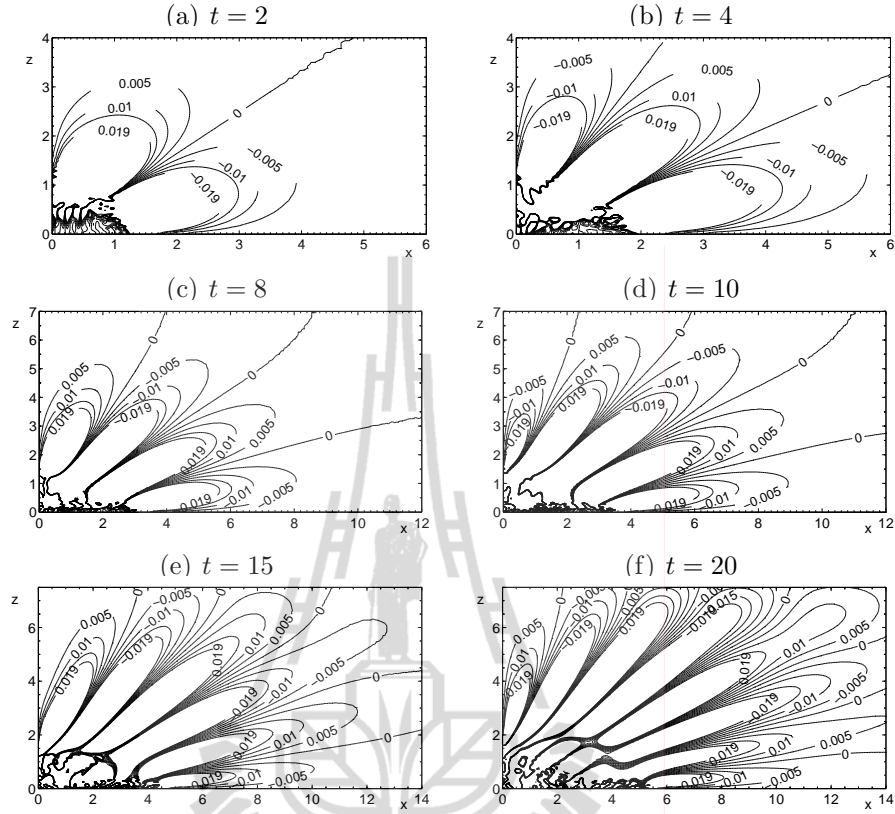(h)

Figure 4.19   Continued.

Figure 4.20 Isolines $\partial\rho_1/\partial x = const$. Computational results from WENO5 approximation of convective terms with $Re= 5 \times 10^4$, $\Delta x = \Delta z = 0.05$ and $\Delta t = 0.001$.

In order to better understand the wave generated by a collapsing region, the phase pattern of internal waves is illustrated by Figure 4.20, where isolines $\partial\rho_1/\partial x = const$ are drawn at time instants $t = 2$, 4, 8, 10, 15 and 20. Lines $\partial\rho_1/\partial x = 0$ correspond to peaks and troughs of internal waves. Not far from the center, except the small region where the finite size of mixed region is dominant, these lines are almost straight. This agrees with the experimental data of Wu (1969). However, for large distance from center, the lines $\partial\rho_1/\partial x = 0$ change to a curve. This behavior of phase lines $\partial\rho_1/\partial x = 0$ does not relate to the method of approximation of convective terms. Other approximations of convective terms were used in this work to demonstrate similar effects.

Plots concerning the wave heights are shown in Figures 4.21-4.24. The maximum wave heights are as large as two-tenths of the initial radius of the mixed region, however while the waves propagate from the collapse center, all undulations continuously and rather rapidly reduce their heights. To illustrate a dependence of the internal wave on different approximations of the convective terms, we present in Figures 4.21-4.22 and Figures 4.23-4.24, the isolines $\rho = const$ obtained at $t = 4$ and 10, respectively, using numerical simulations with different high-order upwind approximations of convective terms in the governing equations. Isolines $\rho = \rho_s(z^*) = const$ are drawn for $z^* = 0.5$, 1.0, 2.0 and 3.0. Figures 4.21 and 4.23 compare the influence of the first-order upwind and four flux-limiter approximations of convective terms. Figures 4.22 and 4.24 compare the performance of the flux-limiter with Superbee, the SMIF, the ENO3 and the WENO5 approximations of convective terms in the governing equations. At time $t = 4$, the first-order monotone approximation demonstrates the smaller size of the troughs of the line $\rho = \rho_s(0.5) = const$. An essential difference in wave patterns $\rho = \rho_s(0.5) = const$ corresponding to the flux-limiter with Superbee, the SMIF, the ENO3 and the WENO5 approximations of convective terms can be seen. Wave patterns $\rho = \rho_s(z^*)$, $z^* = 1.0$, 2.0, 3.0 corresponding to different approximations of convective terms are nearly identical as seen from data of Figures 4.21-4.24.
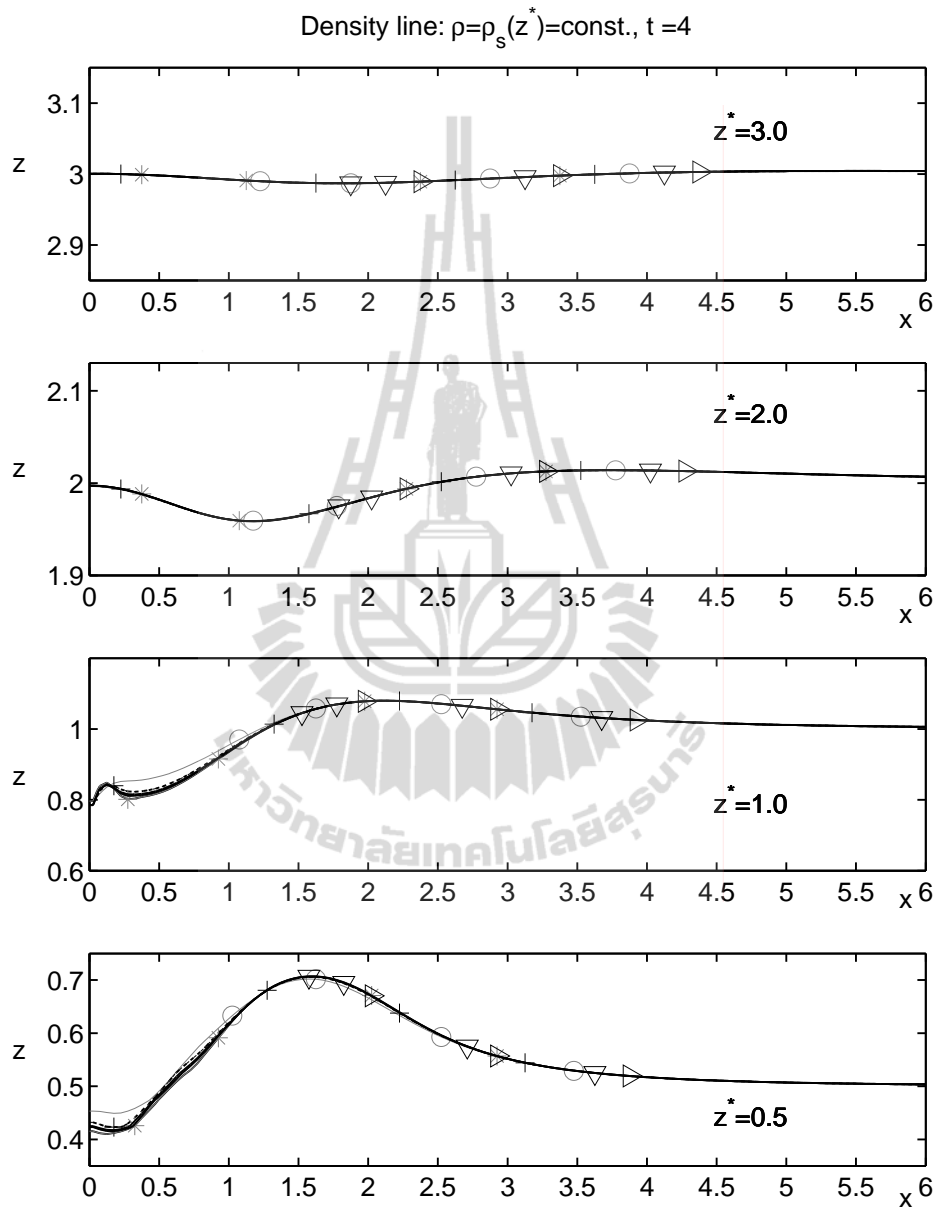
Figure 4.21 Isolines $\rho = \rho(z^*)$, $z^* = 0.5$, 1.0, 2.0, and 3.0 at $t = 4$. Corresponds to 1st−order UPW and four flux-limiters $\circ$ – 1st-order upwind; $\triangleright$ –Minmod; $*$ –Superbee; $\triangledown$ – Van Leer; $+$ – MC. Grid spacings: $\Delta x = \Delta z = 0.05$ and $Re = 5 \times 10^4$.
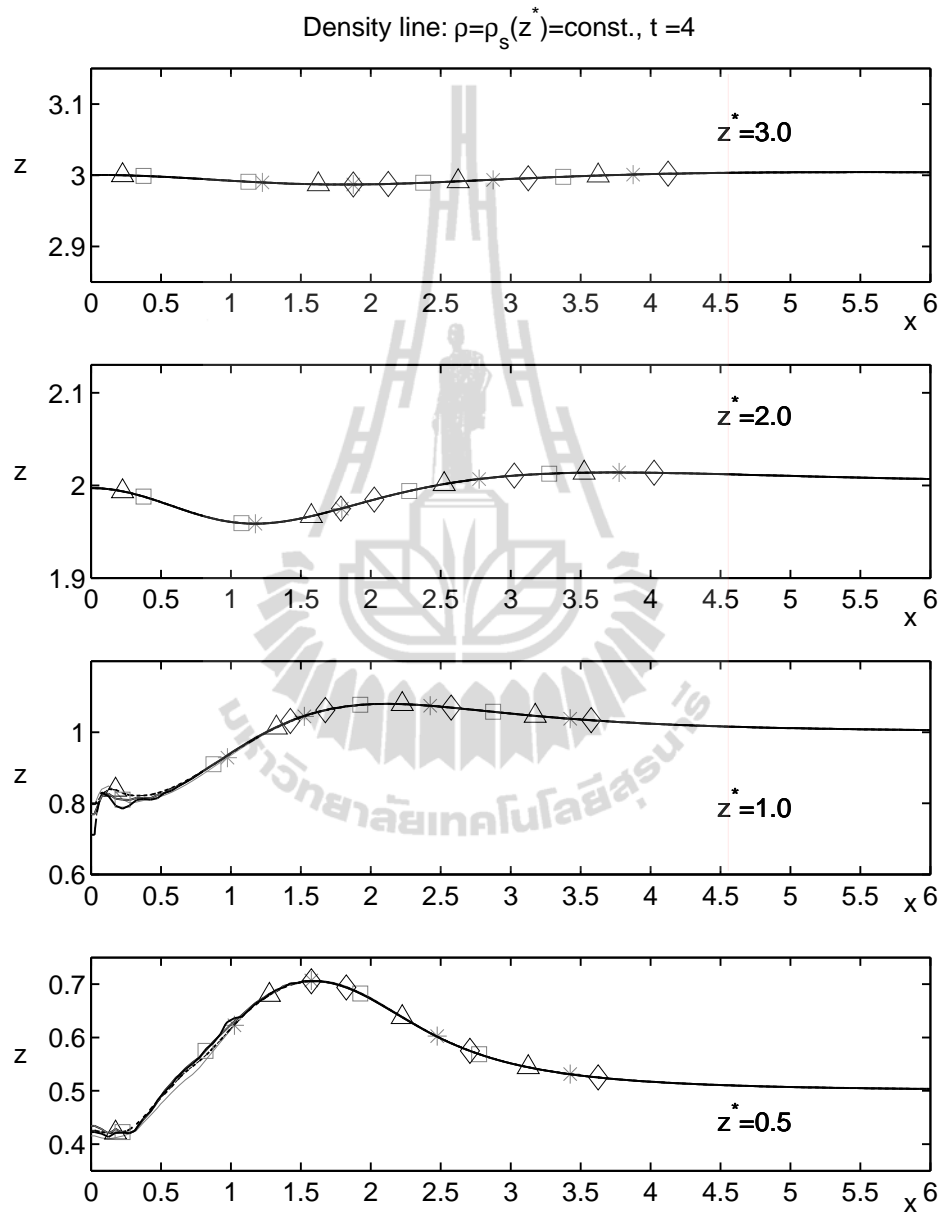
Figure 4.22 Isolines $\rho = \rho(z^*)$, $z^* = 0.5,\ 1.0,\ 2.0,\ $ and 3.0 at $t = 4$. Corresponds to four schemes: $*$ – flux-limiter/Superbee; $\triangle$ – SMIF; $\square$ – ENO3; $\diamond$ – WENO5. Grid spacings: $\Delta x = \Delta z = 0.05$ and $Re = 5 \times 10^4$.

Figure 4.23 Isolines $\rho = \rho_s(z^*)$, $z^* = 0.5$, 1.0, 2.0, and 3.0 at $t = 10$. Corresponds to five flux-limiters $\circ$ – 1st-order upwind; $\triangleright$ –Minmod; $*$ –Superbee; ∇ – Van Leer; $+$ – MC. Grid spacings: $\Delta x = \Delta z = 0.05$ and $Re = 5 \times 10^4$.

Figure 4.24 Isolines $\rho = \rho_s(z^*)$, $z^* = 0.5$, 1.0, 2.0, and 3.0 at $t = 10$. Corresponds to four schemes: $*$ – flux-limiter/Superbee; $\triangle$ – SMIF; $\square$ – ENO3; $\diamond$ – WENO5. Grid spacings: $\Delta x = \Delta z = 0.05$ and $Re = 5 \times 10^4$.
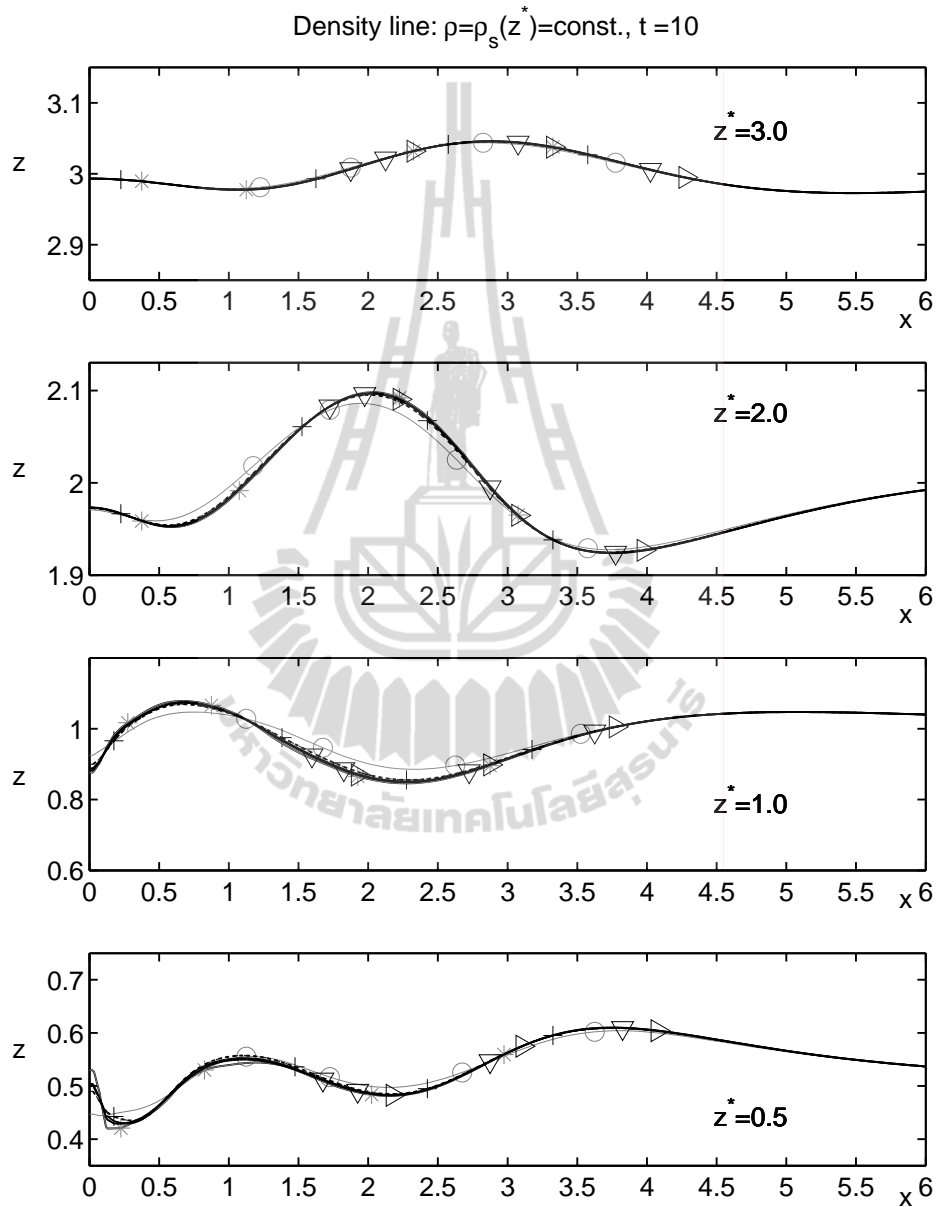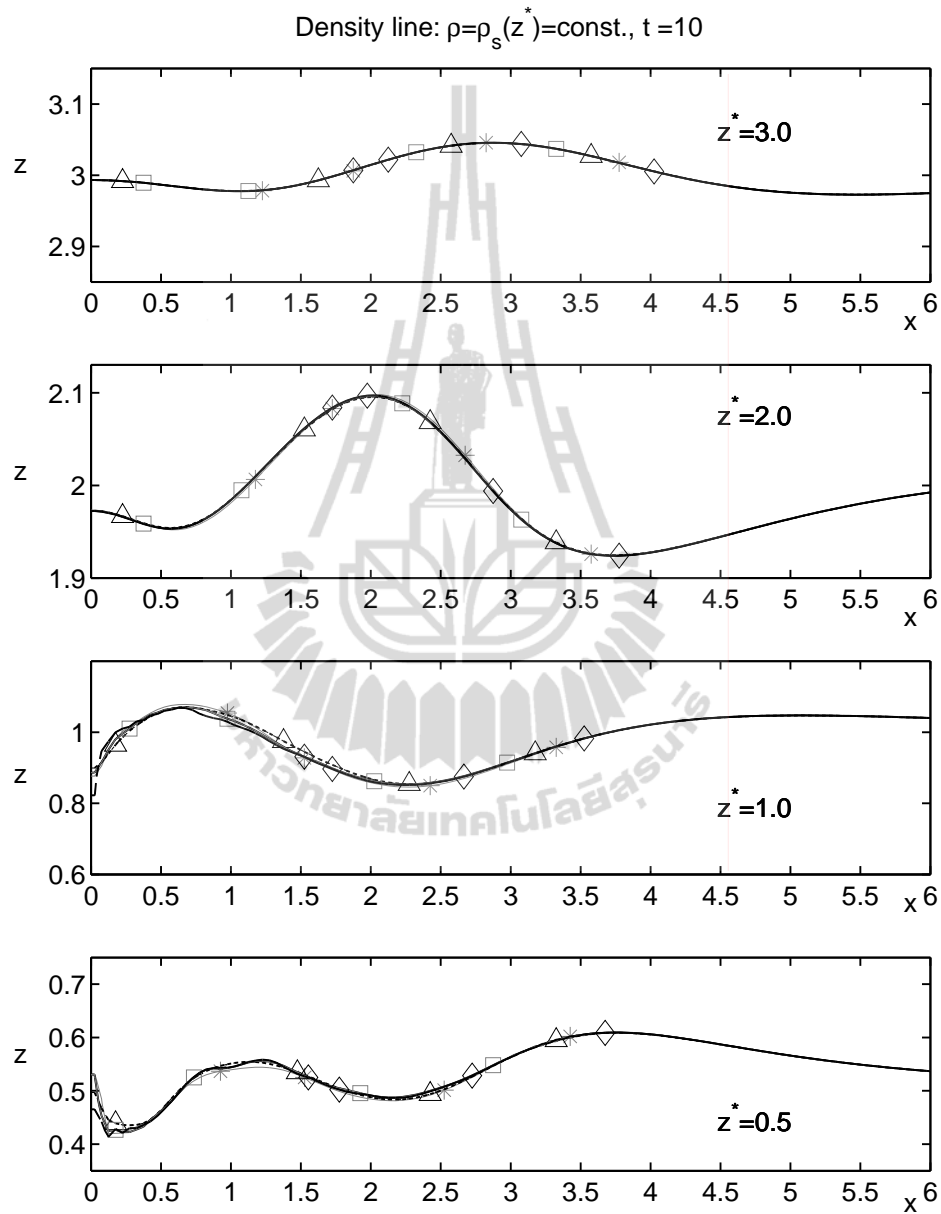
CHAPTER V

CONCLUSIONS AND FUTURE WORKS

Numerical simulations of the collapse of a fully mixed region in a linearly stratified fluid were considered. The simulations are based on the incompressible Navier-Stokes equations in the Oberbeck-Boussinesq approximation. Several high-order upwind finite difference schemes have been successfully tested and compared for this problem. The comparative study has shown that among four flux-limiter schemes (Minmod, Superbee, Van Leer and MC limiters), the Superbee limiter gives better results with regards to the value of the numerical diffusion. The Superbee flux-limiter gives the smallest numerical diffusion when compared with the SMIF, the ENO3 and the WENO5 schemes. The performances of the ENO3 and the SMIF are nearly identical. The WENO5 scheme produces smaller smearing of discontinuities compared with the SMIF and the ENO3 schemes. The Superbee flux-limiter gives a little bit smaller width of the mixed region compared with Wu's experimental data. The WENO5 scheme demonstrates results closer to Wu's experimental data. More significant influence of different high-order upwind approximations on the patterns of internal waves generated by the collapsed of mixed region are observed for the waves with density level corresponding to the density of unperturbed fluid on the levels of mixed region.

The following reconsideration can be given for future research based on the current thesis.

1. Developed computer codes can be used to simulate the collapse of the mixed

region with a density perturbation of Gaussian form. The performance of different approximations of convective terms will probably not be essential.

2. The case of a non-linear stratification (especially narrow pycnocline) has to be very sensitive to the choice on upwind approximation.

3. The interaction of two or more mixing regions in the stratified fluid can be analyzed by the developed approaches.

4. In natural circumstances, the disturbances rarely evolve as purely two-dimensional. Thus, some peculiar features may arise which are absent in the plain two-dimensional case.
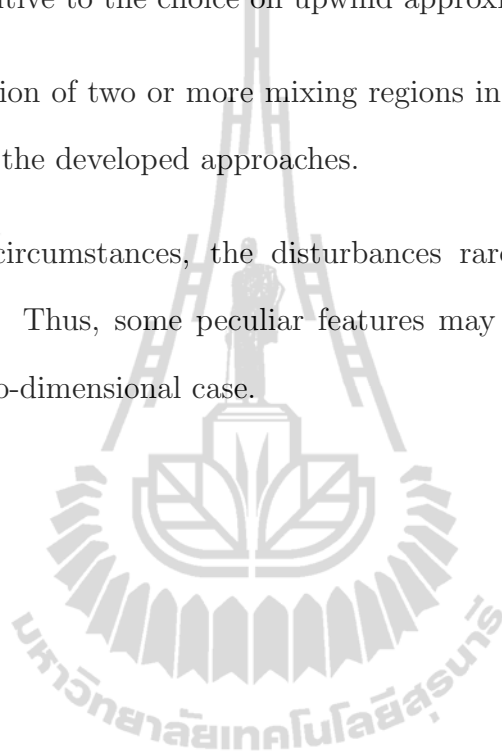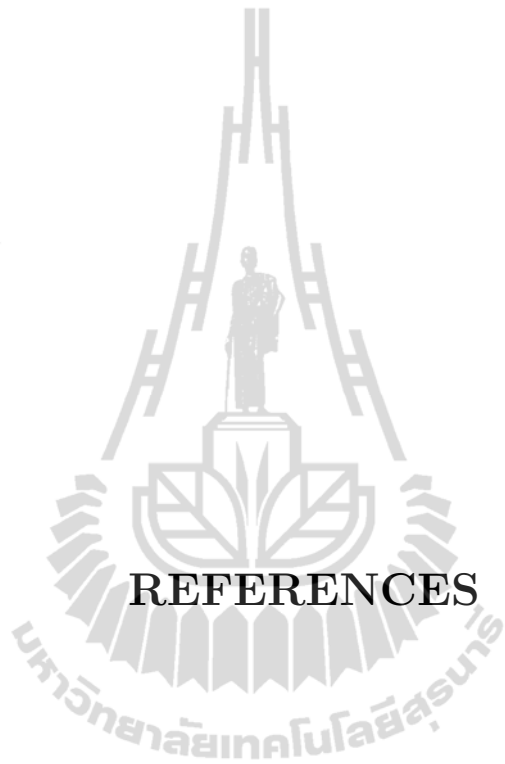
REFERENCES

REFERENCES

Amsden, A.A., and Harlow, F.H. (1970). The SMAC method: a numerical technique for calculating incompressible fluid flows. **Los Alamos Scientific Laboratory Report LA-4370** 10: 357–390.

Babakov, A.V. (1983). Application of flow theory to a problem of the dynamics of a viscous stratified fluid. **USSR Computational Mathematics and Mathematical Physics** 23(2): 115–119.

Balsara, D., and Shu, C.W. (2000). Monotonicity preserving weighted essentially non-oscillatory schemes with increasingly high order of accuracy. **Journal of Computational Physics** 160(2): 405–452.

Belotserkovskii, O.M. (1997). **Mathematical Modelling in Informatics: Numerical Simulation in the Mechanics of Continuous Media.** Moscow State University of Printing Arts, Moscow Russia.

Boris, J.P., and Book, D.L. (1976). Flux-corrected transport. III. minimal-error FCT algorithms. **Journal of Computational Physics** 20(4): 397–431.

Brown, D., Cortez, R., and Minion, M. (2001). Accurate projection methods for the incompressible Navier-Stokes equations. **Journal of Computational Physics** 168: 464–499.

Chorin, A.J. (1968). Numerical solution of the Navier-Stokes equations. **Mathematics of Computation** 22(104): 745–762.

Chung, T.J. (2002). **Computational Fluid Dynamics**. Cambridge University Press.

Fedorov, K.N. (1976). **Fine Thermohaline Structure of Oceanic Water**. Gidrometeoizdat, Leningrad, 183 pages (in Russian).

Fortin, M., Peyret, R., and Temam, R. (1971). Résolution numérique des équations de Navier-Stokes pour un fluide incompressible. **Journal de Mécanique** 10: 357–390.

Gilreath, H.E., and Brandt, A. (1985). Experiments on the generation of internal waves in a stratified fluid. **AIAA Journal** 23: 693–700.

Gushchin, V.A. (1981). The splitting method for problems of the dynamics of an inhomogeneous viscous incompressible fluid. **USSR Computational Mathematics and Mathematical Physics** 21(4): 190–204.

Gushchin, V.A., and Konshin, V.N. (1992). Computational aspects of the splitting method for incompressible flow with a free surface. **Journal of Computeres and Fluids** 21-3: 345–353.

Gushchin, V.A., and Matyushin, P.V. (1997). Numerical simulation of separated flow past a sphere. **Computational Mathematics and Mathematical Physics** 37-9: 1086–1100.

Harten, A., Engquist, B., Osher, S., and Chakravarthy, S. (1987). Uniformly high order essentially non-oscillatory schemes. **Journal of Computational Physics** 71: 231–303.

Hirsch, C. (1991). **Numerical Computational of Internal and External Flows, Vol. 2: Computational Methods for Inviscid and Viscous Flows**. John Wiley and Sons.

Jiang, G.S., and Shu, C.W. (1996). Efficient implementation of weighted ENO schemes. **Journal of Computational Physics** 126: 202–228.

Kim, J., and Moin, P. (1985). Application of a fractional-step method to incompressible Navier-Stokes equations. **Journal of Computational Physics** 59: 308–323.

LeVeque, R.J. (1996). High-resolution conservative algorithms for advection in incompressible flow. **SIAM Journal on Numerical Analysis** 33: 627–665.

Lighthill, J.M. (2002). **Waves in Fluids**. Cambridge University Press, England, 2nd edition, 520 pages.

Lytkin, Y.M., and Chernykh, G.G. (1975). On internal waves induced by the mixing zone collapse in a stratified fluid. **Mathematical Problems of Mechanics (Continuum Dynamics)** 22: 116–132, Institute of Hydrodynamics, Sib. Branch USSR Akad. Sci., Novosibirsk.

Maderich, V.S., Nikishov, V.I., and Stetsenko, A.G. (1988). **Internal Mixing Dynamics in a Stratified Medium**. Naukova Dumka, Kiev, (in Russian).

Monin, A.S., and Ozmidov, R.V. (1981). **Oceanic Turbulence**. Gidrometeoizdat, Leningrad, (in Russian).

Moshkin, N.P., Chernykh, G.G., and Fomina, A.V. (2005). On the influence of small total momentum imbalance on turbulent wake dynamics in the linearly stratified medium. **Mathematical Modeling** 17(1): 19–33.

Munroe, J.R., Voegel, C., Sutherland, B.R., Birman, V., and Meiburg, E.H. (2009). Intrusive gravity currents from finite-length locks in a uniformly stratified fluid. **Journal of Fluid Mechanics** 635: 245–273.

Nartov, V.P., and Chernykh, G.G. (1982). On numerical modeling of fluid flow generated by collapse of mixed region in stratified medium. Technical report, Institute of Theoretical and Applied Mechanics, Novosibirsk, preprint (in Russian).

Roe, P.L. (1983). Some contributions to the modeling of discontinuous flows. **Lecture Notes in Applied Mathematics** 22: 163–193.

Roe, P.L., and Sidilkover, D. (1992). Optimum positive linear schemes for advection in two and three dimensions. **SIAM Journal on Numerical Analysis** 29: 1542–1568.

Schooley, A.H., and Stewart, R.W. (1963). Experiments with a self-propelled body in a fluid with a vertical density gradient. **Journal of Fluid Mechanics** 15: 83–96.

Shu, C.W. (1997). Essentially non-oscillatory and weighted essentially non-oscillatory schemes for hyperbolic conservation laws. **NASA/CR-97, ICASE Report** 97.

Temam, R. (1969). Sur l'approximation de la solution des équations de Navier-Stokes par la méthode des pas fractionnaires II. **Archive for Rational Mechanics and Analysis** 33: 377–385.

Turner, J.S. (1973). **Buoyancy Effects in Fluids**. Cambridge University Press, Cambridge, 368 pages.

Van-Leer, B. (1974). Towards the ULTIMATE conservation difference scheme. II. Monotonicity and conservation combined in a second order scheme. **Journal of Computational Physics** 14: 361–370.

Van-Leer, B. (1977). Towards the ULTIMATE conservation difference scheme. IV. A new approach to numerical convection. **Journal of Computational Physics** 23: 276–299.

Voropaeva, O.F., and Chernykh, G.G. (1998). Internal waves generated by momentumless turbulent wake in a linearly stratified fluid. **Mathematical Modeling** 10(6): 75–89.

Voropaeva, O.F., Moshkin, N.P., and Chernykh, G.G. (2003). Internal waves generated by turbulent wakes in a stably stratified medium. **Doklady Physics** 48(9): 517–521.

Vorozhtsov, E.V., and Yanenko, N.N. (1989). **Methods for the Localization of Singularities in Numerical Solutions of Gas Dynamics Problems**. Springer-Verlag, New York.

Wessel, W.R. (1969). Numerical study of the collapse of a perturbation in an infinite density stratified fluid. **Physics of Fluids** 12(12): 170–176.

Wu, J. (1969). Mixed region collapse with internal wave generation in a density-stratified medium. **Journal of Fluid Mechanics** 35: 531–544.

Yanenko, N.N. (1971). **The Method of Fractional Steps**. Springer-Verlag, New York, USA, 160 pages.

Zhang, R., Zhang, M., and Shu, C.W. (2010). On the order of accuracy and

numerical performance of two classes of finite volume WENO schemes. **Communications on Computational Physics** 17: 807–827.
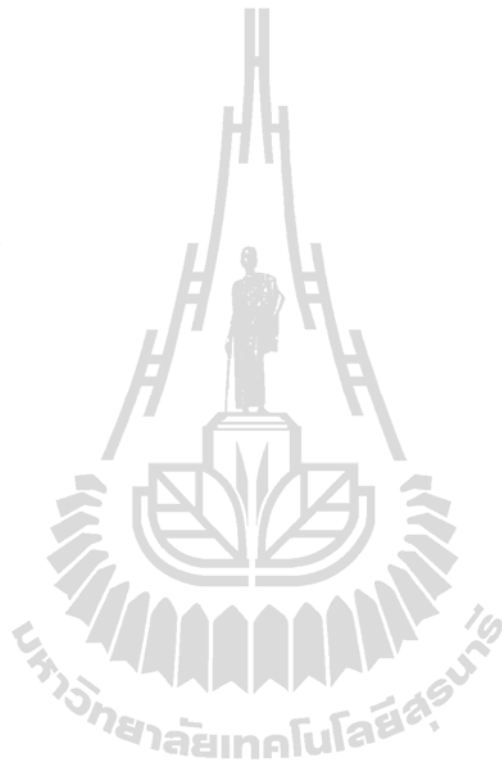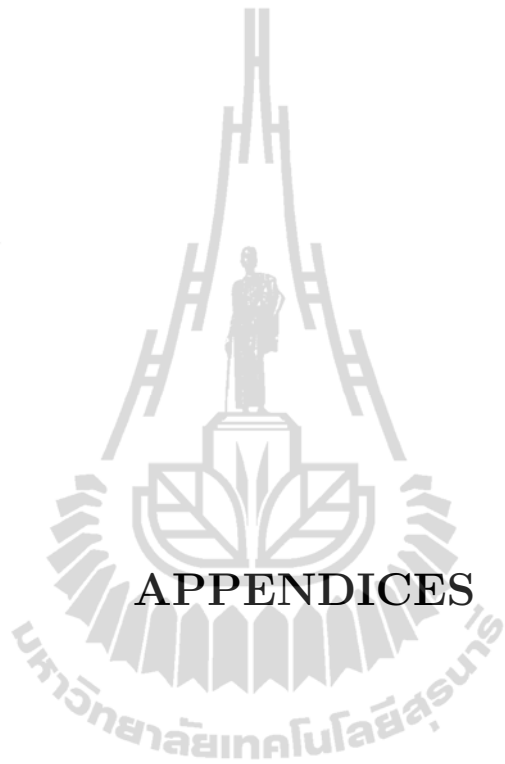
APPENDICES

APPENDIX A

SOLUTION OF POISSON'S EQUATION

In this section, we shall discuss a numerical technique for solving Poisson's equation

$$\Delta\phi + q = 0, \tag{A.1}$$

where $\phi = \phi(x, z)$ is a real value function on a 2D domain denoted by $\Omega \subset \mathbb{R}^2$, and $\Delta = \dfrac{\partial^2}{\partial x^2} + \dfrac{\partial^2}{\partial z^2}$ is the Laplace operator. The source function $q = q(x, z)$ is given on domain Ω. A solution $\phi(x, z)$ satisfying (A.1) will also satisfy boundary conditions on the boundary $\partial\Omega$. Here, we consider the Neumann boundary condition

$$\frac{\partial\phi}{\partial n} = 0 \quad \text{on} \quad \partial\Omega. \tag{A.2}$$

To solve the Poisson equation, we consider a problem which is an unsteady problem

$$\frac{\partial\phi}{\partial t} = \Delta\phi + q, \tag{A.3}$$

with the same steady boundary condition. The relation between steady and unsteady problems is that the solution of the unsteady problem approaches the solution of the steady problem with the same boundary conditions as $t \to \infty$, see for more details in "*The Method of Fractional Steps*" by Yanenko (1971).

The splitting scheme (known as fractional steps) for unsteady problem (A.3):

$$\frac{\phi^{n+1/2} - \phi^n}{\tau} = \Lambda_1(\alpha\phi^{n+1/2} + \beta\phi^n) + q_1, \tag{A.4}$$

$$\frac{\phi^{n+1} - \phi^{n+1/2}}{\tau} = \Lambda_2(\alpha\phi^{n+1} + \beta\phi^{n+1/2}) + q_2, \tag{A.5}$$

where α, β are weight parameters with $\alpha + \beta = 1$, $\tau = \Delta t$, and

$$\Lambda_1 = \frac{\partial^2}{\partial x^2}, \quad \Lambda_2 = \frac{\partial^2}{\partial z^2} \tag{A.6}$$

We notice that the right hand terms q_1 and q_2 are still undetermined. The scheme in the whole steps of (A.4) and (A.5) is

$$(1 - \alpha\tau\Lambda_1)(1 - \alpha\tau\Lambda_2)\phi^{n+1} = (1 + \beta\tau\Lambda_1)(1 + \beta\tau\Lambda_2)\phi^n + \tau Q, \tag{A.7}$$

where

$$Q = (1 + \beta\tau\Lambda_2)q_1 + (1 - \alpha\tau\Lambda_1)q_2. \tag{A.8}$$

It is necessary that $Q = q$. Assuming that $q_1 = 0$ we then have

$$(1 - \alpha\tau\Lambda_1)q_2 = q. \tag{A.9}$$

The next algorithm solves Poisson's equation through unsteady problem (A.3).

Algorithm 3: assume $q_1 = 0$,

- Step 1. solve for $\phi^{n+1/2}$

$$\frac{\phi^{n+1/2} - \phi^n}{\tau} = \Lambda_1(\alpha\phi^{n+1/2} + \beta\phi^n). \tag{A.10}$$

- Step 2. solve for q_2:

$$(1 - \alpha\tau\Lambda_1)q_2 = q. \tag{A.11}$$

- Step 3. solve for ϕ^{n+1}:

$$\frac{\phi^{n+1} - \phi^{n+1/2}}{\tau} = \Lambda_2(\alpha\phi^{n+1} + \beta\phi^{n+1/2}) + q_2. \tag{A.12}$$

- Step 4. stop criteria:

$$\| \phi^{n+1} - \phi^n \| < \varepsilon, \tag{A.13}$$

where ϵ is a small number and we used $\varepsilon = 10^{-7}$ in this work.
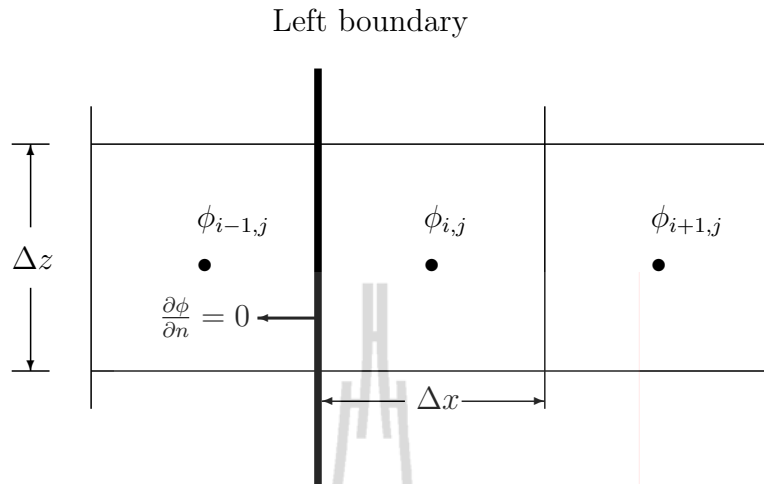
Left boundary

Figure A.1 The cell $I_{i,j}$ adjacent to the left boundary.

Remarks:

1. The Neumann boundary condition must be subjected to the discretization for the points involving to the boundaries.

2. We use the central difference formula to approximate differential operators Λ_1 and Λ_2. Thus, all algebraic systems in Steps 1, 2 and 3 become tridiagonal systems.

3. The tridiagonal systems may be solved by any method, i.e. the Thomas algorithm which is very effective and easy to handle.

4. Example of discretization of $\Lambda_1\phi_{i,j}$ for the cell $I_{i,j}$ as in Figure A.1,

$$
\begin{aligned}
\Lambda_1\phi_{i,j} &= \frac{\partial^2\phi_{i,j}}{\partial x^2}, \\
&\approx \frac{\phi_{i-1,j} - 2\phi_{i,j} + \phi_{i+1,j}}{\Delta x^2}, \\
&\approx \frac{-\phi_{i,j} + \phi_{i+1,j}}{\Delta x^2}.
\end{aligned} \tag{A.14}
$$

The approximation (A.14) is obtained from applying the Neumann condition (A.2) to the left boundary.

APPENDIX B

LAGRANGIAN PARTICLE TRACKING

In this section, we describe the method of Lagrangian particle tracking in rectangular domain Ω. Let the mixing region $R \subset \Omega$ be a quarter of a unit circle with center at the origin as in Figure B.1. To study the evaluation of the mixing region, we track the Lagrangian particles inside the mixing region at every single time step. The location of each particle is given initially. After the velocity field is computed, we update the particle locations. Assume that we are observing a particle P with initial location at $P^0(x_{P^0}, z_{P^0})$. Figure B.2 depicts the particle P moving from P^n to P^{n+1}. At time T_n, the location of $P^n(x_{P^n}, z_{P^n})$ is contained in a rectangular cell $C = [x_1, x_2] \times [z_1, z_2] \subset \Omega$ which has vertices at grid points numbered $1, 2, 3$ and 4 as in Figure B.2. The particle P^n moves to P^{n+1} with velocities (u_P^{n+1}, v_P^{n+1}). The particle's velocities can be interpolated using velocity information of grid points $1, 2, 3$ and 4. In this work, we use the interpolation with weight functions $\Phi_i(\xi, \eta)$, where $i = 1, 2, 3, 4$ correspond to the cell C's vertices. The local point (ξ, η) in Figure B.3 represents the point transformation of global point (x, z) in the cell C and is given by the following transformation

$$\xi = \frac{x - x_c}{\Delta x/2}, \quad \eta = \frac{z - z_c}{\Delta z/2}, \tag{B.1}$$

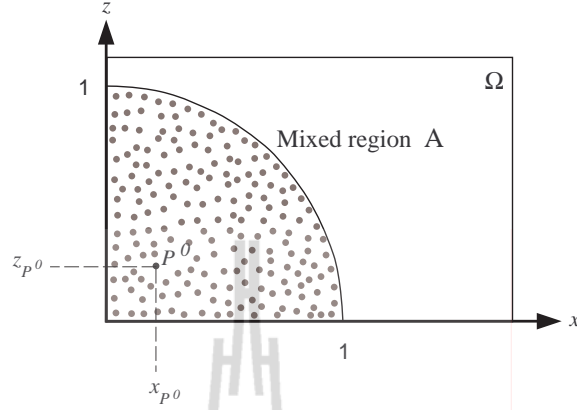where $x_c = (x_1 + x_2)/2, \quad z_c = (z_1 + z_2)/2$ be a cell C's midpoint.

Figure B.1 Lagrangian particles at initial time.

The four weight functions of the local point (ξ, η) can be computed by formulas:

$$\begin{aligned}
\Phi_1(\xi, \eta) &= \frac{1}{4}(1 - \xi)(1 - \eta), \\
\Phi_2(\xi, \eta) &= \frac{1}{4}(1 + \xi)(1 - \eta), \\
\Phi_3(\xi, \eta) &= \frac{1}{4}(1 + \xi)(1 + \eta), \\
\Phi_4(\xi, \eta) &= \frac{1}{4}(1 - \xi)(1 + \eta).
\end{aligned} \tag{B.2}$$

The interpolation of the velocities (u_P^{n+1}, v_P^{n+1}) using the four weights of local point (ξ_P, η_P) are

$$u_P^{n+1} = \sum_{i=1}^{4} u_i^{n+1} \Phi_i(\xi_P, \eta_P), \tag{B.3}$$

$$v_P^{n+1} = \sum_{i=1}^{4} v_i^{n+1} \Phi_i(\xi_P, \eta_P). \tag{B.4}$$

Finally, we update location of the particle P^n by

$$x_{P^{n+1}} = x_{P^n} + u_P^{n+1} \Delta t, \tag{B.5}$$

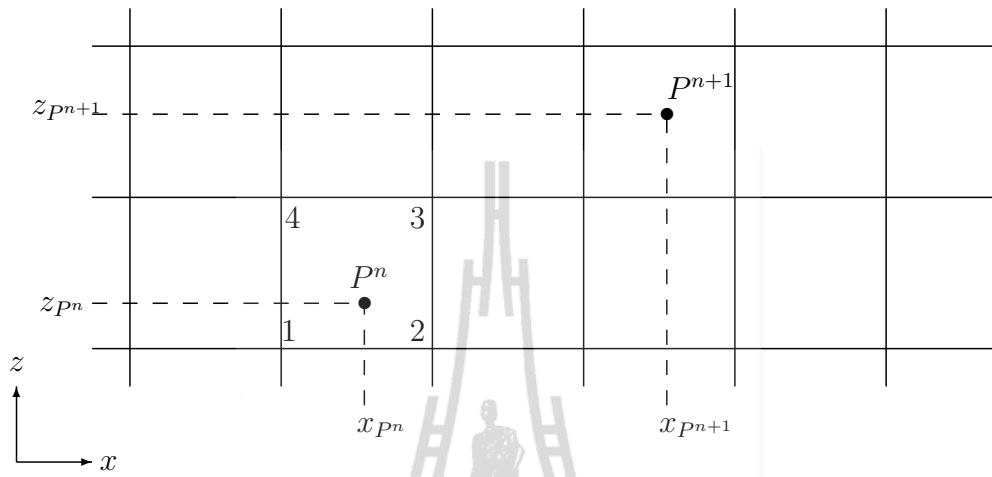$$z_{P^{n+1}} = z_{P^n} + v_P^{n+1} \Delta t. \tag{B.6}$$

Figure B.2 Particle P moves from P^n to P^{n+1}.
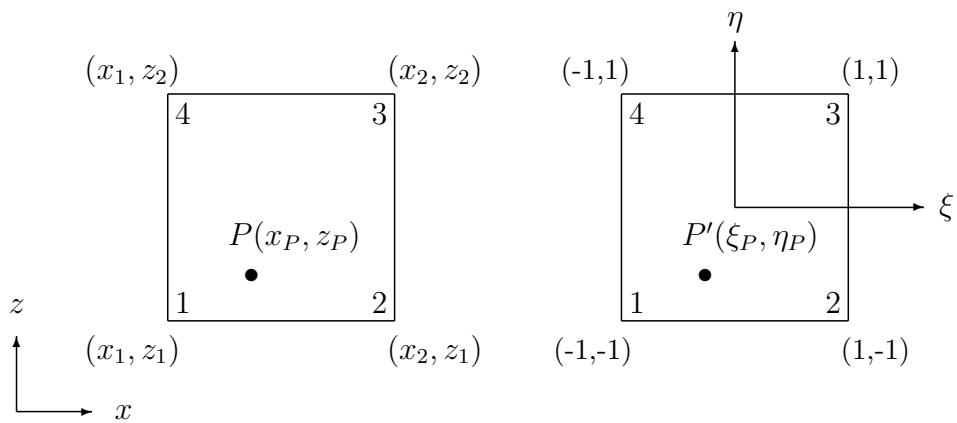
(a) Cell $C \subset \Omega$.   (b) Local cell of C.

Figure B.3 Transformation of $P(x_P, z_P)$ to $P'(\xi_P, \eta_P)$.

CURRICULUM VITAE

NAME: Kridsada Narong **GENDER:** Male

NATIONALITY: Thai **MARITAL STATUS:** Single

DATE OF BIRTH: June 16, 1975

EDUCATIONAL BACKGROUND:

- B.Sc. in Mathematics, Khon Kaen University, Khon Kaen, Thailand, 1996.

- M.Sc. in Computational Science, Chulalongkorn University, Bangkok, Thailand, 2003.

WORK EXPERIENCE:

- Lecturer in Mathematics at Department of Mathematics, Statistics and Computer, Faculty of Science, Ubon Ratchathani University, Thailand, 1997-2000 and 2004.

CONFERENCES:

- K. Narong and N.P. Moshkin, (2009), "On the performance of high-resolution advection schemes in the context of laminar mixed region collapse in density stratified fluid", **The 2nd SUT Graduate Conference 2009, Nakhon Ratchasima, Thailand.**

- K. Narong and N.P. Moshkin, (2009), "On the performance of high-resolution advection schemes in the context of laminar mixed region collapse in density stratified fluid", **The 13th Annual National Symposium on Computational Science and Engineering 2009, Kasetsart University, Bangkok, Thailand.**

SCHOLARSHIPS:

- The Ministry of University Affairs of Thailand (MUA), 2005-2008.